January 2016

UNDERSTANDING AND EVALUATING CRYSTAL POLYMORPHISM BY SECOND HARMONIC GENERATION MICROSCOPY

Azhad Chowdhury Chowdhury
Purdue University

Graduate School Form 30
(Updated 11/20/2014)

PURDUE UNIVERSITY
GRADUATE SCHOOL
Thesis/Dissertation Acceptance

This is to certify that the thesis/dissertation prepared

By Azhad U. Chowdhury

Entitled UNDERSTANDING AND EVALUATING CRYSTAL POLYMORPHISM BY SECOND HARMONIC GENERATION MICROSCOPY

For the degree of Doctor of Philosophy

Is approved by the final examining committee:

Garth J. Simpson

Mary J. Wirth

Chittaranjan Das

Lynne S. Taylor

To the best of my knowledge and as understood by the student in the Thesis/Dissertation Agreement, Publication Delay, and Certification/Disclaimer (Graduate School Form 32), this thesis/dissertation adheres to the provisions of Purdue University's "Policy on Integrity in Research" and the use of copyrighted material.

Garth J. Simpson

Approved by Major Professor(s): _____

_____

Approved by: Timothy Zwier 11/29/2016

Head of the Department Graduate Program Date

UNDERSTANDING AND EVALUATING CRYSTAL POLYMORPHISM BY SECOND HARMONIC GENERATION MICROSCOPY

A Dissertation

Submitted to the Faculty

of

Purdue University

by

Azhad U. Chowdhury

In partial Fulfillment of the

Requirements of the Degree

of

Doctor of Philosophy

December 2016

Purdue University

West Lafayette, Indiana

ACKNOWLEDGMENTS

Firstly, I would like to express my sincere gratitude to my advisor Prof. Garth Simpson for his continuous support in the last five years during my Ph.D study and related research work, and for his patience, motivation, and enormous knowledge. He appeared to be the most resourceful person in every aspect during my Ph.D career. His guidance helped me a lot in doing research, preparing manuscripts and writing this thesis. I do not think I would have been able to finish my Ph.D without his continuous support and encouragement. I would say joining the Simpson Lab was a great decision for me, here at Purdue university. I am always amazed with his enthusiasm, efficiency and multi-tasking skills. All I can say is during these five years he established himself as a role model to me. I wish him the best and to his lovely family.

Besides my advisor, I would like to thank the rest of my thesis committee: Prof. Mary Wirth, Prof. Chittaranjan Das, and Dr. Lynne Taylor for their time and eagerness in helping me. I am grateful that they were very approachable for anything I needed in the past.

I would like to thank my former and present lab mates for everything we have done together in the last five years. The Simpson Lab has always have been an exceptional learning environment, I must say. My special thanks to Shane, Chris, Emma, Ryan, Shijie, Nicole, Zhengtian, Sreya, and Janny for their support and contribution to my projects and

other tasks. All other lab members whose names I did not mention due to the limited space are awesome people in every aspect. It was my pleasure to meet and work with all of them.

I would like to thank the entire chemistry department for being so cooperative and nice to every graduate student. My special thanks to Michael, Hurtmut and Mark in the Amy facility for their contributions to my projects and for the time-to-time help as needed. I also would like to thank people in the Chemistry main office, General chemistry office, Business office, Procurement office, Chemistry shop, and copy center from whom I received much help. My graduate life wouldn't be this easy without all of your help.

I would like to thank my undergraduate advisor Dr. Lee for all of his support in my undergraduate life. He is the person who made me fall in love with chemistry and encouraged me to go for the graduate program. His inspiration and motivation still helps me to drive myself.

I am grateful to all my friends and family members who have always encouraged me, believed in me and prayed for me. Without their courage and enthusiasm, it would be very tough for me to come this far.

I am grateful to my parents for bringing me to this world and teaching me throughout my life to become a better person. My father was the greatest inspiration for me in every step of my life. He always wanted me to do something exceptional, taught me to think from different perspectives, and encouraged me to go for a Ph.D since my undergraduate life. Although he left this world I still feel like he is guiding me all the time. I am also grateful to my mother who has worked so hard throughout her entire life and has

taken all the burden just to make us happy without complaining. May Allah grant success to my parents both in this world and in hereafter.

Finally, I am so grateful to my beloved wife and son for everything. I attribute my success to them. My wife who has been with me in all the ups and downs in my life for the last seven years. She sacrificed the most to let me go through all the hardship without realizing it. She took all the burden of our family just to make my life easy so that I can focus on my Ph.D. My son is the meaning of life to me. I relieve all the stresses just thinking of his naughty smiley face. I pray to Almighty Allah that he gave me such a lovely family who are always there to make me happy.

TABLE OF CONTENTS

Page

LIST OF TABLES viii

LIST OF FIGURES ix

LIST OF ABBREVIATIONS xi

ABSTRACT xiv

CHAPTER 1. INTRODUCTION 1

1.1 Background and Motivation 1
1.2 Ostwald's Rule of Stages 2
1.3 Second Harmonic Generation (SHG) Microscopy for Polymorphs Characterization 3
1.4 Thesis Overview 4
1.5 References 7

CHAPTER 2. KINETIC TRAPPING OF METASTABLE AMINO ACID POLYMORPHS 10

2.1 Introduction 10
2.2 Experimental 14
2.2.1 Sample Preparation 14
2.2.2 Inkjet Printing 14
2.2.3 Instrumental 15
2.2.4 X-ray Diffraction 16
2.2.5 Algorithm 16
2.3 Results and Discussion 17
2.4 Conclusion 27
2.5 References 29

Page

CHAPTER 3. EXCITON COUPLING MODEL FOR THE EMERGENCE OF SECOND HARMONIC GENERATION FROM ASSEMBLIES OF CENTROSYMMETRIC MOLECULES 47

3.1 Introduction 47
3.2 Theoretical Foundation 50
3.3 Experimental 52
3.3.1 Computational Methods 52
3.3.2 Instrumental 53
3.4 Results and Discussion 53
3.4.1 Case Study 1: Butadiene Dimer 53
3.4.2 Case Study 2: 2,6-di-tertbutyl-anthraquinone (TAQ) Crystals 61
3.5 Conclusion 65
3.6 References 66

CHAPTER 4. SENSITIVE DETECTION OF POLYMORPH TRANSITIONING IN CLOPIDOGREL BISULPHATE BY SECOND HARMONIC GENERATION MICROSCOPY WITH RAMAN SPECTROSCOPY 75

4.1 Introduction 75
4.2 Experimental 79
4.2.1 Material and Sample Prep 79
4.2.2 SHG Imaging 79
4.2.3 SHG Guided Raman Measurement 80
4.2.4 X-ray Diffraction Measurement 81
4.2.5 Image Segmentation and Registration 81
4.3 Results 82
4.3.1 Pure sample Measurement 82
4.3.2 Form I and Form II Mixture 83
4.3.3 Raman Spectroscopy for Crystal Form Discrimination 84
4.3.4 X-ray Diffraction for Further Validation 84
4.4 Discussion 86
4.5 Conclusion 88
4.6 References 90

CHAPTER 5. POWDER ANALYSIS BY SECOND HARMONIC GENERATION MICROSCOPY 99

5.1 Introduction 99
5.2 Theoretical Foundation 101
5.2.1 Estimating the Effective Interaction Length Under Different Limiting Conditions 103
5.2.2 Modeling Interactions in the Focal Volume 105

Page

5.3 Experimental 108
5.3.1 Sample Preparation 108
5.3.2 Simulations 109
5.3.3 Imaging 109
5.4 Results and Discussion 110
5.4.1 Modeling the Impact of Numerical Aperture 110
5.4.2 Isolated Point Source Measurements 112
5.4.3 Crystal Orientation, Size, and Phase-Matching 114
5.4.4 Packing Density 117
5.4.5 Prediction of the Model 118
5.5 Summary 122
5.6 Conclusion 124
3.6 References 125

VITA 138

PUBLICATIONS 139

LIST OF TABLES

Table Page

Table 2.1 Statistical details of bright field and SHG images of inkjet printed dot matrices of proline solution. 45

Table 2.2 Percentage of area under the peak at the corresponding diffraction angle of each PXRD.....46

Table 3.1 CIS calculations on 1,3-butadiene monomer and dimer at two distances. 74

LIST OF FIGURES

Figure Page

Figure 2.1 The change in Gibbs free energy change (ΔG) as a function of the radius of the cluster. 33

Figure 2.2 Laser transmittance and SHG images of racemic proline, obtained from two different conditions. 34

Figure 2.3 Bright-field and SHG images of dot matrix printed racemic solution. 35

Figure 2.4 Bright-field and SHG image of inkjet printed D- and L-proline. 36

Figure 2.5 Laser transmittance and SHG images of re-hydration of inject printed metastable polymorph of proline produced from racemic solution. 37

Figure 2.6 Images of the first two principle components of inkjet printed proline. 38

Figure 2.7 Histogram of pixels containing PC2 of all SHG active D-, L-, and racemic proline crystals. 39

Figure 2.8 Confocal Raman spectrum of L proline powder and all other Inkjet printed proline solutions. 40

Figure 2.9 Diffraction image analysis of inkjet printed racemic solution. 41

Figure 2.10 Recovered diffraction peaks after autocorrelation along the azimuthal direction. 42

Figure 2.11 Comparison of the XRD peak positions. 43

Figure 2.12 Ternary phase diagram of D-proline, L-proline and H_2O at 25°C. 44

Figure 3.1 1,3-butadiene dimer used in quantum simulations. 69

Figure 3.2. Exciton coupling diagram for 1,3-butadiene. 70

Figure 3.3. Calculated hyperpolarizability of 1,3-butadiene dimer at varying dimer distances. 71

Figure Page

Figure 3.4. Calculated hyperpolarizability of the 1,3-butadiene dimer at different incident frequencies. 72

Figure 3.5. Laser transmitted images of TAQ from different crystallization conditions. .73

Figure 4.1 Raman spectroscopy integrated SHG microscope and its schematic diagram.. 93

Figure 4.2 Pure sample measurement of Form I and Form II.....94

Figure 4.3 Integrated SHG along the Z-axis of Form I and Form II. 95

Figure 4.4 Representation of segmentation algorithm to recover the Form II particles. ..96

Figure 4.5 Crystal form classification confirmed by independent SHG-guided Raman analysis on a per-particle basis. 97

Figure 4.6 Initial classification by SHG/V measurement of 10% physical mixture of Form II in Form I, and validation by XRD measurement. 98

Figure 5.1 Pictorial depiction of the effective volumes associated with the different limiting interaction lengths. 129

Figure 5.2 Theoretical SHG activity of a powder under phase matched (PM) and non-phase matched (NPM) conditions calculated for different numerical apertures.....130

Figure 5.3 Recovery of the beam intensity profile as a function of axial position. 131

Figure 5.4 Determination of the scattering length l_s. 132

Figure 5.5 Illustration of the image processing. 133

Figure 5.6 Illustration of the approach used to select the lower and upper thresholds prior to particle counting.....134

Figure 5.7 Comparison of the raw versus corrected 135

Figure 5.8 Histogram of $\log_{10}$(particle area) fitted to a normal distribution.....136

Figure 5.9 The measured size-dependent SHG intensity recovered from the histogram.....137

LIST OF ABBREVIATIONS

ANDA	Abbreviated New Drug Applications
API	Active Pharmaceutical Ingredient
CCD	Charged Coupled Device
CIS	Configuration Interaction
CNT	Classical Nucleation Theory
CW	Continuous Wave
DFT	Density Functional Theory
EOM	Electro Optic Modulator
FDA	Food and Drug Administration
HF	Hartree Fock
HOMO	Highest Occupied Molecular Orbital
HT	High-throughput
KDP	Potassium Dihydrogen Phosphate
KP	Kurtz-Perry
LUMO	lowest Unoccupied Molecular Orbital

LOD	Limit of Detection
MW	Molecular Weight
NA	Numerical Aperture
NCC	Normalized Cross Correlation
NDA	New Drug Applications
NLO	Nonlinear Optics
NPM	Non-phase Matching
PC1	Principle Component 1
PC2	Principle Component 1
PCA	Principle Component Analysis
PEG	Polyethylene Glycol
PM	Phase Matching
PPM	Parts per Million
PSHG	Powder Second Harmonic Generation
PXRD	Powder X-ray Diffraction
RSD	Relative Standard Deviation
SEM	Scanning Electron Microscopy
SFG	Sum-Frequency Generation
SHG	Second Harmonic Generation
SONICC	Second Order Nonlinear Optical Imaging of Chiral Crystals

TAQ	2,6-di-tertbutyl-anthraquinone
TDHF	Time-Dependent Hartree Fock
XRD	X-ray Diffraction

ABSTRACT

Chowdhury, Azhad U. Ph.D., Purdue University, December 2016, Understanding and Evaluating Crystal Polymorphism by Second Harmonic Generation Microscopy. Major Professor: Garth J. Simpson.

The crystalline form of a solid can profoundly affect its physical and chemical properties, with both potentially stable and metastable crystal polymorphs are accessible during crystal formation. Conventional methods limit the detection of rare nucleation and rapid phase transitioning events due to their lack of selectivity and sensitivity. Inkjet printing of a solution confines the nucleation event in a few micrometer volumes within the droplet, and furthermore rapid desolvation favors the kinetic factor to trap the rare metastable polymorphs. Second harmonic generation microscopy (SHG) possesses enough sensitivity to detect sub-micrometer size chiral crystals selectively and has the potential for use in crystal nucleation studies.

The unfavored noncentrosymmetric crystal forms are observed by SHG microscopy in inkjet printed racemic solution of an amino acid. Polarization-dependent SHG measurement and synchrotron X-ray microdiffraction analysis of individual printed drops are consistent with formation of homochiral crystal production. Fundamentally, these results provide evidence supporting the ubiquity of Ostwald's Rule of Stages, describing the hypothesized transitioning of crystals between metastable polymorphic forms in the early stages of crystal formation.

In addition to the metastable polymorphs characterization, quantification of SHG signal is essential for definitive discrimination for the polymorphs with a certain confidence interval. In this regard, a microscopy approach is developed for quantifying (SHG) activity of powders that largely decouples linear and nonlinear optical interactions. Decoupling the linear and nonlinear optical effects provides a means to independently evaluate and optimize the role of each in crystal engineering efforts and facilitates direct comparisons between experimental and computational predictions of lattice hyperpolarizabilities. Using a focused fundamental beam places a controllable upper bound on the interaction length, given by the depth of field. An analytical model that includes scattering losses of a focused Gaussian beam reliably predicted several experimental observations. Specifically, the measured scattering length for SHG is in excellent agreement with the value predicted based on the particle size distribution. Additionally, histograms of the SHG intensities as functions of particle size and orientation agreed nicely with predictions from the model.

CHAPTER 1. INTRODUCTION

1.1 Background and motivation

Polymorphism and polymorphic transitions of an active pharmaceutical ingredient (API) are equally important in pharmaceutical formulation. Polymorphs are chemically identical but their crystal structures are different from each other. Therefore, the thermodynamic stability and other physicochemical properties of APIs can be significantly affected by polymorphism.[1,2] In most cases, thermodynamically less stable polymorphs, known as metastable polymorphs, have a tendency to transform into the most stable form, which is extremely problematic for pharmaceutical industries from the early stage of drug development to the shelf life of a final product.[1,3,4] A well-known example of this is Ritonavir, a semisolid capsule, in which the marketed polymorphic form (Form I) spontaneously converted to a more stable polymorph (Form II). The more stable Form II exhibited much slower dissolution kinetics and the product had to be withdrawn from the market with an estimated cost of $250 million.[5] In most cases, the most stable form is considered for formulation over other forms to avoid phase transformation, but in a few cases metastable forms were chosen due to their higher solubility and bioavailability.[3] A recent study estimates that 80-90% of APIs exhibit polymorphism.[1] In this context, the Food and Drug Administration (FDA) and other government agencies require an intensive

solid form screening of APIs at the time of filing new drug applications (NDAs) and abbreviated new drug applications (ANDAs).[6] However, the origin of the polymorphism or the polymorphism related phenomena are not fully understood yet.[3,7,8]

1.2 Ostwald's Rule of Stages

Formation of metastable polymorphs can be described by the Ostwald's rule of stages, which suggests that during the crystallization in solution, a high energetic system moves toward the equilibrium through a minimal change of its free energy in a series of steps.[9,10] Thus the least stable polymorph whose free energy is closest to the mother liquor nucleates first followed by an adiabatic transition through increasingly more stable forms before it reaches the most stable crystal form.[11,12] Although this purely thermodynamic argument supports many experimental observations, many other experimental results cannot be explained by this rule. Rather, Ostwald transitioning can be understood in terms of kinetics through classical nucleation theory. Crystallization can be described in two distinct steps, nucleation and crystal growth, in which the formation of the final crystalline form is the combination of thermodynamic and kinetic effect. According to classical nucleation theory (CNT), critical nucleus formation is an interplay between surface free energy (ΔG_S) and bulk free energy (ΔG_B).[9,11,13] In this context, the polymorph that nucleates first has the lowest free energy barrier (ΔG) and thus the faster nucleation rate. However, this metastable polymorph may not necessarily transform into the most thermodynamically stable polymorph. The final crystalline form results from one of two ways: i) the relatively unstable polymorph can spontaneously convert to the stable form, or ii) kinetic factor that

prevents the equilibrium of a solution containing multiple metastable crystalline forms. The most stable polymorph will always be problem, just at vanishingly slow rate in cases where they are trapped, and more commonly they are very short lived. Therefore, a general rule is that crystallization under thermodynamic conditions in infinite time produces the stable form, while a metastable form is expected to be produced under kinetic conditions (e.g., rapid cooling, rapid desolvation).[3] In either case evidence of these polymorphic transformations is difficult to observe as crystal nucleation is intrinsically a rare event and polymorphic changes upon nucleation are generally expected to be short lived.[9,11] At the same time, conventional crystallization detection methods (e.g. X-ray diffraction, Raman spectroscopy, infrared (IR) spectroscopy, etc.) do not possess enough sensitivity to selectively detect the stochastic nucleation event.

1.3 Second Harmonic Generation (SHG) Microscopy for Polymorph Characterization

Nonlinear optical (NLO) imaging methods for chiral crystal detection and quantification have the potential to enable rapid characterization of pharmaceutical crystalline solids.[14-16] In particular, second harmonic generation (SHG) has emerged as a contrast mechanism, as it is highly selective for noncentrosymmetric (i.e., chiral) crystals[17] and produces no coherent SHG signal from liquids (even from a noncentrosymmetric solution), gases, and amorphous solids. SHG is the frequency doubling of light arising from a second order nonlinear optical process.[18] Coherent SHG selectively arises from the bulk crystalline fraction with an appropriate symmetry within the focal volume. At the same time, the energy difference between the SHG signal and the fundamental beam is 100%. Therefore, signal can be measured with higher sensitivity with little or no background. In

this context, crystal formation and transition from one polymorph to another can be detected selectively with a higher sensitivity by the inherent chirality property of new pharmaceutical APIs. Under favorable conditions this selectivity for crystalline API has allowed measurements to reach detection limits on the order of parts per billion to as low as parts per trillion.[19] Several studies done in the past few years within the Simpson group indicate the potential use of SHG microscopy for pharmaceutical formulations analysis such as high-throughput (HT) screening, rapid polymorph discrimination,[20] and trace crystallinity detection in amorphous solid dispersions or in excipients matrix.[14-17,21] Therefore, SHG microscopy is potentially a suitable analytical tool for solid form screening.

1.4 Thesis Overview

Crystallization is the key experimental procedure to produce multiple crystalline forms. Crystal form determines the physicochemical properties of the solid materials, although the fundamental elements of phase transition remain elusive. In practice, measuring the overall nucleation rate and growth rates is comparatively simple, but insights into the earliest stages of growth following nucleation and the structures initially emerging are particularly challenging to obtain. Therefore, this interesting early nucleation event is important for the development of a fundamental understanding of crystallization processes and the development of reliable predictive models.

Polymorph transitioning may also explain the nearly universal observation of faster nucleation rates than those predicted by classical nucleation theory using bulk free-energy parameters.[22,23] Like all kinetic processes, a wide range of rate constants for inter-

conversion can be reasonably expected, from the extreme long-lived case in ritonavir, to structures that may only survive a few seconds or less. If short-lived metastable intermediates are found to routinely emerge following the early stages of crystal formation, it could lead to methods for recovering predictive rate constants by classical nucleation theory (or variations thereof) based on the surface and bulk free energies of the metastable polymorphs. Challenges remain, largely due to difficulties in the measurements.

This dissertation explores the strength of SHG microscopy to understand and to evaluate crystal polymorphism, particularly, for kinetically trapped metastable polymorphs of amino acid characterization, theoretical and experimental foundation to interpret the SHG signals from a medium that is symmetry forbidden for SHG, polymorphic phase content quantification in a two-polymorph mixture of an API, and finally, quantification of SHG signal in highly scattering environment. Chapter 2 focuses on the kinetic trapping of metastable polymorphs of amino acids. The experimental method of metastable polymorph trapping and characterization is discussed in details. The results of this study support the ubiquity of Ostwald's Rule of Stages, a hypothesized transitioning of crystals between metastable polymorphic forms in the early stages of crystal formation. Chapter 3 discusses a simple model to interpret the presence of substantial SHG activity from assemblies of centrosymmetric molecular building blocks. A quantum chemical calculation of a model system describes the origin of this signal through exciton coupling arguments based on the electronic structure of the monomer and the relative orientation between the monomers within the dimer. Experimental observations support the anticipated results through a metastable polymorphs formation of the analyte which is proposed as an alternative molecular packing configurations. So far it has been found that SHG microscopy is well-

suited for quantitative analysis, but the measurements carry little meaningful chemically-specific information for qualitative analysis of chemical composition. Chapter 4 discusses the use of Raman spectroscopy guided by SHG microscopy for the characterization and quantification of polymorphic phase content in an API mixture. Finally, chapter 5 discusses a microscopy approach for quantifying second harmonic generation (SHG) activity of powders that largely decouples linear and nonlinear optical interactions. Detecting signals in a powdered matrix is challenging for several reasons – signals are generated from a wide range of particle size distributions with random shapes and orientations, scattering losses of signals from the depth of penetration. It shows that the proposed microscopy based approach is capable of quantifying SHG signal on a per particle basis.

1.5 References

1 Chieng, N., Rades, T. & Aaltonen, J. An overview of recent studies on the analysis of pharmaceutical polymorphs. *Journal of pharmaceutical and biomedical analysis* **55**, 618-644 (2011).

2 Vippagunta, S. R., Brittain, H. G. & Grant, D. J. Crystalline solids. *Advanced drug delivery reviews* **48**, 3-26 (2001).

3 Aaltonen, J. *et al.* Solid form screening–a review. *European Journal of Pharmaceutics and Biopharmaceutics* **71**, 23-37 (2009).

4 Chen, J., Sarma, B., Evans, J. M. & Myerson, A. S. Pharmaceutical crystallization. *Crystal Growth & Design* **11**, 887-895 (2011).

5 Bauer, J. *et al.* Ritonavir: an extraordinary example of conformational polymorphism. *Pharmaceutical research* **18**, 859-866 (2001).

6 Ciociola, A. A., Cohen, L. B. & Kulkarni, P. How drugs are developed and approved by the FDA: current process and future directions. *The American journal of gastroenterology* **109**, 620 (2014).

7 Davey, R. J. Crystallization: How come you look so good? *Nature* **428**, 374-375 (2004).

8 Dunitz, J. D. Are crystal structures predictable? *Chemical Communications*, 545-548 (2003).

9 Chowdhury, A. U. *et al.* Kinetic trapping of metastable amino acid polymorphs. *Journal of the American Chemical Society* **136**, 2404--2412, doi:10.1021/ja410293p (2014).

10 Ostwald, W. Studien über die Bildung und Umwandlung fester Körper. *Z. phys. Chem* **22**, 289-330 (1897).

11 Hall, V. J. & Simpson, G. J. Direct observation of transient Ostwald crystallization ordering from racemic serine solutions. *Journal of the American Chemical Society* **132**, 13598--13599, doi:10.1021/ja106728c (2010).

12 Nvlt, J. The Ostwald Rule of Stages. *Crystal Research and Technology* **30**, 443--449, doi:10.1002/crat.2170300402 (1995).

13 Abu Bakar, M. R., Nagy, Z. K., Saleemi, A. N. & Rielly, C. D. The impact of direct nucleation control on crystal size distribution in pharmaceutical crystallization processes. *Crystal Growth and Design* **9**, 1378-1384 (2009).

14 Schmitt, P. D., Trasi, N. S., Taylor, L. S. & Simpson, G. J. Finding the Needle in the Haystack: Characterization of Trace Crystallinity in a Commercial Formulation of Paclitaxel Protein-Bound Particles by Raman Spectroscopy Enabled by Second Harmonic Generation Microscopy. *Molecular pharmaceutics* **12**, 2378-2383 (2015).

15 Toth, S., Madden, J., Taylor, L., Marsac, P. & Simpson, G. Selective imaging of active pharmaceutical ingredients in powdered blends with common excipients utilizing two-photon excited ultraviolet-fluorescence and ultraviolet-second order nonlinear optical imaging of chiral crystals. *Analytical chemistry* **84**, 5869-5875 (2012).

16 Toth, S. J. *et al.* Ab Initio Prediction of the Diversity of Second Harmonic Generation from Pharmaceutically Relevant Materials. *Crystal Growth & Design* **15**, 581-586 (2015).

17 Wanapun, D., Kestur, U. S., Kissick, D. J., Simpson, G. J. & Taylor, L. S. Selective detection and quantitation of organic molecule crystallization by second harmonic generation microscopy. *Analytical chemistry* **82**, 5425-5432 (2010).

18 Boyd, R. W. *Nonlinear optics*. (Academic press, 2003).

19 Newman, J. A. *et al.* Parts per million powder X-ray diffraction. *Analytical chemistry* **87**, 10950-10955 (2015).

20 Schmitt, P. D., DeWalt, E. L., Dow, X. Y. & Simpson, G. J. Rapid Discrimination of Polymorphic Crystal Forms by Nonlinear Optical Stokes Ellipsometric Microscopy. *Analytical chemistry* (2016).

21 DeWalt, E. L., Sullivan, S. Z., Schmitt, P. D., Muir, R. D. & Simpson, G. J. Polarization-modulated second harmonic generation ellipsometric microscopy at video rate. *Analytical chemistry* **86**, 8448-8456 (2014).

22 Vehkamaki, H. *Classical nucleation theory in multicomponent systems*. (Springer-Verlag, 2006).

23 Erdemir, D., Lee, A. Y. & Myerson, A. S. Nucleation of Crystals from Solution: Classical and Two-Step Models. *Acc. Chem. Res.* **42**, 621-629 (2009).

CHAPTER 2. KINETIC TRAPPING OF METASTABLE AMINO ACID POLYMORPHS

2.1 Introduction

In a few relatively rare cases, the time-frame for polymorph transitioning can be long enough to enable detection of the metastable intermediates using conventional existing methods.[1-3] Perhaps the most famous example involves the case of ritonavir (Norvir®).[4-6] Only when a more thermodynamically stable Form II polymorph of ritonavir first appeared in commercial Norvir gel-caps was it realized that the initial form was metastable. The more stable Form II exhibited much slower dissolution kinetics and the product had to be withdrawn from the market and reformulated.

The formation of metastable polymorphs can be interpreted thermodynamically according to the Ostwald-Lussac's Rule of Stages, which states that the form having the Gibbs free energy closest to the solvated molecules in the mother liquor, will crystallize first,[3,7,8] followed by adiabatic transitions through increasingly more stable forms before ultimately arriving at the most stable crystal form.[1] However, this purely thermodynamic argument is based on an adiabatic limit. In practice, direct observation of such polymorph transitions are challenging given the rare and transient nature of crystal nucleation. More than a century after the original hypothesis by Ostwald, methods are now becoming available to systematically observe polymorphic transitions experimentally according to the Ostwald Rule of Stages at the individual building-block scale in a few model systems.[9-

[11] Studies of colloidal crystal nucleation have provided a route for increasing the size of the "molecule" to one large enough to observe by conventional optical microscopy.[1,10] Experiments of protein crystallization[12] and simulations of relatively simple model systems[9,13-16] also support a multi-step process for crystallogenesis. The most compelling evidence for direct observation of rapid transitioning according to the Ostwald Rule of Stages in a system with directional bonding arguably comes from electron microscopy measurements of $LiFePO_4$ nanocrystals.[1] In this study Chung and coworkers observed at least four different polymorphic forms of the inorganic crystal sequentially at atomic resolution during high-temperature crystal formation. However, these atom/particle model systems generally consist of relatively simple highly symmetric building blocks with low barriers for interconversion between polymorphs and correspondingly facile polymorph transitioning. More complex molecules of low symmetry with greater conformational freedom generally can be expected to exhibit larger entropic barriers for interconversion. Consequently, studies working toward the broader goal of characterizing complex molecular species have been limited primarily by the difficulties in definitively isolating and characterizing the individual transient structures at low concentration and small sizes generated during the very earliest stages following crystal nucleogenesis.

According to classical nucleation theory, the rates of formation and growth of crystal nuclei arise from an interplay between surface free energy (ΔG_S) and bulk free energy (ΔG_B).[11,12,17,18] The critical cluster size for nucleation corresponds to the maximum in the total free energy surface, as shown in Figure 2.1. The polymorph with the lowest barrier for nucleation may not necessarily correspond to the most thermodynamically stable bulk form. The transition to the most stable form can arise from two mechanisms. First, the

relatively unstable polymorph can spontaneously convert to the alternative form, which requires another solid-state nucleation event. Second, the presence of crystallites of the stable polymorphic form elsewhere within the mother liquor can grow at the expense of the metastable forms through Ostwald ripening. In either case evidence of these polymorphic transformations is difficult to obtain as crystal nucleation is intrinsically a rare event and polymorphic changes upon nucleation are generally expected to be short-lived.

The conditions most likely to result in long-lived metastable polymorph generation correspond to small, confined volumes and rapid desolvation to reduce the possibility of ripening or interconversion. Inkjet printing, which deposits picoliter dots of solutions on substrates, is well-matched to these requirements. In addition, inkjet printing can serve as a model for other deposition techniques involving rapid solvent evaporation, including spray-drying, which is used routinely in the preparation of high surface-area APIs.[19]

In the current study, piezoelectric inkjet printing was employed to produce metastable polymorphs of proline and second harmonic generation (SHG) microscopy used as a probe for identifying noncentrosymmetric (metastable) crystal domain formation. Two algorithm approaches, principal component analysis (PCA) and autocorrelation, have been used on the polarization dependent SHG images and x-ray diffraction images of inkjet printed dots to verify the presence of kinetically trapped metastable polymorphs of proline upon rapid crystallization from racemic solutions. The majority of the amino acids, including both proline and serine, produce centrosymmetric racemic co-crystals when crystallized from racemic aqueous solutions.[20,21] Consequently, any non-centrosymmetric crystal forms prepared from such solutions would necessarily be metastable. However,

crystal polymorphism studies using conventional methods (e.g., diffraction, Raman, infrared spectroscopy, NMR, calorimetry, etc.) typically do not have the sensitivity to selectively identify small quantities of the rare, unfavored polymorphs in mixtures.[22]

Second harmonic generation can be used as a contrast mechanism, as it is highly selective for non-centrosymmetric submicron sized noncentrosymmetric (i.e. chiral) crystals,[22] and producing no coherent SHG signal from liquids (even from a non-centrosymmetric solution), gases, and amorphous solids.[20,22-25] Crystals grown from a racemic proline solution are expected to be centrosymmetric, racemic co-crystals[21] and should not produce any SHG signal. However, the presence of detectable SHG signal from inkjet-printed microcrystals can serve as a simple indicator of the presence or absence of metastable polymorphic forms. Polarization-resolved SHG microscopy can further enhance the information content of SHG measurements,[26,27] given the sensitivity of the polarization dependence of SHG to crystal form and orientation. SHG can also be used to rapidly identify regions of interest for X-ray diffraction analysis, which in turn can be used to characterize polymorphism.[27-29] Here, we demonstrate the use of autocorrelation analysis of scattering patterns to recover high signal to noise XRD "powder patterns" from picogram to femtogram of material produced by piezoelectric inkjet printing, and use this approach for structural analysis of the metastable forms.

2.2 Experimental

2.2.1 Sample Preparation

D- and L-proline, assay ≥ 99%, were purchased from Sigma-Aldrich and used without any further purification. 0.7 M homochiral solutions of each were made in deionized water and racemic solution was prepared by obtaining equal volume of each. In order to produce thermodynamically controlled racemic proline crystals, the racemic solution was kept on the hot plate with a gentle heat for 30 minutes to prepare a super-saturated solution then cooled down to room temperature and kept in a fume hood overnight for spontaneous crystallization. Fine white crystals were formed. Racemic mixture of dry proline crystals were prepared by crushing equal parts of the two homochiral proline powders in a mortar and pestle.

2.2.2 Inkjet Printing

Homochiral and racemic proline solutions were printed on hydrophobic glass cover slips and on MiTeGen UV-Vis 100 μm MicroTip by a Fujifilm Dimatix Material printer DMP 2800. Proline soluctions were printed in dot matrix arrays with 80 μm periodicity between spots and 120μm periodicity between rows, respectively (10x10 array). A standard monopolar waveform with an average jetting voltage of 33V and nozzle temperature of 48°C were used to print the arrays. Deposited volumes of <8 fL and <2 fL were estimated from the residual solid on the substrate in the array dots from homochiral and racemic solutions. The average printing time of each pattern was ~10-12 seconds.

2.2.3 Instrumental

A built-in-house beam scanning SHG-microscope was used to acquire images. Beam scanning was performed with a resonant vibrating mirror (~8 kHz, EOPC) along the fast-axis scan, and a galvanometer (Cambridge) for slow-axis scanning. The 80 MHz Ti:sapphire pulsed laser (Spectra-Physics Mai Tai) of 100 fs pulse width directed through the scan mirrors and focused onto the sample using a 10× objective of working distance 1.6 cm (Nikon, N.A.=0.30). Under typical operating conditions, the incident wavelength was 800 nm, with 80 mW laser power recorded before the objective. In order to reduce 1/f noise in the polarization-dependent measurements, a custom electro-optical modulator (EOM, Conoptics) was positioned in the beam path, enabling high frequency (16 MHz) modulation of the polarization state of the beam. The laser repetition rate was doubled by an orthogonal pulse pair generator, in which the primary beam was split and recombined following a 6.25 ns delay to produce an interleaved pulse train of orthogonal polarizations prior to the EOM.[30] Synchronous digitization of each laser pulse with strict timing control was used to identify the polarization-dependence of each incident laser shot.[31] Polarized transmission SHG signals were collected, with dichroic mirrors and narrow band-pass filters (Chroma HQ400/20 m-2p) centered around 400 nm placed prior to the photomultiplier tube detectors (Burke, XP 2920PC). Matlab code was written in-house to control the scanning mirrors and communication with the data acquisition electronics. Concurrently with the transmission SHG detection, bright field images were acquired by measuring the extinction of the 800 nm beam using a photodiode, also acquired in transmission. Bright field and SHG images were rendered and analyzed with Image J to produce a set of 10 unique polarization-dependent images per detector and "analyze

particles" options were used to measure the area of each dot in bright field as well as SHG active regions.[32]

2.2.4 X-ray Diffraction

X-ray microdiffraction measurements were acquired at GM/CA beamline 23- ID-B with a 10 μm-diameter, 12.0 keV X-ray beam with 1 s exposure time, at a photon flux of 1.3 x 10^{10} photons s^{-1} (5-fold attenuation) and detector distance of 150 mm, at the Advanced Photon Source within Argonne National Laboratory.[27-29] An SHG microscope built into the beamline and described previously was used to discriminate between the SHG-active and inactive dots in inkjet printed arrays, and position them within a collimated 10 μm-diameter X-ray beam. Diffraction patterns were collected from both SHG active and SHG inactive dot of racemic proline and from pure L-proline dot.

2.2.5 Algorithm

Analysis of the X-ray scattering images was performed by autocorrelation over the azimuthal rotation angle for peak-detection in order to suppress diffuse scatter and improve the S/N of the diffraction measurements. In brief, scattering images were transformed into polar coordinates by use of python image processing,[33] followed by autocorrelation along the φ axis was performed by the Wiener-Kmintchine method.[34,35] The differences between the asymptotic mean of the azimuthal autocorrelogram and the mean of the autocorrelogram over steps of 1-4 pixels were plotted as a function of the radial 2θ angle. This algorithm served to retain sharp features in the scattering pattern consistent with diffraction, while suppressing rolling features from diffuse scattering arising from

amorphous materials or through inelastic scattering events. For comparative purposes, conventional powder XRD scattering patterns were also produced simply by integration over all the azimuthal angles and all the regions probed by the X-ray beam.

For the polarization-dependent studies, principal component analysis (PCA) was performed on 10 different input and output SHG polarization combinations using R v.2.15 with the built-in PCA function (princomp).[27,36] Each pixel in the SHG images was treated as a "hyperspectral" vector in a ten dimensional polarization space.[26] PCA separates the data into the eigenvectors or principal components that maximize the total variance in the data set, the first few of which provide the greatest separation within the polarization dependent dimensions.

2.3 Results and Discussion

Laser transmittance and SHG images of racemic proline crystals produced by solvent evaporation from racemic solutions and physical mixtures (1:1 mass ratio) of two homochiral powder are presented in Figure 2.2. The crystals of homochiral proline from aqueous solution adopt a $P2_12_12_1$ space group as the thermodynamically favored form,[37] which is SHG active. A physical mixture of the two homochiral crystalline materials prepared by grinding produced an ensemble that was racemic overall, but still primarily comprised of homochiral crystalline domains. SHG imaging of these materials produced a strong signal. The disparity between the bright regions in the SHG image and the optical transmittance images suggest that scattering losses in the optically opaque regions attenuated the SHG response, either through scattering of the fundamental and the corresponding reduction of SHG, or through the scattering of the coherent SHG to angles

outside the acceptance cone of the collection objective. Alternatively, the darker regions could correspond to domains in which the racemic solid dispersion has undergone phase transformation to either an amorphous material or the racemic co-crystal.[38] The racemic proline co-crystal produced upon crystallization of proline from a racemic solution adopts a $P2_1/c$ space group[21] with a centrosymmetric lattice, which is forbidden by symmetry from producing SHG.[23,25] Combining the results from all of the considered cases, the SHG-activity was >50-fold in the physical mixture of homochiral crystals than in the powders produced upon crystallization from a racemic solution.

Inkjet-printing racemic proline solutions on hydrophobic glass slides produced markedly different results. Figure 2.3a and 2.3b are bright field and SHG images of inkjet printed racemic proline solution, respectively. Seven out of twelve printed dots produced SHG signal while rest five did not (red circles in Figure 2.3b) show any SHG activity. Similar SHG activity was observed from multiple dot arrays (not shown) with >60% of printed racemic dots exhibiting SHG-activity. The average SHG photon counts of 45±6 from racemic dots were comparable to the average SHG counts of 45±5 from $BaTiO_3$ nano-crystals (200 nm) in polyethylene glycol (PEG) from the same laser power. SHG signals (Figure 2.3b) coincide qualitatively with locations of laser extinction (Figure 2.3a), although extinction arose over quantitatively larger areas. From the SHG intensity measurements (presented in Table 1), 82±2% of the area within the homochiral dot was SHG active, compared to just 58±2% in the racemic dot exhibiting SHG activity.

Several possible origins of the observed SHG-activity upon inkjet printing were considered. SHG is well-known to arise at interfaces between centrosymmetric media from local symmetry breaking.[23,25] In heterogeneous dots, multiple interfaces between

amorphous and/or crystalline domains may be present, contributing to interfacial SHG. The anticipated magnitude of the interfacial response can be estimated based on the relative number of bulk versus interfacial molecules producing signal. Assuming a ~1 μm^2 beam waist and a similarly sized crystal, the number of interfacial molecules is roughly 10^4-fold lower than the number of bulk molecules within a crystalline lattice (assuming a ~10 Å lattice constant). Given the quadratic scaling of SHG with number density, this difference corresponds to a ~10^8-fold difference in anticipated SHG from the interface of a centrosymmetric or amorphous media versus a noncentrosymmetric crystalline lattice. The observation of SHG-activity comparable in brightness to the highly SHG-active $BaTiO_3$ nanoparticles suggests the formation of bulk-allowed noncentrosymmetric crystal domains within the dot, and not SHG arising from interfaces. In addition, SHG from impurities in the racemic solutions is unlikely to serve as a major source of background, as those same solutions were used to prepare the SHG-inactive samples by slow-drying. Therefore, the SHG-activity from inkjet printing of the racemic solutions was attributed to noncentrosymmetric crystal formation.

Inkjet printed homochiral proline samples were also studied, prepared from same stock solutions used to produce the racemic solutions, producing representative SHG micrographs shown in Figure 2.4. The top row are Laser transmittance images and bottom row are SHG images of inkjet printed homochiral (D- and L-) proline. The average areas of the homochiral dots were larger than the racemic dots, possibly attributed to a lower surface tension, higher contact angle, and more spherical initial droplet of a homochiral proline solution comparing to that of the racemic solution. Secondary dot formation adjacent to the main drop, known as satellites, was observed from non-uniform ejection of

the ink dot from the cartridge from non-ideal matching of the ink to the jetting waveform, incorrect voltages, or high surface tension. No surfactant was used in these studies, which introduced additional challenges in control proper drop formation. The observation of clearly detectable SHG activity from each dot (Figure 2.4c, 2.4d) is consistent with the formation of known thermodynamically favored and SHG-active $P2_12_12_1$ space group[37,39] adopted by homochiral proline upon crystallization from aqueous solution.

The disparities between the total printed areas of the dot and the fraction of them that exhibited SHG activity suggests that a significant amorphous content remained following printing. For the dot prepared from homochiral solutions, all published polymorphs of proline identified by the authors fall into space groups that are allowed for SHG.[37,40] Therefore, it is reasonable to assign the SHG-inactive area to regions containing either amorphous proline or nanocrystalline proline with crystal sizes falling below the detection limits of SHG (i.e., SHG-amorphous). In the racemic dot, the SHG-inactive domains could correspond to either amorphous proline or to locations of SHG-inactive racemic co-crystals. If it is assumed that 20% of the area corresponds to amorphous material as in the homochiral dot, then the inactive co-crystal may potentially occupy the remaining 30%. However, this SHG-inactive fraction represents the minor constituent within the dot, rather than the major. Both the cross-sectional area of the dot exhibiting SHG-activity and the integrated brightness of the racemic dot (the SHG active racemic crystals were 2-3 times brighter than crystals in either homochiral dot) suggest that the majority of the printed volume corresponds to an SHG-active metastable polymorphic form.

In order to confirm that the SHG-active domains were indeed from metastable crystal forms, SHG-active inkjet printed dots prepared from racemic solutions were re-hydrated by extended exposure to 100% relative humidity and re-analyzed (Figure 2.5). The rehydrated dots exhibited SHG activities that were reduced 5-fold (18%) compared to the initially prepared dots after 24 hours in 100% relative humidity, which is consistent with interconversion to more stable crystal forms.

While the simple SHG intensity measurements summarized in Figure 2.3 and Figure 2.4 indicate the presence of SHG-active crystals produced from the racemic solution, the SHG intensity alone provides little meaningful information on the forms of the crystals produced. The observation of SHG-activity could potentially be arising from either homochiral crystallization, from the generation of noncentrosymmetric racemic co-crystals with both enantiomers present within the lattice, or some combination of the two.

Polarization-dependent SHG measurements were acquired and interpreted using principal component analysis (PCA) to aid in assessing the crystal forms produced upon inkjet printing the racemic solutions. A set of 10 polarization-dependent micrographs were used to define a 10-dimensional "polarization space", with PCA used to reduce the majority of the relevant polarization-dependent information to a few key principal components containing the majority of the intrinsic information content in the polarization-dependent data set. PCA results from the 10 different polarization combination images of inkjet-printed racemic proline solution and a histogram of all the dot are presented in Figure 2.6. Together, PC1 and PC2 contain 96% of the total signal variance. The first principal component, PC1, was dominated by differences in overall intensity as a function of location.[27,41,42] Therefore, PC2, carried the majority of the polarization-dependence of the

measurements. This interpretation is also consistent with previous work designed to detect different crystal domains by SHG imaging demonstrated that PC2 carries the majority of the polarization-dependent information.[27] Figure 2.7 is the histogram of PC2 values averaged within each dot.

Interestingly, the histogram of PC2 values (Figure 2.7) indicates reasonable separation between D- and L-proline by polarization-dependent SHG microscopy. This result is somewhat surprising, given that SHG is not predicted to enable discrimination between the two enantiomers from an isotropic population of crystal orientations (analogous to hyper-Rayleigh scattering). The ability to resolve the two therefore suggests preferred crystal orientation (e.g., from heterogeneous templating by the solid interface). It is even more remarkable that the influence of absolute chirality appears to provide a greater inherent variance in the SHG measurements than changes related to the random population of azimuthal orientations of the crystals. Both effects can be seen by inspection of the PC2 images in Figure 2.5, in which the PC2 values varied significantly within the individual dot (attributed to a population of oriented crystals), but integration over the dots nevertheless produced overall darker spots for the D-proline and vice versa for the L-proline.

Dot arrays prepared from printing the racemic solution produced PC2 values intermediate between the two homochiral crystal results. These observations are consistent with the formation of a population of homochiral crystals within the dot generated from printing the racemic solution. However, several alternative possibilities were also considered. First, the SHG-activity could be emerging from a noncentrosymmetric polymorph that still includes both enantiomers within the unit cell. No such forms are

known for proline, but could still be formed under kinetic control. It would be coincidental for the polarization-dependence of such a form to lie between the two homochiral poles in the histogram within Figure 2.7, but the possibility cannot be definitively excluded based solely on the SHG measurements.

In order to characterize those SHG active and inactive inkjet printed dots, confocal Raman measurements within individual inkjet printed dots were acquired by signal integration for 1.5 hours in a single inkjet confocal volume positioned within the printed dots, and compared with Raman spectra of the pure powders generated with 10 s integration times (Figure 2.8). For dots printed from the homochiral solutions, spectral features qualitatively similar to those observed from the racemic powder were observed. However, interpretation of the spectra was complicated by preferred orientation effects, as the relative intensities of the different Raman features are markedly different for the inkjet printed proline versus the powder spectra. Attempts were made to obtain confocal Raman spectra of the SHG-active dots produced from racemic solutions, but no sharp spectral features consistent with crystalline proline were observable, prohibiting meaningful assessment of crystal polymorphism by Raman. The absence of detectable Raman is attributed to the relatively weak Raman cross-section of proline, the trace quantities of crystalline material present, and the relatively high detection limits of Raman microscopy compared to both SHG and the minibeam synchrotron XRD method developed in this work.

X-ray microdiffraction measurements using synchrotron radiation were also performed to characterize the structures produced upon inkjet printing of proline solutions (Figure 2.9 and 2.10). Figure 2.9a and 2.9b are bright field and the SHG images of L-proline printed onto an X-ray micro tip, respectively. By using a microfocused beam only

10 μm in diameter to reduce background scatter, diffraction analysis could be performed on each individual printed dot. A representative scattering pattern is shown in Figure 2.9c. The small probed volume and even smaller crystal sizes associated with the diffraction measurements placed them between the two extreme limits of single crystal diffraction and powder X-ray diffraction (PXRD), in which a statistical population of crystal sizes and orientations are probed. The conditions of the current experiments preclude the ability to obtain large single crystals from inkjet-printed drops, however, they also do not produce enough microcrystals to approximate all possible crystal orientations. Consequently, an autocorrelation-based approach was developed to recover a powder-like pattern from the spots present in the scattering image, illustrated in Figure 2.10. First, the scattering image was transformed from Cartesian coordinates to radial coordinates, after first performing calibration to place the center of the undiffracted beam within one pixel of the center of the 4096×4096 element X-ray detection array. Following this transformation, the diffuse rings circling the beam stop in the initial image appear as vertical swaths in radial coordinates. Next, autocorrelation was performed along the azimuthal axis (vertical axis in Figure 2.9d). From the autocorrelogram at each radial 2θ distance, integration was performed over the short-lived features (1-4 pixels) corresponding to spots in the original scattering image, followed by subtraction of the asymptotic baseline arising from the diffuse scattering background. Autocorrelation provides no discrimination based on absolute azimuthal position, recovering a one-dimensional diffraction pattern analogous to what one might obtain by powder XRD (Figure 2.10). The S/N of >3000 from the synchrotron XRD measurements for a 1 s XRD integration time per pixel and 250 μs per-pixel integration time for SHG, compared to a S/N of the most prominent Raman peak was 16 after 1.5 hours

of signal averaging. Similar analyses were performed on several printed dot of the racemic solution (both SHG-active and SHG-inactive) as well as printed dot of homochiral L-proline.

Even with the autocorrelation analysis, the small volumes within each printed dot did not allow for statistical sampling of crystal orientations, complicating quantitative determination of crystal form directly from the relative intensities of the diffracted peaks. Therefore, the positions of peaks with S/N > 100 were used as the primary factor for structural assignment. A comparison of these peak positions are presented in Figure 2.11. The integrated intensities under these similar diffraction peaks were calculated along with total area under each PXRD in between 10□-28□ diffraction angle. Results indicate that 64% of the integrated peak intensity from SHG active racemic dot corresponded to 2θ locations also present for L-proline, while only 5% of area under the peak are present for SHG silent racemic proline (shown in Table 2.2). These results further support the polarization-dependent SHG analyses suggesting that the homochiral metastable crystal polymorph forms upon rapid inkjet printing from an aqueous solution.

Interestingly, about one third of the diffracted intensity within the SHG-active racemic dot did not overlap with diffraction peaks observed in either the homochiral dot or the racemic SHG-inactive dot. This disparity could arise from undersampling of the homochiral dot, such that not all 2θ diffraction locations were adequately sampled within the limited number of dot analyzed. Alternatively, additional crystal forms may be present that do not correspond to constituents of either of the other two sets of dot (i.e., homochiral and racemic SHG-inactive). Nevertheless, it appears that the homochiral metastable crystals comprise the majority composition of the racemic SHG-active dot based on X-ray

microdiffraction analysis. Consequently, the SHG-active domains are attributed to homochiral crystalline domains, with an equal probability of forming from the D- or L-enantiomers on a single nanocrystal basis.

The phase diagrams of proline provides a framework for describing the thermodynamic driving factors underpinning crystallization (Figure 2.12). Klussmann, Blackmond, and coworkers have presented a framework for predicting the anticipated eutectic points from combined solubility measurements of the enantiopure homochiral form and the racemic co-crystal.[43-45] Using this model, the solid lines for the phase boundaries were calculated using just the solubilities of the racemic and homochiral solutions. In the case of proline crystallizing from an aqueous solution, the solubilities of the two crystal forms are similar, with the solubility ratio of $\alpha = [\text{racemic}]_{sat}/[\text{enantiopure}]_{sat} = 0.78$ resulting in an anticipated eutectic point corresponding to a 0.89 mole fraction of pure enantiomer (or equivalently, and enantiomeric excess of 0.74). These results are in good qualitative agreement with previous studies of the crystallization of proline from hydrophobic solvents ($CHCl_3$ and $CHCl_3$/MeOH mixtures), in which the racemic form was found to exhibit substantially lower solubility than the enantiopure form and indicating a strong preference for formation of the racemic co-crystal.[43,45] However, the measured phase diagram in Figure 2.8 is in better qualitative agreement with the previous crystallizations in DMSO yielding a solubility ratio closer to 1. Quantitatively the solubility ratio in DMSO was reported to be $\alpha = 1.155$,[45] while the measurements presented here indicate $\alpha = 0.78$ in H_2O. Overall, the slightly lower solubility of the racemic form suggests that both crystal forms are energetically accessible under the conditions of the experiment, but the racemic co-crystal is clearly the

thermodynamically favored crystal produced from a racemic solution. Therefore, the observation of SHG-active forms emerging from a racemic solution indicates that crystallization is proceeding under kinetic control.

The presence of transient SHG-active polymorphic forms can be understood qualitatively from classical nucleation theory. Homogeneous crystal nucleation is driven by the interplay between an interfacial free energy cost and a volume free energy gain under conditions of supersaturation (Figure 2.1). Polymorphic forms with different interfacial free energy costs and volume gains have the potential to exhibit lower barriers for initial nucleation.[8,17] Under adiabatic conditions, curve crossing between different polymorphic forms can arise to ultimately favor growth of the most thermodynamically stable crystal form. However, curve-crossing may be avoided under non-adiabatic conditions of rapid solvent evaporation, promoting continued growth of kinetically trapped metastable polymorphs. If the SHG-active polymorphs are comprised of homochiral crystalline domains, transitioning to the more stable racemic co-crystal would require significant changes in the fundamental composition of the lattice, which may explain the presence of a relatively large kinetic barrier to interconversion.

2.4 Conclusion

The rapid drying of inkjet printed dot of racemic proline solutions on substrates produce SHG-active domains. These domains were attributed to the presence of metastable polymorphic forms kinetically trapped during rapid solvent desolvation, which supports Ostwald's conjecture of polymorph transitioning during crystallogenesis. Given the ubiquity of inkjet printing and the related approach of spray-drying as a preparative method

for pharmaceutical ingredients combined with the impact of crystal polymorphism on bioavailability, these findings may help guide future API formulations strategies that involve inkjet printing and spray drying.

For example, the possibility of a kinetic route to enable homochiral resolution has potential implications in pharmaceutical syntheses and the preparation of final dosage forms. While crystallization is arguably the most energy-efficient means of resolving homochiral compounds from an enantiomeric mixture, the process is only currently viable in the absence of resolving agents (e.g., chiral salts) under conditions in which the homochiral polymorph is the thermodynamically most stable form. Unfortunately, homochiral crystallization is often found to be the exception rather than the rule, with most compounds favoring racemic co-crystal production as in proline. However, if the emerging crystal form can be placed under kinetic control rather than thermodynamic control, a host of new possible options and architectures emerge for efficient chiral resolution through crystallization. SHG imaging may help enable such developments by rapidly identifying and optimizing potentially promising conditions.

2.5 References

1 Chung, S.-Y., Kim, Y.-M., Kim, J.-G. & Kim, Y.-J. Multiphase transformation and Ostwald's rule of stages during crystallization of a metal phosphate. *Nature Physics* **5**, 68--73, doi:10.1038/nphys1148 (2008).

2 Hamilton, B. D., Hillmyer, M. A. & Ward, M. D. Glycine Polymorphism in Nanoscale Crystallization Chambers. *Crystal Growth \& Design* **8**, 3368--3375, doi:10.1021/cg800326a (2008).

3 Nvlt, J. The Ostwald Rule of Stages. *Crystal Research and Technology* **30**, 443--449, doi:10.1002/crat.2170300402 (1995).

4 Bauer, J. *et al.* Ritonavir: an extraordinary example of conformational polymorphism. *Pharmaceutical research* **18**, 859--866 (2001).

5 Chemburkar, S. R. *et al.* Dealing with the Impact of Ritonavir Polymorphs on the Late Stages of Bulk Drug Process Development. *Organic Process Research \& Development* **4**, 413--417, doi:10.1021/op000023y (2000).

6 Morissette, S. L., Soukasene, S., Levinson, D., Cima, M. J. & Almarsson, O. Elucidation of crystal form diversity of the HIV protease inhibitor ritonavir by high-throughput crystallization. *Proceedings of the National Academy of Sciences of the United States of America* **100**, 2180--2184, doi:10.1073/pnas.0437744100 (2003).

7 Terry, T. Structural and thermodynamic explanations of Ostwald's rule. *Organic Process Research \& Development* **7**, 1017--1027 (2003).

8 Wilhelm, O. Studies upon the forming and changing solid bodies. *Zeitschrift fur Physikalsche Chemie* **22**, 289--330 (1897).

9 Chakraborty, D. & Patey, G. N. How Crystals Nucleate and Grow in Aqueous NaCl Solution. *The Journal of Physical Chemistry Letters* **4**, 573--578, doi:10.1021/jz302065w (2013).

10 Gasser, U., Weeks, E. R., Schofield, A., Pusey, P. N. & Weitz, D. A. Real-space imaging of nucleation and growth in colloidal crystallization. *Science (New York, N.Y.)* **292**, 258--262, doi:10.1126/science.1058457 (2001).

11 Zhang, T. H. & Liu, X. Y. Nucleation: what happens at the initial stage? *Angewandte Chemie (International ed. in English)* **48**, 1308--1312, doi:10.1002/anie.200804743 (2009).

12 Vekilov, P. G. Two-step mechanism for the nucleation of crystals from solution. *Journal of Crystal Growth* **275**, 65--76, doi:10.1016/j.jcrysgro.2004.10.068 (2005).

13 Anwar, J. & Boateng, P. K. Computer Simulation of Crystallization from Solution. *Journal of the American Chemical Society* **120**, 9600--9604, doi:10.1021/ja972750n (1998).

14 Anwar, J. & Zahn, D. Uncovering molecular processes in crystal nucleation and growth by using molecular simulation. *Angewandte Chemie (International ed. in English)* **50**, 1996--2013, doi:10.1002/anie.201000463 (2011).

15 Lutsko, J. & Nicolis, G. Theoretical Evidence for a Dense Fluid Precursor to Crystallization. *Physical Review Letters* **96**, 046102, doi:10.1103/PhysRevLett.96.046102 (2006).

16 Mucha, M. & Jungwirth, P. Salt Crystallization from an Evaporating Aqueous Solution by Molecular Dynamics Simulations. *The Journal of Physical Chemistry B* **107**, 8271--8274, doi:10.1021/jp034461t (2003).

17 Erdemir, D., Lee, A. Y. & Myerson, A. S. Nucleation of crystals from solution: classical and two-step models. *Accounts of chemical research* **42**, 621--629, doi:10.1021/ar800217x (2009).

18 Vekilov, P. G. Nucleation. *Crystal growth \& design* **10**, 5007--5019, doi:10.1021/cg1011633 (2010).

19 Basaran, O. a., Gao, H. & Bhat, P. P. Nonstandard Inkjets. *Annual Review of Fluid Mechanics* **45**, 85--113, doi:10.1146/annurev-fluid-120710-101148 (2013).

20 Hall, V. J. & Simpson, G. J. Direct observation of transient Ostwald crystallization ordering from racemic serine solutions. *Journal of the American Chemical Society* **132**, 13598--13599, doi:10.1021/ja106728c (2010).

21 Myung, S., Pink, M., Baik, M. H. & Clemmer, D. E. DL-Proline. *Acta crystallographica. Section C, Crystal structure communications* **61**, o506--508, doi:10.1107/S0108270105021001 (2005).

22 Wanapun, D., Kestur, U. S., Kissick, D. J., Simpson, G. J. & Taylor, L. S. Selective detection and quantitation of organic molecule crystallization by second harmonic generation microscopy. *Analytical chemistry* **82**, 5425--5432, doi:10.1021/ac100564f (2010).

23 Boyd, R. W. *Nonlinear Optics*. 3rd edn, (Academic Press, 2008).

24 Knight, P. L. The Principles of Nonlinear Optics. *Optica Acta: International Journal of Optics* **32**, 1--2, doi:10.1080/713821646 (1985).

25 Stegeman, G. I. & Stegeman, R. A. *Nonlinear Optics: Phenomena, Materials and Devices*. (John Wiley \& Sons, 2012).

26 Begue, N. J. & Simpson, G. J. Chemically selective analysis of molecular monolayers by nonlinear optical stokes ellipsometry. *Analytical chemistry* **82**, 559--566, doi:10.1021/ac901832u (2010).

27 DeWalt, E. L. *et al.* Polarization-resolved second-harmonic generation microscopy as a method to visualize protein-crystal domains. *Acta crystallographica. Section D, Biological crystallography* **69**, 74--81, doi:10.1107/S0907444912042503 (2013).

28 Kissick, D. J. *et al.* Towards protein-crystal centering using second-harmonic generation (SHG) microscopy. *Acta crystallographica. Section D, Biological crystallography* **69**, 843--851, doi:10.1107/S0907444913002746 (2013).

29 Madden, J. T. *et al.* Integrated nonlinear optical imaging microscope for on-axis crystal detection and centering at a synchrotron beamline. *Journal of synchrotron radiation* **20**, 531--540, doi:10.1107/S0909049513007942 (2013).

30 Jr, S. G. E. Polarization multiplexing with solitons. *Journal of Lightwave Technology* **10**, 28--35 (1992).

31 Muir, R. D., Sullivan, S. Z., Oglesbee, R. A. & Simpson, G. J. Synchronous digitization for high dynamic range lock-in amplification in beam-scanning microscopy. *Review of Scientific Instruments* **85**, 033703 (2014).

32 Abràmoff, M. D., Magalhães, P. J. & Ram, S. J. Image processing with ImageJ. *Biophotonics international* **11**, 36-42 (2004).

33 Klington, J.

34 Khintchine, A. Korrelationstheorie der station \ a ren stochastischen Prozesse. *Mathematische Annalen* **109**, 604--615 (1934).

35 Wiener, N. Generalized harmonic analysis. *Acta Mathematica* **Volume 55**, 117--258 (1930).

36 Jolliffe, I. T. Principal Components in Regression Analysis. 167--198, doi:10.1007/0-387-22440-8_8 (2002).

37 Wright, B. A. & Cole, P. A. Preliminary examination of the crystal structure of l - proline. *Acta Crystallographica* **2**, 129--130, doi:10.1107/S0365110X4900031X (1949).

38 Jacques, J., Collet, A. & Wilen, S. H. *Enantiomers, racemates, and resolutions*. (Wiley, 1981).

39 Wampler, R. D. *et al.* Selective detection of protein crystals by second harmonic microscopy. *Journal of the American Chemical Society* **130**, 14076--14077, doi:10.1021/ja805983b (2008).

40 Seijas, L. E., Delgado, G. E., Mora, A. J., Fitch, A. N. & Brunelli, M. On the crystal structures and hydrogen bond patterns in proline pseudopolymorphs. *Powder Diffraction* **25**, 235--240, doi:10.1154/1.3478557 (2012).

41 Lee, J. L. S., Gilmore, I. S. & Seah, M. P. Quantification and methodology issues in multivariate analysis of ToF-SIMS data for mixed organic systems. *Surface and Interface Analysis* **40**, 1--14, doi:10.1002/sia.2713 (2008).

42 Loukas, C. G., Wilson, G. D., Vojnovic, B. & Linney, A. An image analysis-based approach for automated counting of cancer cell nuclei in tissue sections. *Cytometry. Part A : the journal of the International Society for Analytical Cytology* **55**, 30--42, doi:10.1002/cyto.a.10060 (2003).

43 Kellogg, R. M. The crystallization behavior of proline and its role in asymmetric organocatalysis. *Angewandte Chemie (International ed. in English)* **46**, 494--497, doi:10.1002/anie.200603028 (2007).

44 Klussmann, M. *et al.* Thermodynamic control of asymmetric amplification in amino acid catalysis. *Nature* **441**, 621--623, doi:10.1038/nature04780 (2006).

45 Klussmann, M., White, A. J. P., Armstrong, A. & Blackmond, D. G. Rationalization and prediction of solution enantiomeric excess in ternary phase systems. *Angewandte Chemie (International ed. in English)* **45**, 7985--7989, doi:10.1002/anie.200602520 (2006).

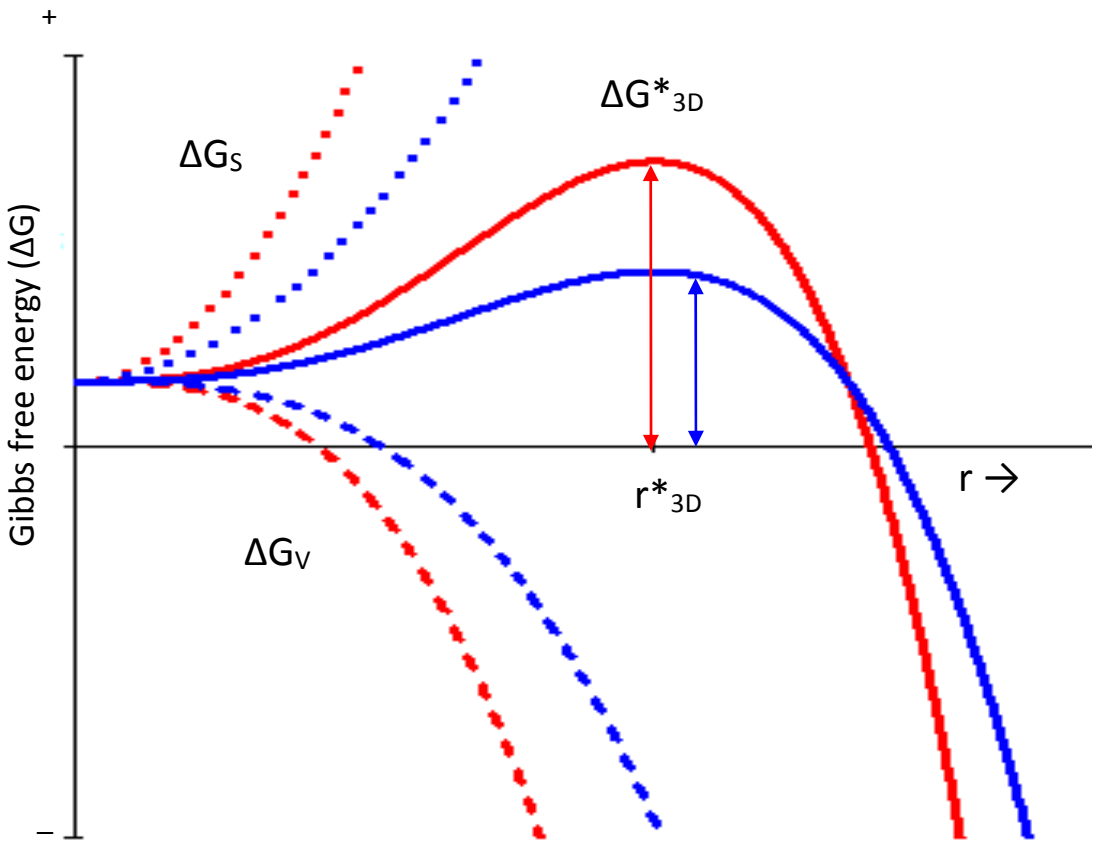

Figure 2.1: The change in Gibbs free energy change (ΔG) as a function of the radius of the cluster. Solid lines are the net free energy change of a cluster as a function of radius. The surface (dotted) and bulk (dashed) free energy represent the positive and negative contributions to the total energy. The critical radii (r^*_{3D}) and the corresponding (ΔG^*_{3D}) for two different polymorphs correspond to the maxima in the solid traces.

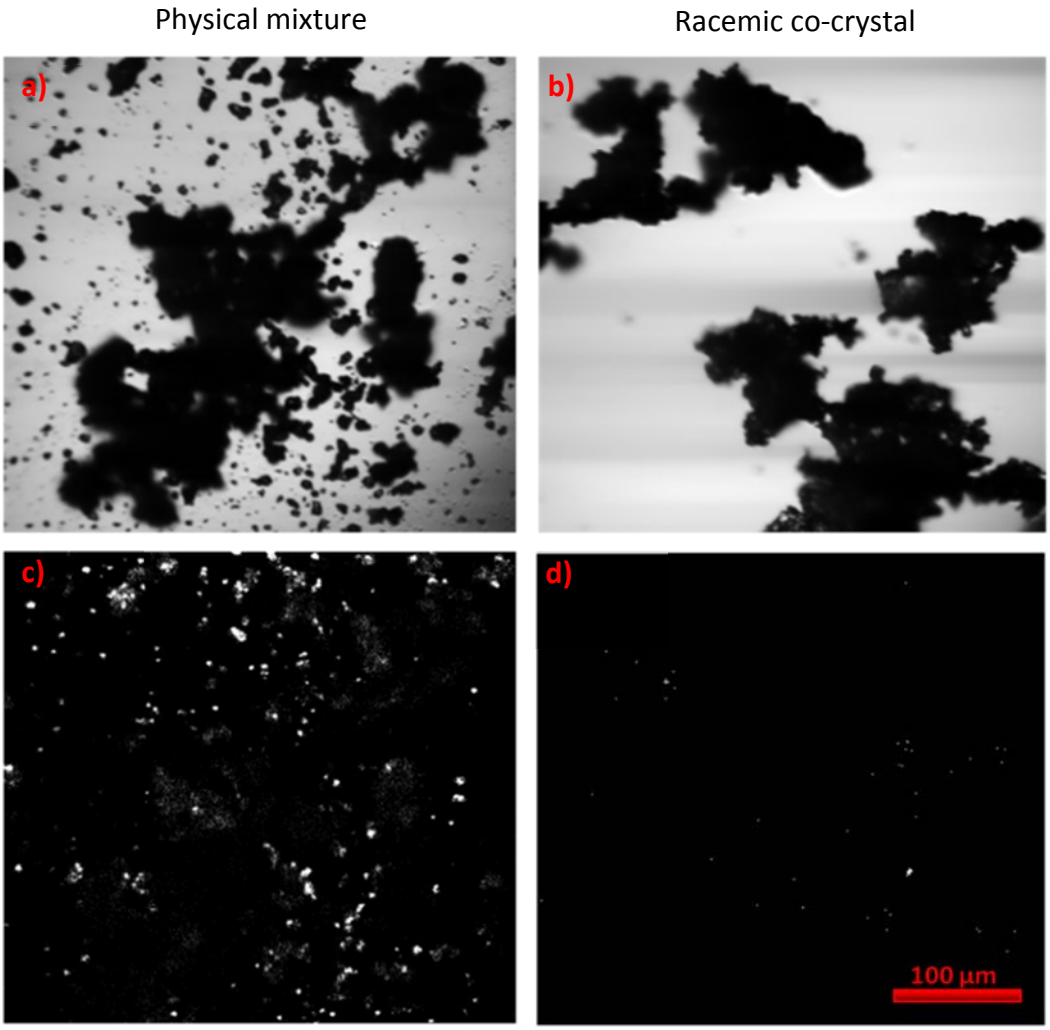

Figure 2.2: Laser transmittance and SHG images of racemic proline, obtained from two different conditions. The physical mixture (Figure 2a and 2c) was made by grinding equal amounts of D and L proline in a mortar and pestle. Overnight crystallization of saturated racemic proline solution produces white racemic co-crystals (Figure 2b and 2d), which was also crushed in a mortar and pestle for imaging. Racemic crystals did not produce any detectable SHG signals.

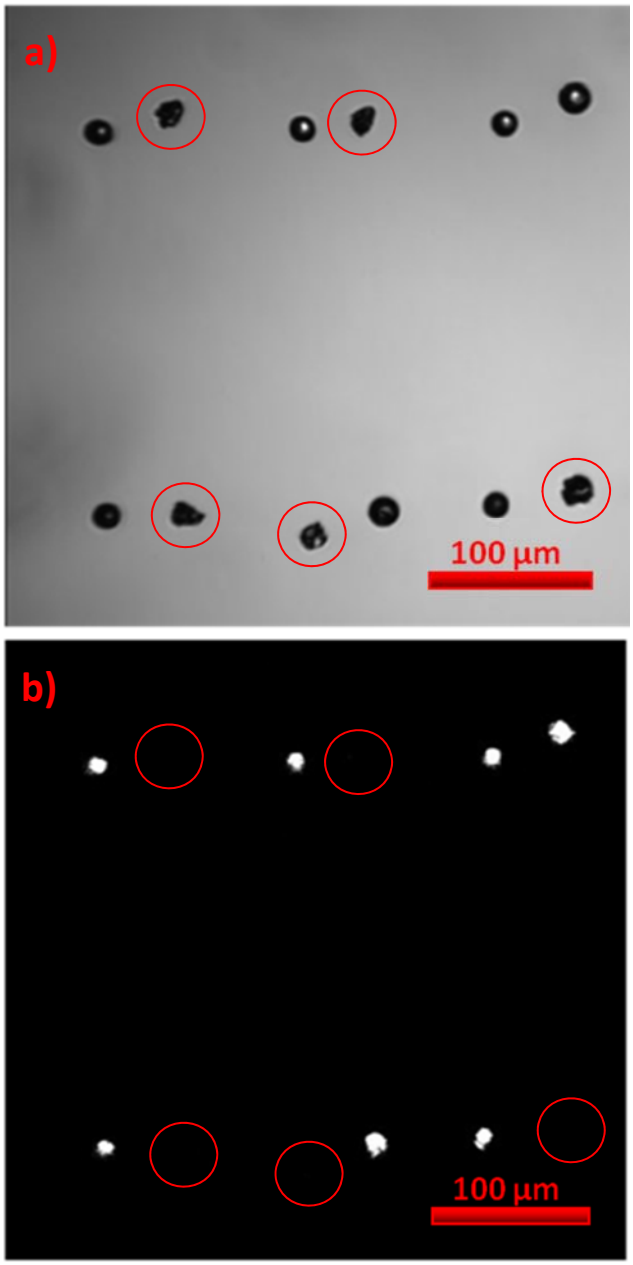

Figure 2.3: Bright-field and SHG images of dot matrix printed racemic solution. There are twelve dots of racemic proline in the field of view. Seven of them formed round shaped dot while the remaining five formed jagged shapes. Only round shaped dot generated substantial amounts of SHG.

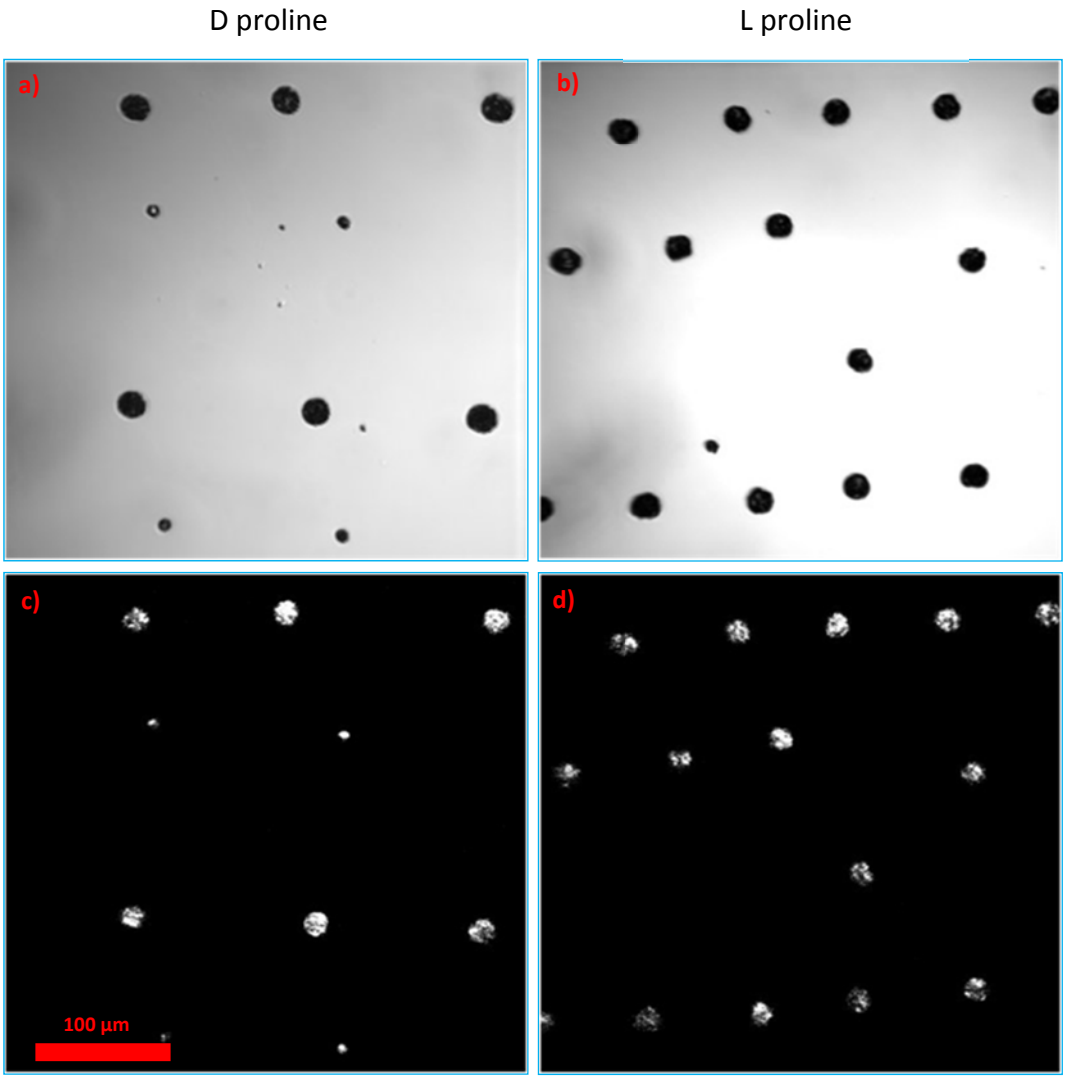

Figure 2.4: Bright-field and SHG image of inkjet printed D- and L-proline. The left column corresponds to D-proline printed dots and the right column corresponds to L-proline printed dots. All the dots in the field of view are SHG active.

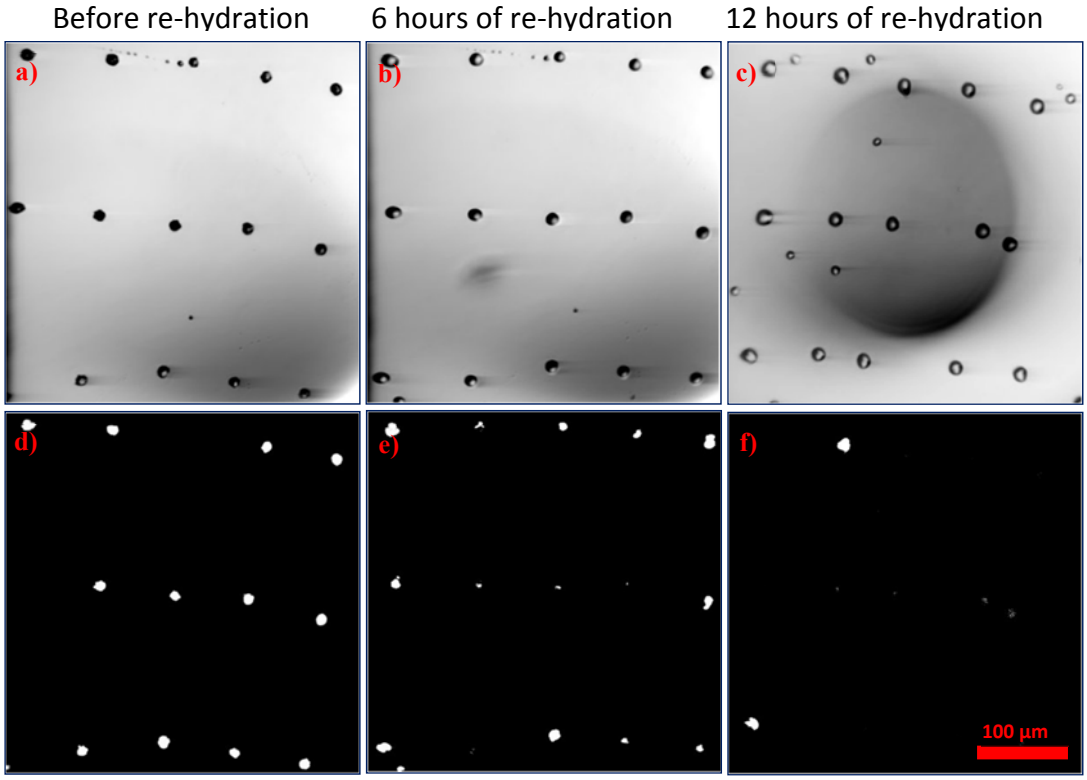

Figure 2.5: Laser transmittance and SHG images of re-hydration of inject printed metastable polymorph of proline produced from racemic solution. In row 2, 1st, 2nd, and 3rd column shows the attenuation of the SHG activity as a function of time upon rehydration.

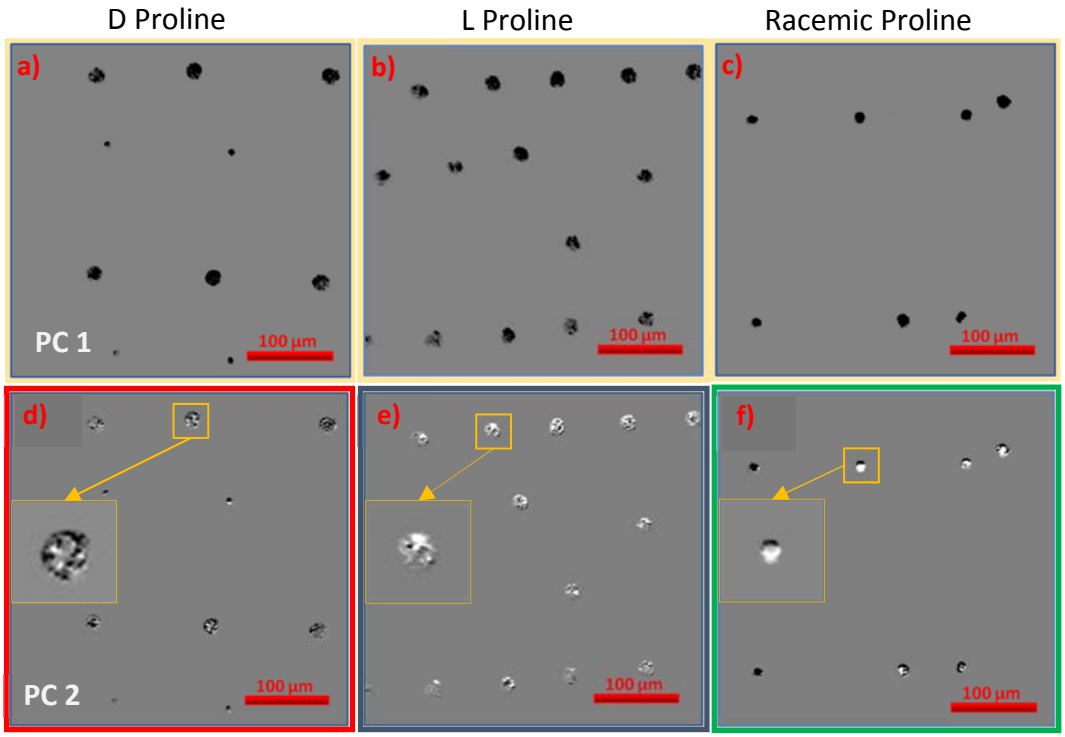

Figure 2.6: Images of the first two principle components of inkjet printed proline. a-c corresponds to principle component 1 and d-f correspond to principle component 2. g) shows a histogram of all SHG active D-, L-, and racemic proline crystals. PC1 corresponds mostly to overall signal intensity, and PC2 corresponds mostly to the polarization dependent SHG response. D- and L- crystals give similar overall intensity, and were separable only in their polarization dependent response. Racemic proline had a less characteristic polarization dependent response, but was characteristically brighter than D- and L- crystals.

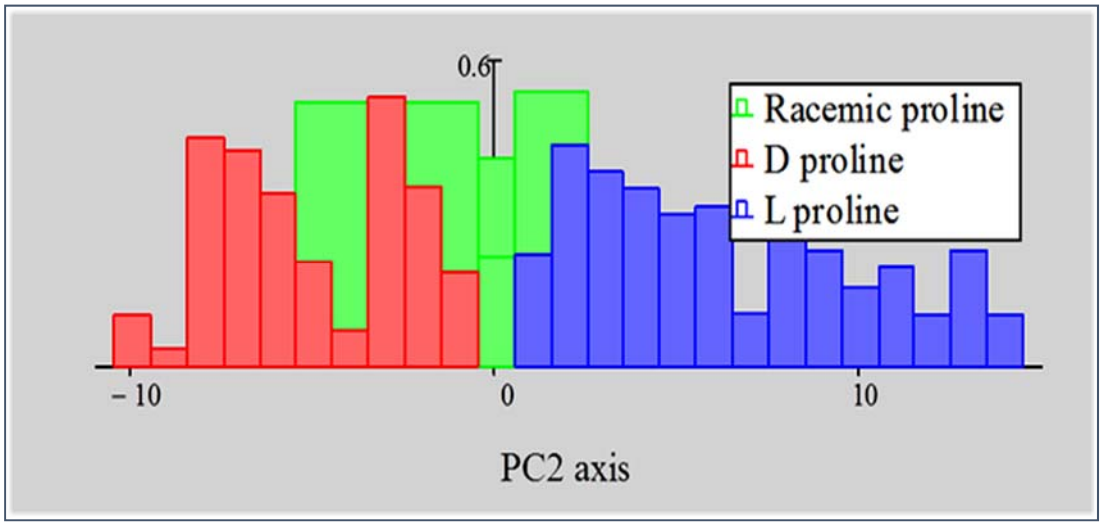

Figure 2.7: Histogram of pixels containing PC2 of all SHG active D-, L-, and racemic proline crystals. PC2 corresponds mostly to the polarization dependent SHG response therefore, D- and L- crystals were separable only in their polarization dependent response but the Racemic proline had a less characteristic polarization dependent response overall.

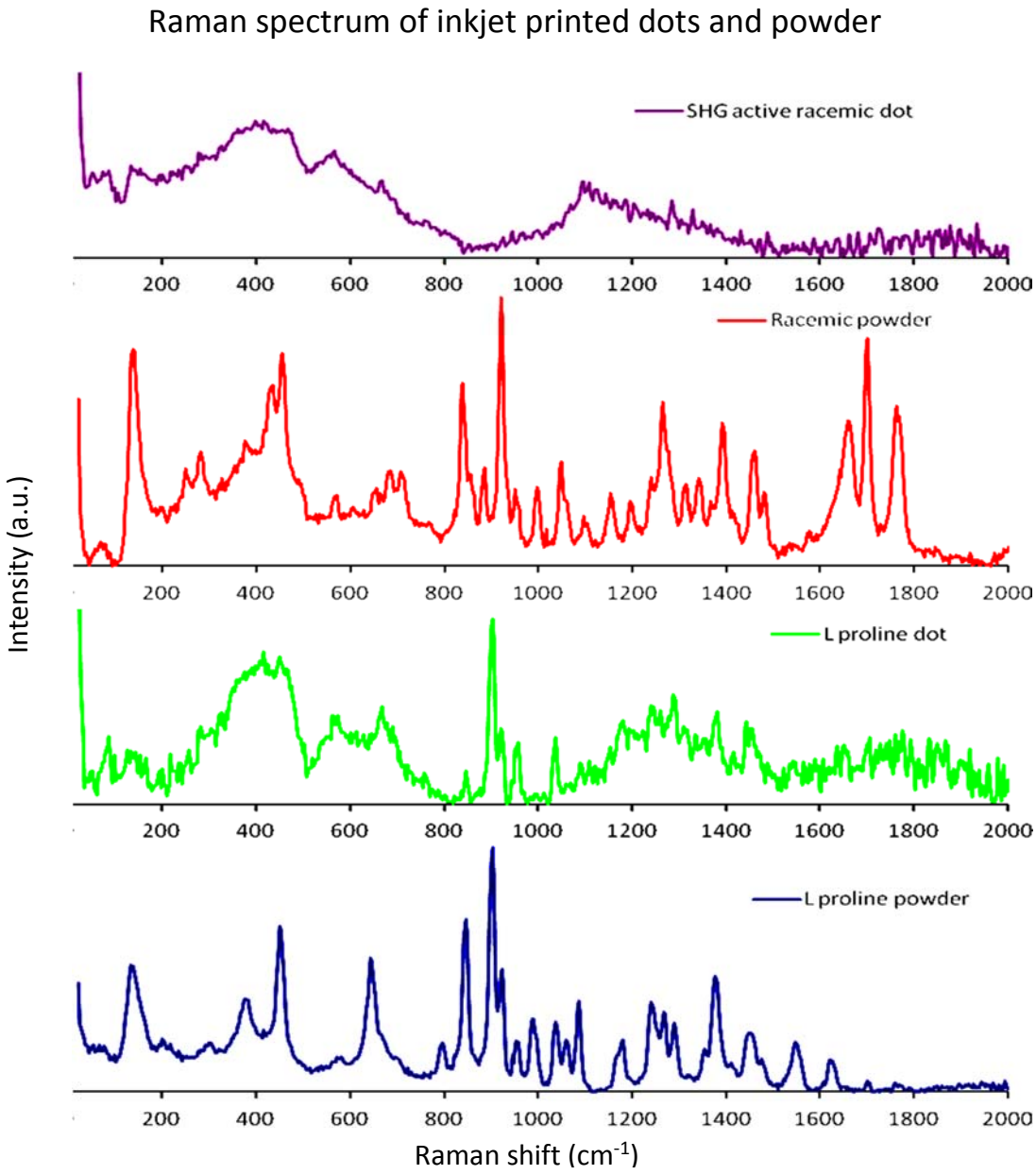

Figure 2.8: Confocal Raman spectrum of L proline powder and all other Inkjet printed proline solutions.

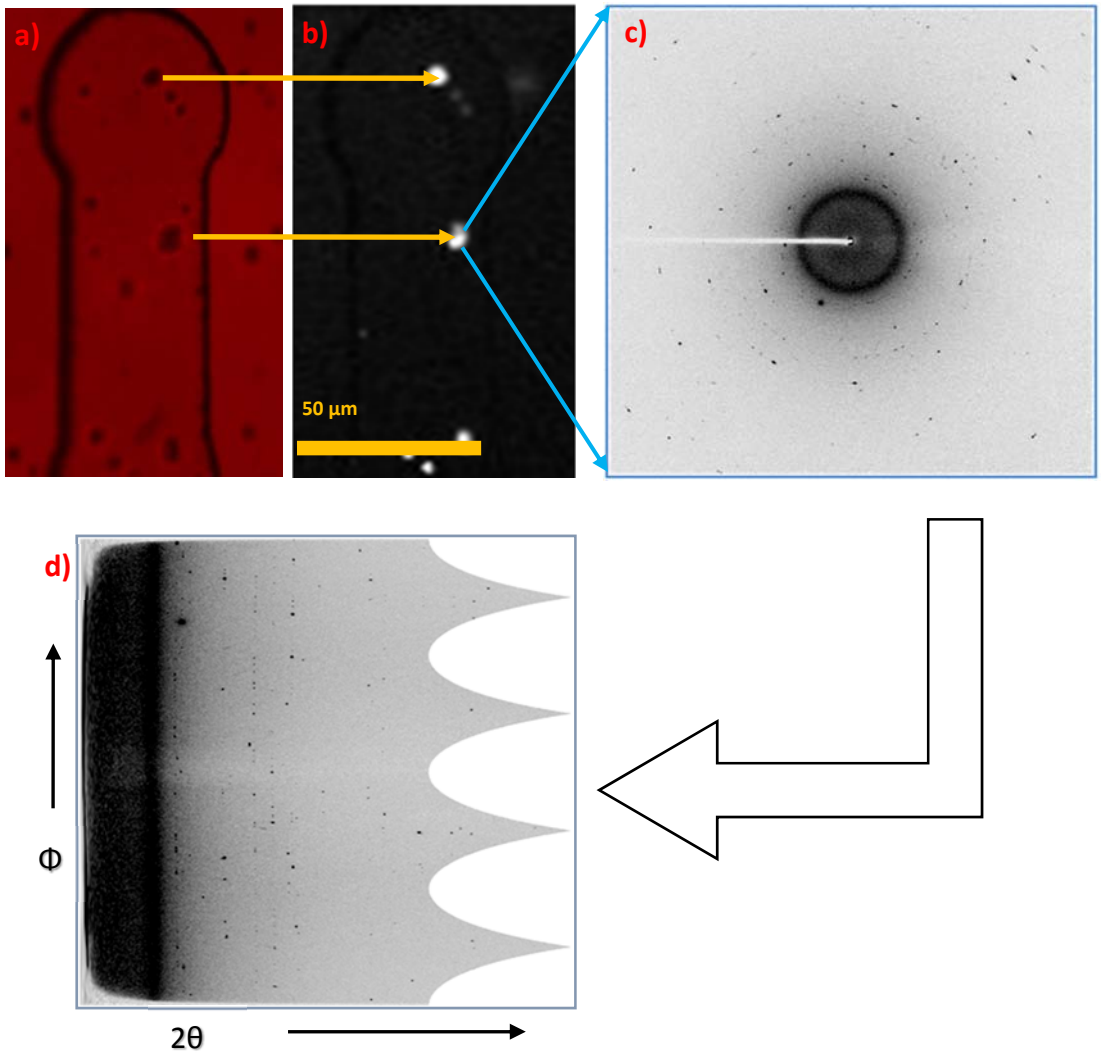

Figure 2.9: Diffraction image analysis of inkjet printed racemic solution. Panels a) and b) are laser bright field and SHG image of inject-printed L-proline on a micro tip, respectively. The white spots in b) are the SHG active inkjet-printed drops. The x-ray diffraction image of a single 10x10 µm spot obtained from the center of the corresponding SHG active droplet is shown in c). Dark spots in this diffraction image correspond to high signal to noise diffraction peaks arises from the crystal. The diffraction image remapped into polar coordinates is shown in d), in which ϕ is the azimuthal rotation angle and 2θ is the proportional to the distance from the image center, corresponding to the location of the un-diffracted beam.

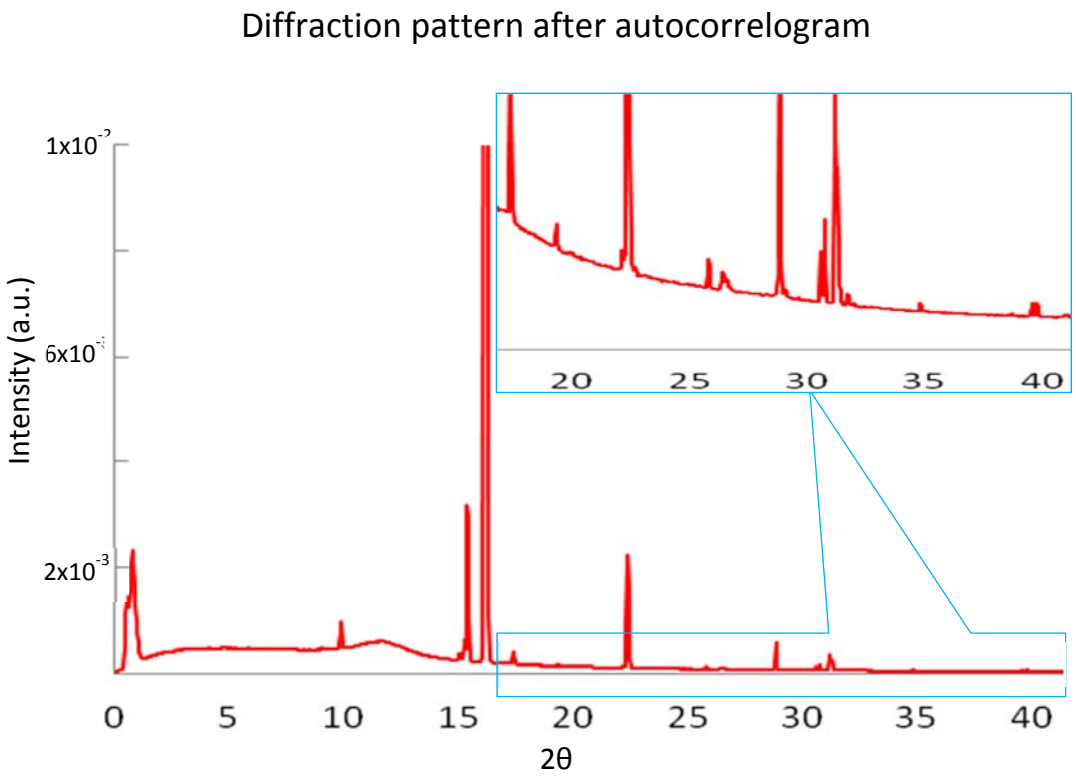

Figure 2.10: Recovered diffraction peaks after autocorrelation along the azimuthal direction, followed by integration over the baseline-subtracted autocorrelogram. High signal to noise of the diffracted peak are shown in the inset.

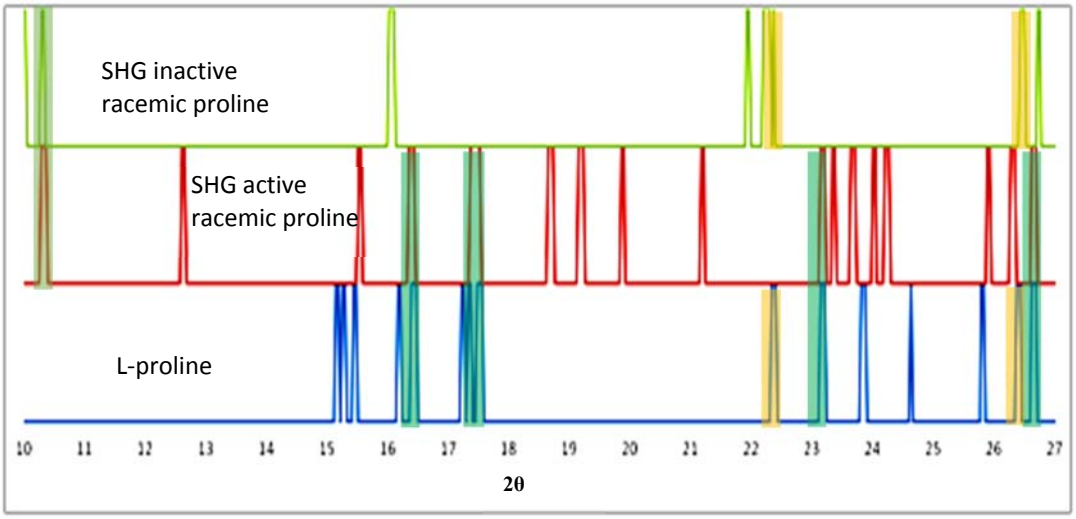

Figure 2.11: Comparison of the XRD peak positions. Diffraction peaks of SHG inactive racemic dot are on top row, SHG active racemic dots are in the middle row, and SHG-active dot of L-proline are in the bottom row. The peaks correspond to locations of diffraction exhibiting S/N>100. Intensities were omitted as orientational affects make these non-trivial to compare. Purple shading indicates regions were L-proline peaks match the SHG inactive racemate spots, green highlights where L-proline and the SHG active racemate spots match, and orange highlights where the two racemates share peaks missing from the L-proline samples.

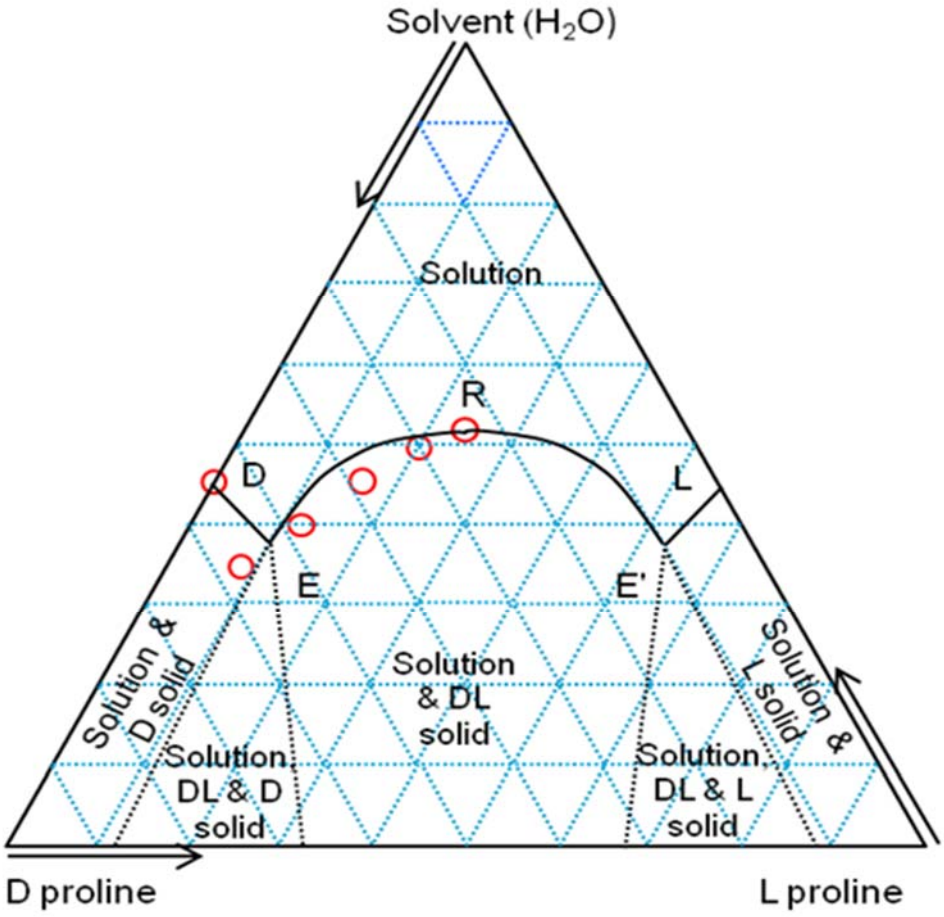

Figure 2.12: Ternary phase diagram of D-proline, L-proline and H_2O at 25°C. Experimental data points (red circles) are plotted in this tri-plot according to their mass percentage and it is assumed that the data points are symmetric about the vertical axis. The solid lines connecting the points DER and RE'L represents the saturated solution and E, E' are the eutectic composition. The eutectic mass percentage was found 74%, calculated from the solubility of homochiral and racemic proline.

Table 2.1: Statistical details of bright field and SHG images of inkjet printed dot matrices of proline solution. Uncertainties correspond to 95% confidence intervals.

proline	Average area in Bright-field (pixels)	SHG active area (pixels)	SHG active area (%)	Avg. SHG intensity (counts)
D proline	375±3	310±3	83±1	9±2
L proline	336±4	270±4	80±2	6±2
Racemic proline	235±4	137±4	58±2	45±6

Table 2.2: Percentage of area under the peak at the corresponding diffraction angle of each PXRD.

2θ	L proline	SHG active racemic	SHG silent racemic
10.33	0.0%	4.9%	0.1%
15.51	0.5%	0.3%	0.0%
16.46	1.3%	12.4%	0.0%
17.51	11.4%	22.3%	0.0%
22.37	5.5%	0.0%	0.1%
23.24	3.6%	12.2%	0.0%
26.49	2.4%	0.0%	0.4%
26.72	6.4%	17.2%	0.0%

CHAPTER 3. EXCITON COUPLING MODEL FOR THE EMERGENCE OF SECOND HARMONIC GENERATION FROM ASSEMBLIES OF CENTROSYMMETRIC MOLECULES

3.1 Introduction

In the design of novel organic materials for nonlinear optical applications, it initially appears irrational to consider approaches using molecular building blocks in which SHG-activity is strictly forbidden by symmetry.[1] However, several recent studies have reported the observation of bright SHG from appropriately arranged assemblies of centrosymmetric or nominally centrosymmetric molecules.[2-6] The rational use of purely centrosymmetric molecules as building blocks for performing frequency doubling and mixing has the potential to open up entirely new synthetic strategies for the design of organic NLO materials. Rational design hinges first on elucidation of the dominant mechanisms driving the nonlinear optical response. However, the macromolecular mechanism underlying the emergence of SHG-activity still remains a somewhat open question.

In one example using squaraines, SHG activity was observed from Langmuir-Blodgett films prepared using centrosymmetric chromophores.[2-6] The presence of SHG activity was attributed to symmetry breaking from inter-chromophore coupling.[7] An

intermolecular charge transfer mechanism was proposed in the case of the squaraines, in which two monomers form a T-shaped dimer. However, the actual structures of the squaraine multimers are not known, given the challenges of obtaining high-resolution structures of single monolayer organic films. While charge transfer is a sufficient condition for the presence of SHG, it is not a necessary one. It is difficult to exclude alternative chromophore dimer architectures that may produce SHG-activity through coupled interactions without additional molecular-level information on the structures produced through intermolecular interactions. Within crystals of related squaraines, the monomers adopt π-stacked dimer structures,[8] or π-stacked herring-bone structures[9] within the extended lattice, rather than T-shaped intermolecular structures.

In other work, vibrational sum-frequency generation (SFG) was observed from the liquid/air interface of benzene and other centrosymmetric liquids,[10,11] studied both experimentally and theoretically.[12,13] Several effects were considered to explain these observations. The observation of SFG from the benzene/air interface was first reported by Allen and coworkers, who attributed the signal to the symmetry-breaking from intermolecular coupling and/or benzene dimer formation.[10] In work by Morita and coworkers, molecular dynamics calculations were coupled with interfacial hyperpolarizability and normal mode analysis, concluding that symmetry breaking within the interfacial benzene molecules themselves was sufficient to explain the observed vibrational SFG without the need for dimerization, although bulk quadrupole contributions were also predicted to be of comparable magnitude.[12] More recently, Tahara and coworkers reported experimental results suggesting that the observed vibrational SFG from benzene may be dominated by bulk quadrupole effects.[10-12]

In related SHG microscopy studies of centrosymmetric carotenoids, bright SHG has recently been reported from H-aggregates of astaxanthin.[14] The astaxanthin monomers are centrosymmetric with little conformational freedom, with the known thermodynamically stable crystal form also adopting a centrosymmetric SHG-inactive lattice.[15] In addition, astaxanthin does not have a donor-acceptor-donor structure that would support partial charge-transfer intermolecular interactions. As such, the nature of the intermolecular interactions driving SHG are not trivially obvious.

Irrespective of the particular structure adopted by the dimer/multimer in the squaraines or the carotenoids, the SHG-activity can likely be attributed to electronic perturbations as a consequence of intermolecular interactions. Given that the intermolecular interactions are relatively weak compared to the intramolecular interactions driving bond formation, a perturbation theoretical approach is likely to be appropriate for treating the emergence of SHG activity. Using the nonlinear optical properties of the unperturbed monomer as a starting point, the introduction of perturbations to the electronic structure can be described within the context of exciton coupling theory.[16-19]

In the present work, this simple exciton coupling approach is developed to provide a framework for describing the emergence of nonzero hyperpolarizability in noncentrosymmetric dimers of centrosymmetric molecules, serving as the foundation for predictions of larger extended clusters and aggregates. Dimer interactions form the foundation for interpreting extended multimeric intermolecular interactions, in addition to being interesting in their own right. They also have the advantage of being the smallest computationally tractable unit for describing intermolecular interactions. Quantum chemical calculations in a simple model system comprised of two coupled butadiene

monomers provide a framework for evaluating the strengths and limitations of the zero order exciton coupling description. Based on the predictions of the model, crystals were prepared from centrosymmetric 2,6-di-tertbutyl-anthraquinone (TAQ) and tested experimentally by SHG microscopy.

3.2 Theoretical Foundation

A framework for interpreting the predicted emergence of SHG-activity due to coupling is proposed based on molecular orbital descriptions of the exciton states in the dimer. In centrosymmetric molecules, all vibrational and electronic transitions are exclusively one-photon or two-photon (including Raman) allowed, but not both. The absence of SHG can be interpreted within the context of this one-photon versus two-photon exclusivity. The molecular hyperpolarizability $\beta^{(2)}$ tensor underlying SHG can be described by a summation over products of one-photon transition moments μ and two-photon transition matrices α, provided the contributing high-energy excited states correspond to frequencies near or above the second harmonic frequency.[17,20,21]

$$\beta^{ijk}\left(-2\omega;\omega,\omega\right)=\sum_{n}S_{n}\left(2\omega\right)\mu_{0n}^{i}\alpha_{n0}^{jk} \tag{1}$$

The above equation will break down in systems exclusively exhibiting one-photon resonance enhancement or in systems not initially in the ground state, but can be considered to be an excellent approximation under most practical experimental conditions. In Eq.1, $S(2\omega)$ is a complex-valued lineshape function. In the case of Lorentzian lineshapes, $S(2\omega)$ is given by the following equation.

$$S_n(2\omega) = \frac{1}{\hbar} \cdot \frac{1}{\omega_n - 2\omega - i\Gamma_n} \tag{2}$$

In Eq. 2, $\hbar\omega_n$ is the transition energy between the ground state and the nth excited state, and Γ_n is the damping constant, related to the homogeneous linewidth. From inspection of Eq.1, the requirement that transitions be either one-photon or two-photon allowed clearly results in zero-values for each term in the summation.

Formally, each dimer state (indicated by the subscript *d*) is given by summations over all the monomer excited states (indicated by *m*), but with the largest contributions arising from those closest in energy.

$$\Psi_d = \sum_m c_m \left(\psi_m^1 \mp \psi_m^2 \right) \tag{3}$$

So far, nothing yet has helped describe the emergence of SHG-activity. If mixing only arose between the states as indicated by the solid lines in Figure 3.2, the μ and α terms for each exciton state in the dimer could be recovered from the sums and differences of μ and α from the corresponding transitions in the monomers. In this limit, the dimer would still exhibit no SHG, since the exciton states arising from one-photon allowed transitions in the monomer would exhibit negligible two-photon absorption, and vice versa.

However, minor contributions from the other monomer excited states are also generally expected (Eq. 3), such that the SHG-activity of the *A* and *B* states can be "turned on" through mixing in of two-photon absorption character into one-photon allowed monomer transitions and vice versa. The specifics of these interactions are detailed in next section.

3.3 Experimental

3.3.1 Computational Methods

Electronic structure of 1,3-butadiene monomers and dimers were calculated using GAMESS package separately. Geometry optimization calculations were used to determine the molecular geometry, then Avagadro software was used to orient the molecule(s) such that the z-axis was the primary axis of rotaion. Configuration Interaction Singles (CIS) calculations were used to compute the electronic resonances of the monomer and dimer separately. Time-Dependent Hartree Fock (TDHF) calculations were used to compute the 1st hyperpolarizability tensor elements on both the monomer and the dimer at 430 nm, 450 nm, and 1000 nm, with the highest energy incident frequency being within 4 nm of the 1st electronic resonance calculated using CIS after frequency doubling. The dimer distance was held at 3.8 Å for all three incident frequencies. Also, at 450 nm incident frequency on the dimer, TDHF calculations were used to compute 1st hyperpolarizability tensor elements at dimer distances of 3.8 Å, 6.0 Å, 8.0 Å, and 60 Å. All calculations used 6-311G basis set. All TDHF calculations obtained both iterative and non-iterative tensor elements, which were in good agreement with each other.

TDHF was selected as it has been shown to recover and describe resonant interactions, unlike conventional HF or DFT.[22,23] The TDHF calculations were all performed for optical frequencies approaching resonance at the second harmonic frequency consistent with the measurements, but still far enough below to avoid complications from singularities that can arise near resonance.

3.3.2 Instrumental

SHG microscopy measurements of TAQ crystals were performed using an instrument described previously.[24-27] In brief, all images were acquired with a built-in-house beam scanning SHG-microscope. Beam scanning was performed with a resonant vibrating mirror (~8 kHz, EOPC) along the fast-scan axis, and a galvanometer (Cambridge) for slow-axis scanning. The 800 nm excitation wavelength by a 80 MHz Ti:sapphire pulsed laser (Spectra-Physics Mai Tai) of 100 fs pulse width was directed through the scan mirrors and focused onto the sample using a 10x objective of working distance 1.6 cm (Nikon, N.A.=0.30). 50 mW laser power was recorded at the sample. SHG signals were collected, with dichroic mirrors and narrow band-pass filters (Chroma HQ400/20 m-2p) centered around 400 nm placed prior to the photomultiplier tube detectors (Burke, XP 2920PC). An in-house written MATLAB code was used to digitize each synchronous laser pulses with strict timing, to control the scanning mirrors and to communicate with the data acquisition electronics. Laser transmittance images were the measurement of the extinction beam by a photodiode. Laser transmission and SHG images were rendered and analyzed with Image J package.

3.4 Results and Discussion

3.4.1 Case Study 1: Butadiene Dimer

Before considering the butadiene dimer, it is useful to start with a review of the electronic structure of the monomer. Butadiene conforms to the C_{2h} point group, which is centrosymmetric and SHG-inactive by symmetry. Based on quantum chemical

calculations, the two lowest energy transitions correspond to a π-π^* HOMO-LUMO transition of B_u symmetry, with the next highest energy transition corresponding to B_g symmetry. As required by symmetry in centrosymmetric molecules, each transition must be allowed for either one-photon or two-photon excitation, but not both. In this case, the B_u transition is one-photon allowed and two-photon forbidden, while the B_g state is one-photon forbidden and two-photon allowed. Quantum chemical calculations of the butadiene monomer confirm these expectations, even when symmetry is not rigorously imposed.

When positioned in a π-stacking configuration such as shown in Figure 3.1, the symmetry of the dimer becomes C_2, with the *A* and *B* states generated from linear combinations of the monomer states. Because of the odd symmetry of the π-orbitals, the difference states are lower in energy than the sum states in π-stacked dimers, consistent with the exciton coupling diagram depicted in Figure 3.2.

The exciton coupling model of a dimer is fully rigorous in the limit of inclusion of all excited states in the summation. In brief, the set of excited states serves as a basis set for recovering the new states in the coupled system. Since the excited states themselves are constructed from a linear combination of fundamental basis set functions, so too are the states produced from exciton coupling. In the limit of weak coupling consistent with intermolecular interactions (as opposed to covalent bond formation), each exciton state of a dimer can be reasonably described by the interactions between just one or two excited states of the monomer. However, the practical need to consider a finite number of excited state couplings can potentially introduce uncertainties in the approach. Consequently, the approach is likely to be most accurate when the coupling between monomers is relatively

weak (such that only a few excited states are required to recover the exciton states) and for molecular systems with a relatively sparse population of spectrally overlapping excited states capable of participation in coupling. These are both reasonable assumptions in the present case.

Unlike the C_{2h} point group, the *A* and *B* states of the dimer can in principle each be both one-photon and two-photon allowed. However, in practice the core nature of the monomer transitions is carried over when describing the excited state transitions in the dimer arising from exciton coupling. Within the validity of this simple exciton coupling description, the most significant contributions to the dimer states will be produced from the sums and differences of the corresponding orbitals of the monomers. For example, considering just the two excited state transitions shown in Figure 3.2, the one-photon transition moment to the first excited B state should be recovered from the vector difference between the two monomer transition moments, resulting in predominantly *y*-polarized transition with an oscillator strength equal to the *y*-component of the monomer multiplied by √2.

The total wavefunction describing the lowest excited state transition in the dimer can be written as a linear combination of both the major one-photon allowed B_u contributions and the minor two-photon allowed B_g contributions.

$$\Psi_B = c_{B_u}\left(\psi^1_{B_u} - \psi^2_{B_u}\right) + c_{B_g}\left(\psi^1_{B_g} - \psi^2_{B_g}\right); c_{B_u} > c_{B_g} \qquad (4)$$

The corresponding transition moments as well as the matrices describing two-photon absorption can be similarly produced from appropriately weighted sums and differences.

$$\begin{aligned}\mu_B &= c_{B_u}\left(\mu^1_{B_u} - \mu^2_{B_u}\right) + c_{B_g}\left(\mu^1_{B_g} - \mu^2_{B_g}\right) = c_{B_u}\left(\mu^1_{B_u} - \mu^2_{B_u}\right) \\ \alpha_B &= c_{B_g}\left(\alpha^1_{B_g} - \alpha^2_{B_g}\right)\end{aligned} \tag{5}$$

Although $c_{B_u} > c_{B_g}$, the presence of a nonzero contribution from the B_g transition provides some two-photon transition character that can drive nonzero values of the hyperpolarizability tensor $\beta^{(2)}$. In this simplified three-state model for the monomer, the hyperpolarizability tensor for the lowest-lying B state is approximated by the following expression.

$$\beta^{ijk}_B = S_B(2\omega)\,\mu^i_B\alpha^{jk}_B \cong S_B(2\omega)\,c_{B_u}\left(\mu^1_{B_u} - \mu^2_{B_u}\right)^i \cdot c_{B_g}\left(\alpha^1_{B_g} - \alpha^2_{B_g}\right)^{jk}; c_{B_u} > c_{B_g} \tag{6}$$

The corresponding tensor contributions for the A states is given by the summation (rather than the difference) between the monomer μ and α terms.

This model suggests several specific predictions that can be compared directly with computational and experimental results.

1. The dominant tensor elements driving the hyperpolarizability in the dimer can be predicted based on the symmetries of the corresponding monomer states contributing to exciton coupling.
2. In the limit of weak inter-chromophore coupling, the SHG-activity should approach zero.
3. The SHG-activity of the dimer should be substantially enhanced close to resonance, but approach zero far from resonance.
4. Significant charge transfer is not expected for the observation of SHG-activity in the dimer.

The first prediction follows directly from the analysis exemplified in Eq. 6. The second is clear conceptually, but potentially less so mathematically. In the limit of weak coupling, the excited state energies of an exciton pair converge to nearly degenerate values. In this limit, it becomes nearly mathematically equivalent to describe the dimer in a basis set consisting of two uncoupled monomers rather than as a coupled dimer. The key criterion has already been established for assessing whether the hyperpolarizability can be considered through the coherent summation of two uncoupled monomers, or if coupling and exciton state descriptions are required. Specifically, coupling should be considered if the energy splitting is comparable or greater than the experimental linewidth of the transition, and can safely be neglected under conditions in which it is not.

The third prediction is closely related to the second. From inspection of Eq. 2, the weighting of each exciton state in the net hyperpolarizability is related to the energy difference between the exciton state and $2\hbar\omega$, where ω is the fundamental frequency. As the second harmonic frequency moves away from resonance, the contribution from each of the exciton states approaches a single constant. For example, the two exciton transition moments from the pair of B_u monomer states each contribute with approximately equal weight, such that the net result is closely approximated by the direct coherent sum of the uncoupled monomers. Correspondingly, in this limit far from resonance the perturbation from exciton coupling becomes negligible.[19,28] Since the unperturbed system of two centrosymmetric monomers is SHG-inactive, the nonresonant result should also converge to that same outcome far from resonance.

The fourth prediction is quite straightforward. Since neither of the monomers possesses a net dipole nor charge transfer character in any of the transitions, little or no

charge transfer is expected in the exciton states produced from sums and differences of those same monomer states.

The predictions of the exciton coupling model were compared with the results of quantum chemical calculations of the linear and nonlinear optical properties of the butadiene monomer as a point of reference for interpreting the NLO properties of the dimer structures. CIS calculations for the monomer were performed and are summarized briefly in the Supporting Information. In brief, the lowest lying excited state corresponds to a transition of B_u symmetry, consistent with the presence of a transition moment polarized within the *xz* plane using the coordinate system indicated in Figure 3.2. The next highest excited state is one-photon forbidden, suggesting either A_g or B_g symmetry. The symmetry is tentatively assigned as B_g based on trends in the dimer detailed below.

The butadiene structure considered computationally was one in which just one pair of carbon atoms were coparallel and π-stacked, as shown in Figure 3.2. In this configuration, the butadiene dimer has C_2 symmetry. A summary of the linear optical properties of the dimer is provided in the Supporting Information.

As a simple confirmatory test, the hyperpolarizability as a function of intermolecular separation is shown in Figure 3.3. As one might expect, the magnitude of each hyperpolarizability tensor element uniformly decreases as the intermolecular distance is increased, asymptotically approaching a value of zero in the limit of negligible inter-chromophore coupling consistent with the second prediction of the exciton coupling model.

The hyperpolarizability tensor elements as a function of fundamental wavelength are summarized in Figure 3.4. Results for the frequency-dependent dimer calculations clearly demonstrate a trend in which the beta tensor elements are rapidly reduced in

magnitude as the incident wave is shifted further from resonance. Again, this observation is in good agreement with the predictions of the exciton coupling model.

Interestingly, the largest magnitude for the SHG-activity is given in the "chiral" β_{zxy} tensor element with the largest relative enhancement close to resonance. The dominance of this contribution can be understood within the context of the exciton coupling model by considering just the two lowest excited states in the butadiene monomer. The monomer B_u (HOMO-LUMO) transition is polarized within the *yz*-plane of the chromophore and oriented largely along the long *z*-axis of the molecule. The lowest energy B-exciton state in the dimer should be formed from the difference of the two monomer wavefunctions (given the sign difference between the *p*-orbitals), with symmetry dictating that it be *y*-polarized, and with a transition moment roughly $\sqrt{2}$ larger in magnitude than the monomer, in excellent agreement with the quantum chemical calculations. Similarly, the next highest excited state in the dimer should consist of the sum of the monomer wavefunctions, corresponding to an A-state with a *z*-polarized transition moment. The major contributions to this pair of A and B states will arise from coupling primarily from just the two one-photon allowed monomer B_u states. However, the dimer A and B states can also borrow minor contributions from the next highest two-photon allowed excited state of B_g symmetry. For a transition of B_g symmetry, the nonzero TPA tensor elements in the monomer will be α_{xy} and α_{xz}, the first of which can contribute exclusively to A-states in the dimer, and the second exclusively to B-states.

Combining the nonzero elements of μ and α according to Eq. 1, the lowest energy dimer transition should be dominated by the β_{yxz} tensor element (nonzero μ_y and borrowed α_{xz}), and the next highest transition dominated by the β_{zxy} tensor element (large μ_z and

borrowed α_{xy}). Given the larger one-photon transition moment along the long monomer *z*-axis, it is not surprising that the second excited state in the dimer corresponding to the β_{zxy} tensor element drives much of the NLO activity near resonance.

These combined conditions predict relatively large contributions from the "chiral" tensor elements, in reasonably good agreement with the computational results. The tensor elements β_{zyx} and β_{yxz} are larger in magnitude than all other tensor elements (at all three wavelengths considered). For example, the next most significant tensor element was β_{zzz}, presumably arising from the large μ_z from the B_u monomer transition coupled with α_{zz} contributions from the next higher excited states of B_g symmetry.

The steep sensitivity of the calculated hyperpolarizability with fundamental wavelength indicated in Figure 3.3 is noteworthy. This trend is consistent with the molecular orbital diagram depicted in Figure 3.2, assuming the "borrowing" of the one-photon and two-photon contributions goes both ways in this two-excited state limit. While the lowest two excited states of the dimer yield nonzero values for β_{yxz} (nonzero μ_y and borrowed α_{xz}) and β_{zxy} (large μ_z and borrowed α_{xy}), the next highest exciton pair will similarly be driven largely but equal and opposite contribution to those same tensor elements β_{yxz} (borrowed μ_y and nonzero α_{xz}) and β_{zxy} (borrowed μ_z and nonzero α_{xy}). The requirement that they sum to approximately zero in the two-excited state model arises simply by nature of the centrosymmetry of the monomers from which the dimer states were generated. Of course, additional excited states are also present and contributing, but the general sensitivity to resonance-enhancement in the dimer can still be qualitatively understood within the context of this argument.

3.4.2 Case Study 2: 2,6-di-tertbutyl-anthraquinone (TAQ) Crystals

Crystals of TAQ form a particularly useful benchmark to test the exciton coupling model. The particular set of nonzero tensor elements generated from exciton coupling depend solely on the relative orientation, and not their relative position.[15] The magnitudes of the tensor elements are affected by the degree of coupling, but not which tensor elements are nonzero. Consequently, the allowed tensor elements are arguably most easily identified by considering first structures for the TAQ dimer with different relative positions between the monomers. Based on a previously published crystal structure, TAQ forms a centrosymmetric, SHG-inactive crystal structure of $P_{\bar{1}}$ symmetry, in which every monomer is in exactly the same orientation within the lattice and each monomer is centrosymmetric.[29] Considering a dimer formed from two monomers of identical orientation, the wavefunctions for the sum states will simply be identical but rescaled, and all the difference states will be zero-valued. As such, the SHG activity of the TAQ dimer and crystal is interesting to interpret within the context of the exciton coupling model. Considering a dimer comprised of two monomers offset in space by not rotated, the symmetry of the dimer is formally C_i and should result in no SHG activity.

In SHG measurements of TAQ powders as received (Figure 3.5), the large majority (~92.6% of the total area in the field of view) was SHG-inactive as expected based on the known crystal form. Consequently, the absence of significant SHG from the large majority of the TAQ powder is in excellent agreement with both the established bulk crystal symmetry and the exciton coupling arguments.

Since the established crystal structure for TAQ material is symmetry-forbidden for SHG,[30] it is particularly noteworthy that strong SHG is nevertheless observed from

localized domains within the powdered sample. While the large majority of the TAQ powder is SHG-inactive consistent with expectations, approximately 7.4% of the total area in Figure 3.5a is occupied by SHG-active domains, representing a small but significant total volume fraction of the material. The SHG activities of the TAQ crystals rival those of $BaTiO_3$, used as a reference material. Recrystallization by rapid desolvation resulted in a ~10-fold increase in the integrated SHG activity of the TAQ powder per unit area, shown in Figure 3.5d.

Following recrystallization, the SHG-active TAQ crystals were placed in a sealed container with a saturated vapor pressure of 1,4-dioxane (the solvent used in the initial crystallization), then re-imaged after 3 days at room temperature (Figure 3.5e, 3.5f). Over this time-frame, the SHG activity of the sample within the same field of view was reduced 27-fold to levels similar to those observed initially within the crystalline powder.

The observation of such a reduction in SHG upon solvent vapor exposure strongly suggests the absence of significant bulk-allowed quadrupolar or magnetic dipole origins for the observed SHG signals. Both higher-order effects arise with comparable efficiency for both centrosymmetric and noncentrosymmetric media. As such, their contributions would be unlikely to be perturbed by the solvent-mediated recrystallization. This observation is in noteworthy contrast to vibrational SFG measurements of the benzene/air interface, in which calculations and measurements suggest quadrupole effects may be significant.[9,10] Furthermore, SHG arising from trace impurities can similarly be excluded, as they would be present in equal quantities before and after exposure to solvent vapor. In addition, the SHG intensity produced by TAQ rivals that of the noncentrosymmetric bulk

dipole-allowed $BaTiO_3$ reference, which strongly suggests a bulk-allowed electric dipole origin if the observed signal.

Given the steep dependence on the preparation method, the SHG arising from the TAQ following recrystallization is attributed to the production of at least one alternative new noncentrosymmetric crystal form. In previous studies, it has been shown that rapid solvent evaporation can promote the formation of metastable polymorphs by placing crystallization under kinetic control rather than thermodynamic control.[30,31] The observed loss in SHG activity shown in Figure 3.5 following exposure of the crystals to solvent vapor is in good agreement with this explanation, as adsorbed solvent films can facilitate the interconversion between different crystalline solvates and/or polymorphs.[32]

Two possible mechanisms for the observed bright SHG-activity within the TAQ crystals are considered. First, intermolecular interactions could be distorting TAQ to break the molecular inversion symmetry. This mechanism can be excluded by inspection of the structure of TAQ, which consists of a rigid ring with significant flexibility only in the t-butyl rotation angles. It is unlikely that the relatively weak intermolecular interactions driving crystal packing will substantially distort the centrosymmetric ring structure driving the nonlinear polarizability of TAQ. It is equally unlikely that a noncentrosymmetric eclipsed configuration for the t-butyl groups as opposed to the centrosymmetric staggered configuration would exhibit substantially enhanced nonlinear optical activity of the monomer. Consequently, the observation of SHG activity is attributed to intermolecular exciton coupling interactions within a noncentrosymmetric lattice.

The observation of bright SHG from TAQ crystals confirms the presence of significant intermolecular interactions within the lattice, but is not alone sufficient to

exclusively confirm the exciton coupling model and exclude alternative mechanisms such as charge transfer. Of course, a charge transfer complex is really just a specific example of exciton coupling in which the monomers are in asymmetric positions rather than the symmetric structures considered computationally in the present work. Without more detailed knowledge of the structures within the T, we can only state that the observation of SHG is consistent with the predictions of the model, and that the exciton model imposes the least requirements in terms of specific structures produced than alternative hypotheses, such as charge transfer

It is interesting that the regions of high SHG in TAQ were brighter than the $BaTiO_3$ reference materials. Given that the molecular building block is forbidden by symmetry to produce SHG, such bright signals are clear indicators of intermolecular interactions within the lattice as a key driving influence. The influence of these interactions is likely further increased through resonance-enhancement. The low lying transitions in TAQ approach energies correspond to the twice the incident photon energy, while $BaTiO_3$ is transparent throughout the visible spectrum.

The presence of an SHG-active form for the TAQ crystals is in excellent qualitative agreement with the exciton coupling model described herein. While the packing arrangement within this new polymorph is not yet established, for the present purposes it is sufficient to note that it is clearly and strongly SHG-active, despite being produced from a centrosymmetric molecular building block.

3.5 Conclusion

A model based on exciton coupling theory was developed for interpreting the emergence of SHG in assemblies of centrosymmetric monomers. From the one-photon transition moments and two-photon absorption tensors within the monomer, the relative magnitudes and polarization-dependences of the hyperpolarizability tensor elements describing the exciton states can be predicted based solely on the relative orientation of the monomers. The degree of energy splitting between the resulting exciton states is dependent on the coupling strength between the monomers. This approach was tested computationally using TDHF and CIS calculations on both the monomer and dimer of 1,3-butadiene, with good agreement between the predictions of the model based on the monomer optical properties and the quantum chemical calculations of the dimers. Specifically, the signs and relative magnitudes of the different $\beta^{(2)}$ tensor elements predicted from the monomer and calculated for the dimer were in good agreement, indicating β_{zxy} as the dominant tensor contribution in the dimer at optical wavelengths. Additional experimental support for the exciton model was found in studies of TAQ crystals, in which the both SHG-active and SHG-inactive forms were found experimentally. Since TAQ is itself centrosymmetric with little conformational flexibility within the chromophore, the observation of relatively strong SHG from the metastable crystals is consistent with an exciton coupling mechanism to produce SHG-active crystalline forms.

3.6 References

1 Boyd, R. W. *Nonlinear Optics*. 3rd edn, (Academic Press, 2008).

2 Ashwell, G. *et al.* Strong second-harmonic generation from centrosymmetric dyes. *Nature* **375**, 385-388 (1995).

3 Ashwell, G. J., Dyer, A. N., Green, A., Sato, N. & Sakuma, T. Monolayer films of U-shaped molecules: suppression of the aggregation-induced second-harmonic generation of squaraine dyes by guest–host interactions. *Journal of Materials Chemistry* **10**, 2473-2476 (2000).

4 Ashwell, G. J., Williamson, P. C., Bahra, G. S. & Brown, C. R. 2,Bis4-(Dihexadecylamino)-2-Hydroxyphenyl-Squaraine: Second-harmonic Generation from Langmuir-Blodgett Monolayers of a Centro-Symmetric Dye in Which the Chromophores are Isolated from the Substrate. *Australian journal of chemistry* **52**, 37-41 (1999).

5 Beverina, L. *et al.* Second harmonic generation in nonsymmetrical squaraines: tuning of the directional charge transfer character in highly delocalized dyes. *Journal of Materials Chemistry* **19**, 8190-8197 (2009).

6 Honeybourne, C. Charge distortion by sparkles can explain strong SHG by centrosymmetric squaraine dyes. *Journal of Materials Chemistry* **9**, 2241-2244 (1999).

7 Honeybourne, C. A mechanism for strong SHG by centrosymmetric anilinosquaraine dyes. *Advanced Materials* **11**, 1477-1480 (1999).

8 Beverina, L. *et al.* Indolic squaraines as two-photon absorbing dyes in the visible region: X-ray structure, electrochemical, and nonlinear optical characterization. *Chemistry of materials* **20**, 3242-3244 (2008).

9 Colin, H. 2, 4-Bis [4-(N, N-dibutylamino) phenyl] squaraine: X-ray crystal structure of a centrosymmetric dye and the second-order non-linear optical properties of its non-centrosymmetric Langmuir–Blodgett films. *Journal of Materials Chemistry* **6**, 23-26 (1996).

10 Hommel, E. L. & Allen, H. C. The air–liquid interface of benzene, toluene, m-xylene, and mesitylene: a sum frequency, Raman, and infrared spectroscopic study. *Analyst* **128**, 750-755 (2003).

11 Matsuzaki, K., Nihonyanagi, S., Yamaguchi, S., Nagata, T. & Tahara, T. Vibrational sum frequency generation by the quadrupolar mechanism at the nonpolar benzene/air interface. *The journal of physical chemistry letters* **4**, 1654-1658 (2013).

12 Kawaguchi, T., Shiratori, K., Henmi, Y., Ishiyama, T. & Morita, A. Mechanisms of sum frequency generation from liquid benzene: Symmetry breaking at interface and bulk contribution. *The Journal of Physical Chemistry C* **116**, 13169-13182 (2012).

13 Rivera, C. A. & Fourkas, J. T. Reexamining the interpretation of vibrational sum-frequency generation spectra. *International Reviews in Physical Chemistry* **30**, 409-443 (2011).

14 Tokarz, D. *et al.* Carotenoid based bio-compatible labels for third harmonic generation microscopy. *Physical Chemistry Chemical Physics* **14**, 10653-10661 (2012).

15 Bartalucci, G. *et al.* Unravelling the chemical basis of the bathochromic shift in the lobster carapace; new crystal structures of unbound astaxanthin, canthaxanthin and zeaxanthin. *Acta Crystallographica Section B: Structural Science* **63**, 328-337 (2007).

16 Gualtieri, E. J., Haupert, L. M. & Simpson, G. J. Interpreting nonlinear optics of biopolymer assemblies: Finding a hook. *Chemical Physics Letters* **465**, 167-174 (2008).

17 Perry, J. M., Moad, A. J., Begue, N. J., Wampler, R. D. & Simpson, G. J. Electronic and vibrational second-order nonlinear optical properties of protein secondary structural motifs. *The Journal of Physical Chemistry B* **109**, 20009-20026 (2005).

18 Simpson, G. J., Perry, J. M., Moad, A. J. & Wampler, R. D. Uncoupled oscillator model for interpreting second harmonic generation measurements of oriented chiral systems. *Chemical physics letters* **399**, 26-32 (2004).

19 Wanapun, D., Wampler, R. D., Begue, N. J. & Simpson, G. J. Polarization-dependent two-photon absorption for the determination of protein secondary structure: A theoretical study. *Chemical Physics Letters* **455**, 6-12 (2008).

20 Davis, R. P., Moad, A. J., Goeken, G. S., Wampler, R. D. & Simpson, G. J. Selection rules and symmetry relations for four-wave mixing measurements of uniaxial assemblies. *The Journal of Physical Chemistry B* **112**, 5834-5848 (2008).

21 Moad, A. J. & Simpson, G. J. Self-consistent approach for simplifying the molecular interpretation of nonlinear optical and multiphoton phenomena. *The Journal of Physical Chemistry A* **109**, 1316-1323 (2005).

22 Korambath, P. & Kurtz, H. A. in *ACS Symposium Series.* 133-144.

23 Van Gisbergen, S., Snijders, J. & Baerends, E. Calculating frequency-dependent hyperpolarizabilities using time-dependent density functional theory. *The Journal of chemical physics* **109**, 10644-10656 (1998).

24 Kestur, U. S. *et al.* Nonlinear optical imaging for sensitive detection of crystals in bulk amorphous powders. *Journal of pharmaceutical sciences* **101**, 4201-4213 (2012).

25 Kissick, D. J., Muir, R. D., Sullivan, S. Z., Oglesbee, R. A. & Simpson, G. J. in *IS&T/SPIE Electronic Imaging.* 86570E-86570E-86577 (International Society for Optics and Photonics).

26 Muir, R. D., Kissick, D. J. & Simpson, G. J. Statistical connection of binomial photon counting and photon averaging in high dynamic range beam-scanning microscopy. *Optics express* **20**, 10406-10415 (2012).

27 Toth, S., Madden, J., Taylor, L., Marsac, P. & Simpson, G. Selective imaging of active pharmaceutical ingredients in powdered blends with common excipients utilizing two-photon excited ultraviolet-fluorescence and ultraviolet-second order nonlinear optical imaging of chiral crystals. *Analytical chemistry* **84**, 5869-5875 (2012).

28 Haupert, L. M. & Simpson, G. J. Chirality in nonlinear optics. *Annual review of physical chemistry* **60**, 345-365 (2009).

29 Franz, A. W., Rominger, F. & Müller, T. J. Synthesis and electronic properties of sterically demanding n-arylphenothiazines and unexpected Buchwald-Hartwig aminations. *The Journal of organic chemistry* **73**, 1795-1802 (2008).

30 Chowdhury, A. U. *et al.* Kinetic trapping of metastable amino acid polymorphs. *Journal of the American Chemical Society* **136**, 2404-2412 (2014).

31 Hall, V. J. & Simpson, G. J. Direct observation of transient Ostwald crystallization ordering from racemic serine solutions. *Journal of the American Chemical Society* **132**, 13598-13599 (2010).

32 Giron, D. *et al.* Solid state characterizations of pharmaceutical hydrates. *Journal of thermal analysis and calorimetry* **68**, 453-465 (2002).

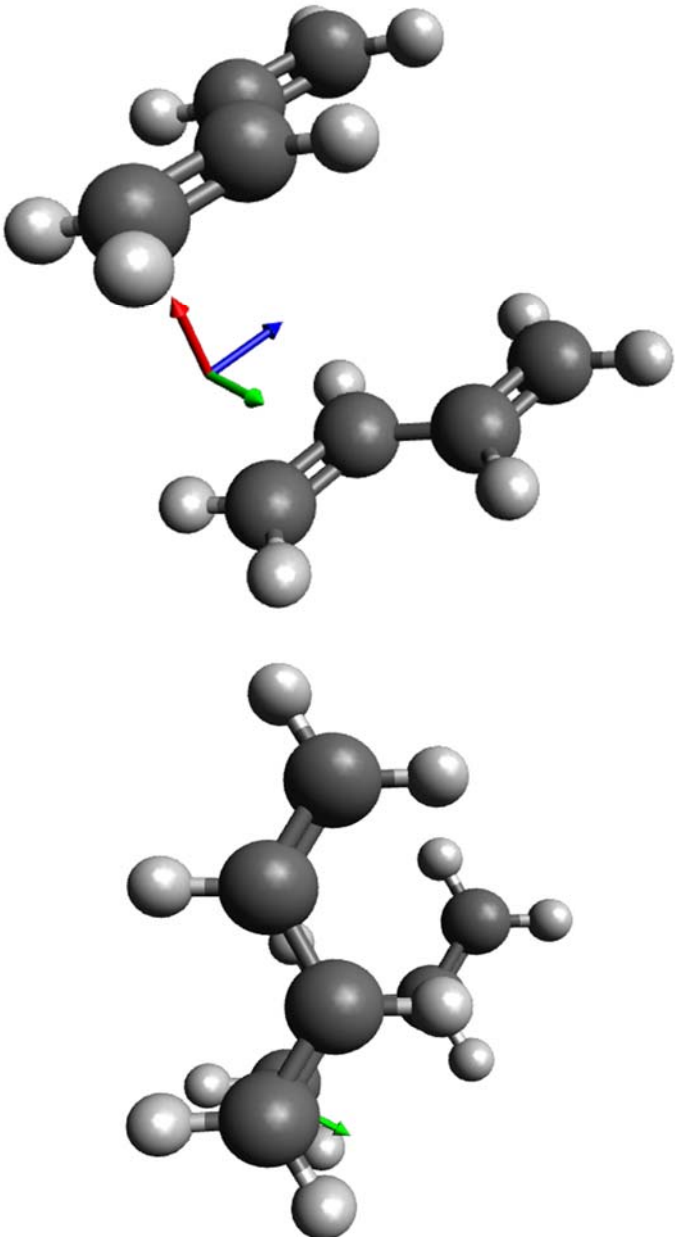

Figure 3.1. 1,3-butadiene dimer used in quantum simulations, arranged so that the z-axis is the primary axis of rotation. The z-axis is blue, the x-axis is red, and the y-axis is green. The monomers are stacked on top of each other to form a 'Y' shape as can be seen from the top-down view of the second image. The distance between the monomers is 3.8 Å, which matches the π-stacking distance between the aromatic rings in the crystal structure used in the companion paper.

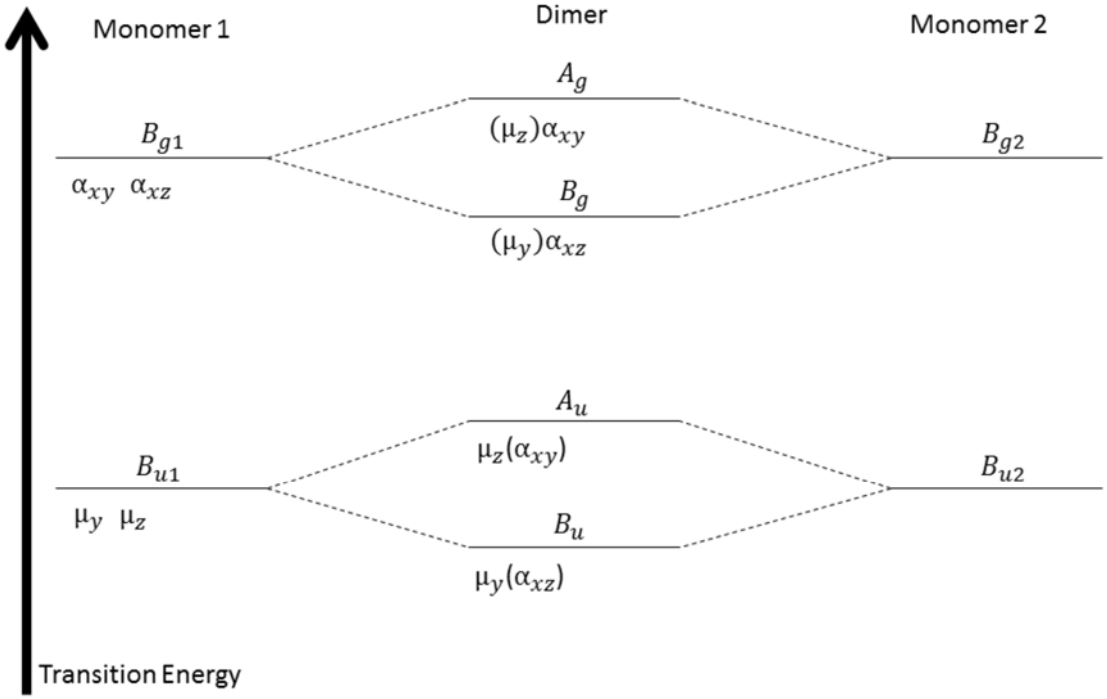

Figure 3.2. Exciton coupling diagram for 1,3-butadiene. Terms in parenthesis represent relatively small contributions from a different dimer transition. Such overlap in molecular orbitals is allowed due to similar symmetry.

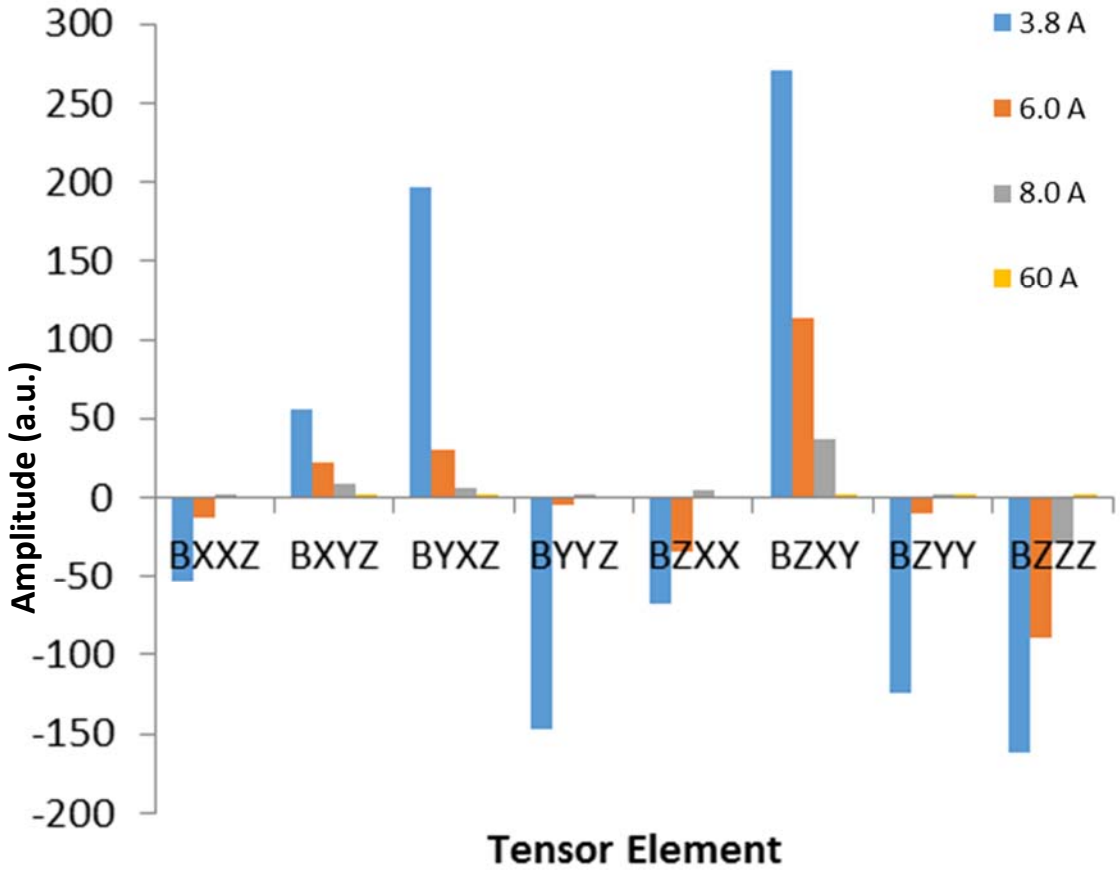

Figure 3.3. Calculated hyperpolarizability of 1,3-butadiene dimer at varying dimer distances. All calculations were performed at 450 nm.

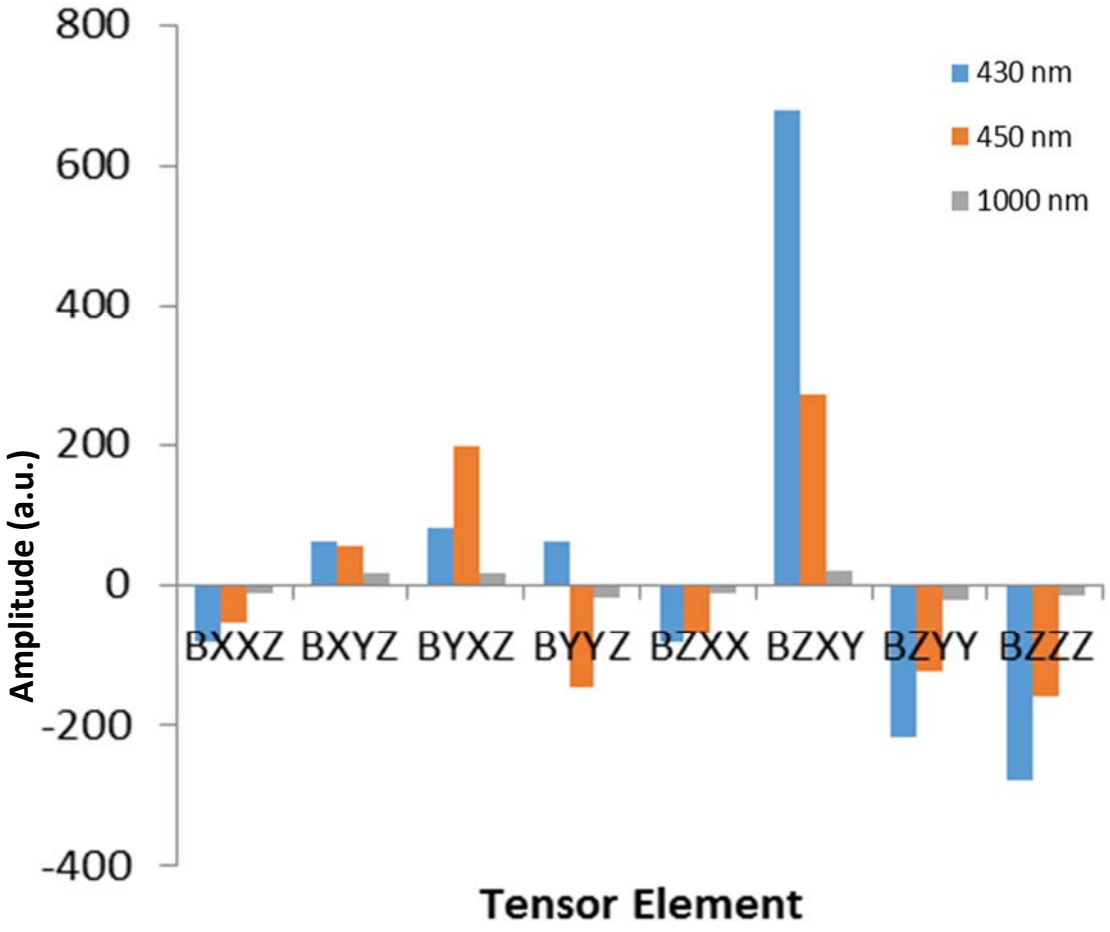

Figure 3.4. Calculated hyperpolarizability of the 1,3-butadiene dimer at different incident frequencies. All calculations were performed at a dimer separation of 3.8 Å.

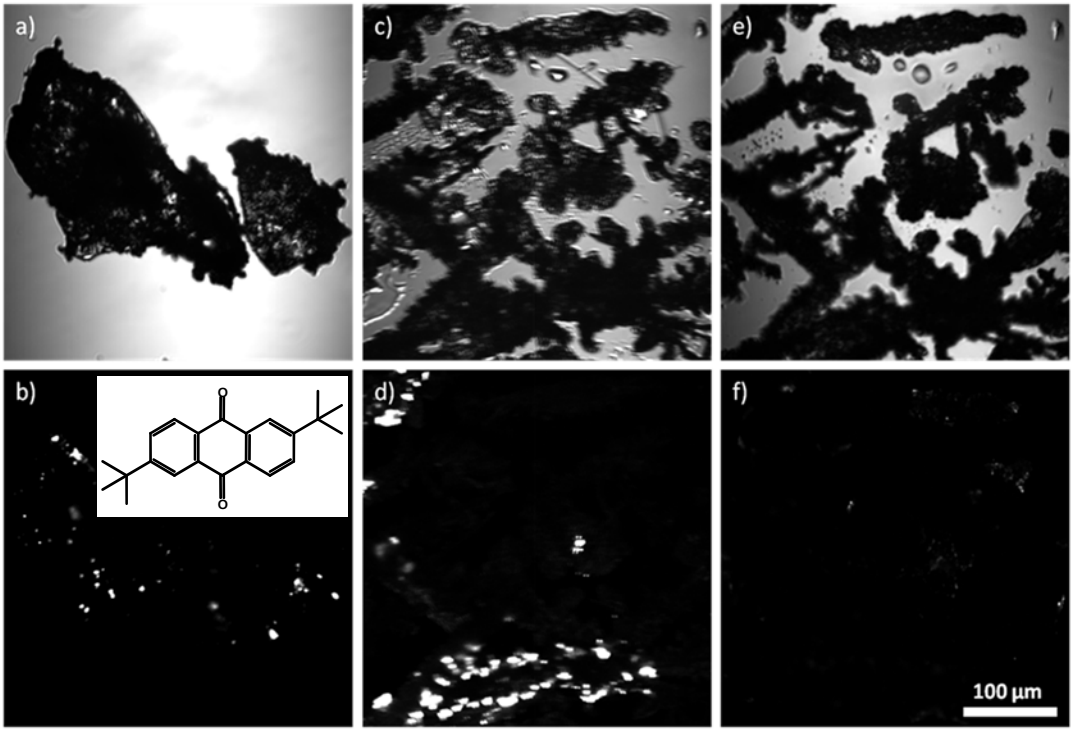

Figure 3.5. Laser transmitted images of TAQ from different crystallization conditions. Top row corresponds to the Laser transmittance images and bottom row corresponds to SHG images. The chemical structure of TAQ is also shown in 5b) in the inset. Figure a) and b) correspond to the powder as received, c) and d) correspond to the crystals grown by the solvent evaporation over the time course of a few minutes, e) and f) are the images of the same sample following enclosure in a chamber containing high solvent vapor pressure for three days. The SHG images are all presented using a common intensity scale relative to a $BaTiO_3$ nanoparticle reference.

Table 3.1: CIS calculations on 1,3-butadiene monomer and dimer at two distances. Each monomer transition gives rise, through addition and subtraction, to two dimer transitions.

	Monomer	**Dimer (8.0 A)**	**Dimer (3.8 A)**
1st excited state	Energy: 198.2 nm μ_x = 0 Debye μ_y = -1.37 Debye μ_z = 6.47 Debye Symmetry: Bu	Energy: 199.8 nm μ_x =0.01 Debye μ_y = -1.92 Debye μ_z = 0 Debye Symmetry: B	Energy: 211.1 nm μ_x = -0.02 Debye μ_y = 1.76 Debye μ_z = 0 Debye Symmetry: B
		Energy: 196.9 nm μ_x = 0 Debye μ_y = 0 Debye μ_z = 9.04 Debye Symmetry: A	Energy: 193.8 nm μ_x = 0 Debye μ_y = 0 Debye μ_z = -6.90 Debye Symmetry: A
2nd excited state	Energy: 190.9 nm μ_x = 0 Debye μ_y = 0 Debye μ_z = 0 Debye Symmetry: Bg	Energy: 191.4 nm μ_x = 0 Debye μ_y = -0.09 Debye μ_z = 0 Debye Symmetry: B	Energy: 193.2 nm μ_x = 0.11 Debye μ_y = -0.26 Debye μ_z = 0 Debye Symmetry: B
		Energy: 191.3 nm μ_x = 0 Debye μ_y = 0 Debye μ_z = -0.21 Debye Symmetry: A	Energy: 187.9 nm μ_x = 0 Debye μ_y = 0 Debye μ_z = 3.77 Debye Symmetry: A
3rd excited state	Energy: 181.0 nm μ_x = 0.79 Debye μ_y = 0 Debye μ_z = 0 Debye Symmetry: Au	Energy: 181.1 nm μ_x = 0 Debye μ_y = 0 Debye μ_z = -0.01 Debye Symmetry: A	Energy: 182.8 nm μ_x = 0 Debye μ_y = 0 Debye μ_z = 3.72 Debye Symmetry: A
		Energy: 181.1 nm μ_x = 1.18 Debye μ_y = 0 Debye μ_z = 0 Debye Symmetry: B	Energy: 182.2 nm μ_x = -2.21 Debye μ_y =0 Debye μ_z = 0 Debye Symmetry: B

CHAPTER 4. SENSITIVE DETECTION OF POLYMORPH TRANSITIONING IN CLOPIDOGREL BISULPHATE BY SECOND HARMONIC GENERATION MICROSCOPY WITH RAMAN SPECTROSCOPY

4.1 Introduction

Polymorphism and polymorph transitioning are equally crucial for active pharmaceutical ingredients (APIs) formulation from the early stage of drug development to the shelf life of a final product. Polymorphism is referred to the existence of multiple crystalline solid forms of the same compound and this multiplicity arises from the packing and/or the relative orientation of molecules in the crystal lattice. These differences in crystal lattice of an API exhibit different bioavailability by differing their physicochemical properties such as dissolution kinetics, thermodynamic stability, etc.[1-4] In most cases, thermodynamically most stable polymorph is the preferred choice for the solid dose development to avoid polymorphic phase transition in the final dosage. However, selection of an inadequately characterized polymorph may cause a severe problem to the pharmaceutical industries as well as to the consumers from a polymorphic phase transitioning during the development and/or in the final dosage. A classic example is the ritonavir, in which the marketed final dosage form spontaneously converted to a more stable and previously unknown crystal form, which exhibited substantially slower dissolution kinetics and correspondingly lower bioavailability.[5] A recent study estimates that more than 80% of APIs have multiple known polymorphic forms and therefore, food

and drug administration (FDA) and other government agencies require an appropriate characterization of APIs during filing for a new drug applications (NDAs) and abbreviated new drug applications (ANDAs).[2,6,7] Considering the list of potential drug candidates and their emergence to the market, a high-throughput (HT) analytical method for APIs screening is essential from the early stage of drug development to the shelf life of final dosages.

Clopidogel bisulphate is a particularly interesting example, in which seven different polymorphic form have been identified; among them only form I and form II are used for the drug formulation.[8-10] For both polymorphs Form I and Form II, only dextrorotatory enantiomer exhibits anti-platelet aggregation where the levorotatory enantiomer remains inactive,[11] and therefore the final dosage form is a pure enantiomeric form preparation. After the discovery of the form II, it was found that the higher bioavailability polymorph Form I was a metastable form and Form II is thermodynamically more stable.[9] Solvent mediated crystallization is the most common method for the production of these polymorphs where Form I transformed from amorphous phase and the form II transformed from form I. Both polymorphic forms of clopidogrel bisulphate possess an enantiotropic system where two different polymorphs are stable in different temperature, thus Form I has the potential to spontaneously transition to the more stable Form II during manufacture and storage.[10,12] Therefore, methods capable of sensitively identifying the early onset of the Form I to Form II transition could be used for active control to ensure Form I production during synthesis. Even a small mass fraction of the more stable polymorph may have profound impacts on subsequent stability of the final dosage form. Furthermore, a poorly

soluble crystalline fraction may negatively impact the dissolution kinetics by serving as nuclei for precipitation of the API upon introduction to the gut.[13]

Several analytical methods have been explored for clopidogrel polymorphic form characterization and quantification including X-ray diffraction analysis[14], vibrational spectroscopic technique combined with chemometrics[10], solid state stress degradation studies[15], X-ray microtomography[16]. In X-ray diffraction analysis, Uvarov and Popov have quantified the clopidogreal phase content in the mixture of Form I and Form II using X-ray powder pattern decomposition and classical direct methods. The limit of detection was found to be 1.0-1.5 wt.% in both methods.[14] In another quantitative analysis of clopidogrel bisulphate form II in Form I, Nemet and coworkers combined IR and Raman spectroscopy with chemometrics and quantified 2% and 3% of Form II in Form I, respectively, with less than 1% limit of detection.[10] Recently, a microscopy based approach combined with image-analysis was developed to extract morphological details for quantification of trace amount of polymorphic phases by morphology. In this study, a synchrotron radiation X-ray computed microtomography (SR μCT) was used for selective and sensitive detection of clopidogrel bisulphate polymorphs. The limit of detection (LOD) was also found to be 1%.[16] Although, this microscopy based approach shows a good promise in polymorphic phase determination in terms of required time to the sample a large area (2048 x 2048 pixels in 2 sec., pixel size = 3.7 μm), it is not suitable for online phase monitoring due to the requirement of a synchrotron radiation source. Although, these reported techniques are capable of detecting polymorphic phases down to ~1% LOD, none of these technique possess enough sensitivity to reach the detection limit into the parts per million (ppm) regime relevant to stability and dissolution kinetics.

Recent studies have suggested the use of nonlinear optical imaging for quantifying both overall crystalline content and crystal polymorphism in pharmaceutical formulations. have shown the capabilities of nonlinear optical imaging to detect organic nanocrystal[17], quantify second order nonlinear optical signal from various active pharmaceutical ingredients[18,19],vizualize protein crystal domain[20], detect and characterize metastable polymorphs[21,22], discriminate polymorphs rapidly[23], detect crystallinity in ppm regime[24], quantify second order nonlinear optical signal per particle basis in powder matrix[25]. While previous studies suggest nonlinear optical methods can be used for discrimination of crystal forms in model systems with well-defined polymorphs, definitive confirmation has not yet been demonstrated through independent analyses on pharmaceutically relevant materials.

In this work, we propose the use of Raman and synchrotron PXRD guided by SHG microscopy for crystal form characterization of individual ~100 ng particles of clopidogrel bisulfate. Specifically, the combination of bright field imaging and SHG microscopy was used to identify candidate particles for subsequent Raman and PXRD analysis of crystal form. Measurements are presented for physical mixtures of Form I and Form II particles, prepared similarly with the exception of the reaction time; the reaction time was extended for the Form II production to allow complete transitioning.

4.2 Experimental

4.2.1 Material and Sample Prep

Pure clopidogrel bisulphate Form I and Form II were produced in-house at Dr. Reddy's lab in India. Clopidogrel bisulphate is a drug that falls into thienopyridine class. It inhibits the platelet aggregation and used to treat patients with acute coronary syndrome. As produced, both polymorphic forms were generated as white spherical particles, exhibiting a similar size distribution with a diameter of ~25 μm. Particle diameter was determined by bright field image analysis. The conversion between pixels and micrometers was calibrated using an Air Force test grid. Three different samples were prepared as powdered blends consisting of clopidogrel bisulphate Form I with trace quantities of Form II (1%, 0.1% and 0.01% by mass). Images were taken for powders compacted between two glass microscope slides from at least three arbitrarily chosen location of each sample to provide representative sampling.

4.2.2 SHG Imaging

SHG micrographs were obtained using a commercial Formulatrix SONICC system, modified in-house for compatibility with powder analysis. In brief, a Fianium femtosecond laser was used as the incident source (170 fs, 1.3 W, 1060 nm, 51 MHz repetition rate). SHG images were produced by beam-scanning through a 10x objective with a ~1mm × 1mm field of view with the SHG measured in transmission. Unless otherwise indicated, 150 mW laser power measured at the sample and 1s acquisition time was used for SHG imaging. Bright field images acquired with a white-light source and a camera in the same

instrument were used to identify particle locations by segmentation algorithms described in detail in a subsequent section.

4.2.3 SHG Guided Raman Measurement

A prototype built-in-house microscope was used to acquire Raman spectrum from SHG active and inactive particles in each field of view. In this prototype instrument output of a Toptica continuous wave (CW) laser (785nm wavelength) was collected by an optical fiber of a custom-made Raman probe (InPhotonics, RPS785/24), shown in Figure 4.1, and re-collimated by a ½" fused silica lens. Collimated light then taken through a scan head followed by two other fused silica 1" lenses in a 4f configuration to focus on the sample using a 10x objective. A galvanometer mirror pair was used in the scan head and precise voltage controlling on two galvanometer mirrors drives the Raman beam to a randomly chosen location in each field of view. Using of two galvanometer mirrors was advantageous in a way that it also could be used to scan the sample for spectral imaging. Raman signal from the sample was collected in epi, following the same beam path back through the same Raman probe and directed into an Action SP-300i spectrometer to generate spectrum. There was a built-in notch filter in the probe to block the laser line. A 100x1340 array based CCD chip was used inside of the spectrometer to generate spectrum. Vendor software Winspec32 was used to collect spectra. Two different computers were used in this prototype instrument, one to drive the beam and the other to collect the spectrum.

4.2.4 X-ray Diffraction Measurement

X-ray diffraction (XRD) measurement was carried out by a SHG integrated XRD multimodal microscope in Argonne National Laboratory, Chicago. Instrument details was described elsewhere[26,27]. In short, a Fianium FemtoPower ~1060 ultrafast fiber laser that generates ~160 fs pulses centered at 1064nm, with a 50 MHz repetition rate was integrated into GM/CA@ APS beamline 23-ID-B at the Advanced Photon Source. Output of the laser was used to scan the sample through a 10x objective with a numerical aperture (NA) of 0.3 using a resonant-galvo scan-head. SHG and beam blocking laser transmitted signal was collected in trans and images were created by registering the photon events synchronizing with the laser pulses. The unattenuated photon flux of 12 keV, 5 μm diameter beam was used to generate diffraction pattern.

4.2.5 Image Segmentation and Registration

The image segmentation algorithm was developed in Matlab where a normalized cross correlation (NCC) based template matching algorithm was trained by images of an Airforce test grid taken by two different modalities, Bright field and SHG, to recover the pattern in both images and align them to each-other. In the following step, an efficient Otsu's adaptive thresholding was used on SHG image to create a binary mask (Figure 4.4d), assuming two polymorphs are present and thus a bimodal intensity distribution in intensity is expected. Otsu's method separates image into two classes, i.e. background and foreground, it starts with an arbitrary threshold then searches for an optimal threshold that maximizes the inter-class variance.[28] At the same time a binary image was also created (Figure 4.4c) using the bright field image followed by removal of residual pixels to match

the SHG image dimensions. At this point a simple subtraction followed by pruning the residual mask recover the particles that produces low or almost no SHG signals (Figure 4.4f), consequently, the Form II. Although, this advanced image processing algorithm can recover the Form II in Form I easily, further validation of this polymorphic phase determination is obligatory.

4.3 Results

4.3.1 Pure Sample Measurement

SHG images were obtained from the pure Form I and Form II using the commercial Formulatrix instrument, the results are presented in Figure 4.2. Form I exhibits ~250 times higher SHG activity per unit volume than the Form II. In both cases, SHG intensity measurement from each individual particle was calculated to estimate the SHG per unit volume (SHG/V) and normalized to the reference material of $BaTiO_3$ (500 nm). Clopidogrel bisulphate Form I is known to adopt a monoclinic unit cell and belongs to the $P2_1$ space group, and Form II has an orthorhombic unit cell and belongs to $P2_12_12_1$ space group.[14] Symmetry properties within the molecule as well as in the crystal lattice play a significant role in dictating SHG activity. Detectable coherent SHG signal is produced selectively from the bulk crystalline fraction and only within crystals of appropriate symmetry. In this context, higher or lower symmetry in the crystal lattice resulted in dimmer or brighter SHG signal per unit particle volume, respectively.

The integrated intensity over multiple z-planes (Figure 4.3) totaling a depth of field ~120 μm was divided by the estimated volume of an individual particle multiplied

with the total number of the particles in the field of view to determine the SHG activity per unit volume. Bright outliers (greater than 3σ) in the SHG image of Form II (Figure 4.2.d) were excluded in the calculation. Diameter of Particles were calculated from the bright field measurement and SHG activity per particle were recovered using the segmentation algorithm. The combined mean and standard deviation in the SHG activities on per particle basis were 13±2. counts/particle for Form I and 0.046±0.006 for Form II. Based on these measurements, individual particles can be assigned to either Form I or Form II with a statistical confidence of 99.995%.

4.3.2 Form I and Form II Mixture

In order to quantify polymorphic phase content in a mixture, bright field and SHG images were taken of a 10% mixture of Form II in Form I. The combination of bright-field and SHG micrographs provided a means to make initial classifications of individual particles as either Form I or Form II, the process of which is illustrated in Figure 4.4. Bright field images enabled identification of particle locations with a high signal to noise ratio (SNR), while the difference in SHG/V for Forms I and II was used for initial classification. However, the bright field and SHG images were acquired using independent beam paths, the former of which was obtained using a camera with wide-field illumination, while the latter was generated by beam-scanning. As such, image registration algorithms were developed and employed to correct for the disparities in the number of pixels and in the fields of view for the two imaging modalities. The assumption of spheroidal particle morphologies (~25 μm in diameter) reduced complications from particle-particle overlap in the segmentation algorithm.

4.3.3 Raman Spectroscopy for Crystal Form Discrimination

An independent assessment of crystal form was performed by Raman spectroscopy using the SHG/V analysis to guide selection of relevant particles of interest, the results of which are presented in Figure 4.5. Figure 4.5a) and 4.5b) correspond to the post-processed bright field image and SHG image, respectively. The combination of these two images provides an initial assessment of crystal form, which can be subsequently tested by Raman spectroscopy. Representative Form II candidates are indicated by the red (SHG activity, low) and Form I candidates by blue (SHG activity, high) circles in both images. In order to acquire a Raman spectrum from each particle, the appropriate position of the Raman acquisition was selected by a galvanometer mirror pair, and Raman scattering from the targeted particles was integrated for ~1 minute (2 seconds per frame for 30 frames) to generate high SNR spectra. An excellent agreement was observed between the Form II reference spectrum and the Raman spectrum of individual ~100 ng particles classified as Form II based on the combined bright-field and SHG/V assessments. Similarly, definitive agreement was also observed for the Form I reference spectra with those obtained from particles classified as Form I in 10% mixture sample.

4.3.4 X-ray Diffraction for Further Validation

In addition to the Raman measurements, SHG guided synchrotron XRD measurements were also performed (Figure 4.6) for the 10% mixture to assess the capabilities of single-particle assessments of crystal form by SHG-guided Raman. Figure 4.6a) is the laser transmittance image of the 10% mixture, yellow circles in this image indicate the Form I and Form II identified by the SHG/V measurement. A collimated X-

ray beam, 5 μm in diameter, was used to raster the particle (shown in the inset of Figure 4.5b) and 4.5d)) in a 4x4 grid. Micro X-ray beam enhances the sensitivity of the measurement from localized sampling. Measurement took 2 s per location and another 2 s for dead time between next exposure. Diffraction images from each raster grid were combined to make a single diffraction image. Combination of diffraction images interrogate a broader window of particle's crystallographic orientation distribution thus suitable for statistical average, assuming the particles orientation were completely random. An integration of intensities along the azimuthal angle of a diffraction image recovers the anticipated powder X-ray diffraction (PXRD) pattern. Experimental diffraction patterns were also compared to the theoretical predictions of monoclinic and orthorhombic unit cell, obtained from Cambridge Structural Database (CSD) for Form I and Form II, respectively. Experimental observation of diffraction angles nicely complement the anticipated diffraction angles both polymorphs which definitively corroborates the classification by SHG-guided Raman.

Combining the segmentation with SHG measurements allows identification of particles of interest based on the differences in the SHG/V. From the results in Figure 4.2 and Figure 4.3, significant differences are expected for the Form I and Form II polymorphs. Statistical analysis of the integrated SHG activity per particle basis of both forms suggests a discriminatory confidence of 99.995% based on SHG alone. However, these results are only valid if the dominant differences are definitively connected directly to polymorphism, rather than other physical differences within the particles (e.g., crystal size distribution, orientation, degree of crystalline order, etc.).

4.4 Discussion

All three approaches (SHG, Raman, PXRD) provided excellent discriminatory capabilities for crystal form characterization. In the case of SHG, >99.99% confidence was achieved on a per-particle basis through the combination bright field for particle localization and average SHG for crystal form determination. Qualitatively similar trends were clearly observed by both Raman and XRD. While SHG enables this discrimination from a single scalar input (SHG per unit volume), both the Raman and XRD carry additional structural information through the recovered spectra (1D) and scattering patterns (2D). However, the greatest discrimination capabilities result from dimension reduction to a single scalar value to optimally inform crystal form, such that the measurement objectives are ultimately based on qualitatively similar inputs.

While all three methods allowed high degrees of crystal form discrimination, SHG microscopy has clear benefits in terms of simplicity and measurement time. In practice, conventional Raman required >1minute of signal acquisition per particle to obtain spectra with sufficient SNR for highly confident crystal form discrimination, since the spontaneous Raman event is relatively inefficient (1 in 10^7 Raman scattering events relative to Rayleigh scattering).[29] For a spectral acquisition time of 60 s, a mixture of 1% Form II would take ~15 hours of continuous signal acquisition from 900 individual particles followed by post processing of these spectra to quantify polymorphic phase content (assuming no dead time and detection of 9 Form II particles for an SNR=3 from Poisson statistics). The timeframe for synchrotron analysis is considerably reduced, with as little as 1s integration time per particle, corresponding to ~30 minutes of acquisition (assuming 1 second dead time for data transfer and sample repositioning). However, synchrotron time is also considerably

more difficult to routinely access, given the high demands on beam-time and limited number of synchrotron facilities. In contrast, SHG imaging allowed characterization of all particles within a 1x1 mm^2 area with one second of data acquisition. For an average of ~200 particles in a given field of view, the timeframe required to probe 900 particles is still only a few seconds. To achieve limits of detection of 0.1% would require ~1 minutes (40 frames with ~0.5 s dead time for sample repositioning between frames), and 100 ppm ~10 minutes.

The relatively low variance in the SHG intensity per particle basis are consistent with the presence of numerous small crystallites within each spheroidal particle. The relative standard deviation (RSD) in the SHG/V determination for both Forms I and II was ~15% (calculated from more than 100 particles taken from different fields of view, yielding 13±2 counts/particle for Form I and 0.041±0.006 for Form II). The low relative RSD observed in this study contrasts significantly from SHG microscopy measurements in powders, in which the RSD approached unity for a uniformly distributed population of $BaTiO_3$ nanoparticles.[25] The low per particle RSD is consistent individual particles comprised of polycrystalline conglomerate, rather than single crystals. For a polycrystalline conglomerate, a representative population of numerous small crystallites contributes to the overall SHG intensity observed, rather than a few relatively large sources. In the limit of the average crystal size being much less than the focal volume, a statistical population of all sizes and orientation are reasonably sampled within each individual particle, greatly reducing the particle-to-particle variance in SHG intensity.

It is important to note that the discrimination describe by all methods in this work implicitly assumes that individual particles will be present as either Form I or Form II,

rather than a mixtures containing both forms in each particle. In practice, it is well established that the kinetics of phase transformation are significantly faster for intra-particle interactions[30,31], in which adjacent crystallites are in intimate contact and can serve to nucleate Form II conversion, relative to inter-particle interactions involving minimal and transient crystal contact. As such, kinetically it is reasonable to assume that any initial nucleation event in a given particle results in rapid transition throughout the extent of the particle, but slow (if any) propagation to adjacent particles, consistent with the expectations of the analysis.

4.5 Conclusions

In this study, a prototype instrument (SHG microscopy guided Raman spectroscopy and powder X-ray diffraction) was used to confirm the rapidly identified trace polymorphic form of clopidogrel bisulfate Form II in Form I by SHG measurement. Measurement validations are presented for physical mixtures of Form I and Form II particles. The combination of bright field imaging and SHG microscopy was used to identify candidate particles for subsequent Raman and PXRD analysis of crystal form. Both the SHG guided Raman and synchrotron PXRD results support the initial tentative assignments of crystal form by SHG. Nevertheless, additional benefits of combining methods for orthogonal determination, SHG guiding provides a huge time-saving and enhanced sensitivity by excluding particles that are unlikely to be Form II based on the presence of bright SHG. At the same time, quantification of polymorphic phase content becomes very straight forward by rejecting the requirement of a calibration plot that is required for any other quantitative analytical method. This study potentially can improve overall yield and polymorphic

purity during synthesis and crystallization of clopidogrel bisulfate Form I by identifying Form II during batch drug product crystallization in real time.

4.6 References

1 Aaltonen, J. *et al.* Solid form screening–a review. *European Journal of Pharmaceutics and Biopharmaceutics* **71**, 23-37 (2009).

2 Chieng, N., Rades, T. & Aaltonen, J. An overview of recent studies on the analysis of pharmaceutical polymorphs. *J Pharm Biomed Anal* **55**, 618-644, doi:10.1016/j.jpba.2010.12.020 (2011).

3 Singhal, D. & Curatolo, W. Drug polymorphism and dosage form design: a practical perspective. *Adv Drug Deliv Rev* **56**, 335-347, doi:10.1016/j.addr.2003.10.008 (2004).

4 Snider, D. A., Addicks, W. & Owens, W. Polymorphism in generic drug product development. *Adv Drug Deliv Rev* **56**, 391-395, doi:10.1016/j.addr.2003.10.010 (2004).

5 Bauer, J. *et al.* Ritonavir: an extraordinary example of conformational polymorphism. *Pharmaceutical research* **18**, 859--866 (2001).

6 Raw, A. Pharmaceutical solid polymorphism in drug development and regulation. *Advanced Drug Delivery Reviews* **56**, 235-236, doi:10.1016/j.addr.2003.10.004 (2004).

7 Raw, A. S. *et al.* Regulatory considerations of pharmaceutical solid polymorphism in Abbreviated New Drug Applications (ANDAs). *Adv Drug Deliv Rev* **56**, 397-414, doi:10.1016/j.addr.2003.10.011 (2004).

8 Bousquet, A., Castro, B. & Saint-Germain, J. (Google Patents, 2003).

9 Lu, J., Wang, J. & Rohani, S. Preparation and characterization of amorphous, I and II forms of clopidogrel hydrogen sulfate. *Crystal Research and Technology* **47**, 505-510, doi:10.1002/crat.201200037 (2012).

10 Nemet, Z., Demeter, A. & Pokol, G. Quantifying low levels of polymorphic impurity in clopidogrel bisulphate by vibrational spectroscopy and chemometrics. *J Pharm Biomed Anal* **49**, 32-41, doi:10.1016/j.jpba.2008.09.042 (2009).

11 Badorc, A. & Frehel, D. (EP Patent 281,459, 1988).

12 Koradia, V., Chawla, G. & Bansal, A. K. Qualitative and quantitative analysis of clopidogrel bisulfate polymorphs. *Acta pharmaceutica* **54**, 193-204 (2004).

13 Fahr, A. & Liu, X. Drug delivery strategies for poorly water-soluble drugs. *Expert opinion on drug delivery* **4**, 403-416 (2007).

14 Uvarov, V. & Popov, I. Development and metrological characterization of quantitative X-ray diffraction phase analysis for the mixtures of clopidogrel bisulphate polymorphs. *J Pharm Biomed Anal* **46**, 676-682, doi:10.1016/j.jpba.2007.11.026 (2008).

15 Raijada, D. K., Prasad, B., Paudel, A., Shah, R. P. & Singh, S. Characterization of degradation products of amorphous and polymorphic forms of clopidogrel bisulphate under solid state stress conditions. *J Pharm Biomed Anal* **52**, 332-344, doi:10.1016/j.jpba.2009.05.001 (2010).

16 Yin, X. Z. *et al.* In situ 3D topographic and shape analysis by synchrotron radiation X-ray microtomography for crystal form identification in polymorphic mixtures. *Sci Rep* **6**, 24763, doi:10.1038/srep24763 (2016).

17 Wanapun, D., Kestur, U. S., Kissick, D. J., Simpson, G. J. & Taylor, L. S. Selective detection and quantitation of organic molecule crystallization by second harmonic generation microscopy. *Analytical chemistry* **82**, 5425-5432 (2010).

18 Toth, S., Madden, J., Taylor, L., Marsac, P. & Simpson, G. Selective imaging of active pharmaceutical ingredients in powdered blends with common excipients utilizing two-photon excited ultraviolet-fluorescence and ultraviolet-second order nonlinear optical imaging of chiral crystals. *Analytical chemistry* **84**, 5869-5875 (2012).

19 Toth, S. J. *et al.* Ab Initio Prediction of the Diversity of Second Harmonic Generation from Pharmaceutically Relevant Materials. *Crystal Growth & Design* **15**, 581-586 (2015).

20 DeWalt, E. L. *et al.* Polarization-resolved second-harmonic generation microscopy as a method to visualize protein-crystal domains. *Acta Crystallographica Section D: Biological Crystallography* **69**, 74-81 (2013).

21 Chowdhury, A. U. *et al.* Kinetic trapping of metastable amino acid polymorphs. *Journal of the American Chemical Society* **136**, 2404-2412 (2014).

22 Hall, V. J. & Simpson, G. J. Direct observation of transient Ostwald crystallization ordering from racemic serine solutions. *Journal of the American Chemical Society* **132**, 13598-13599 (2010).

23 Schmitt, P. D., DeWalt, E. L., Dow, X. Y. & Simpson, G. J. Rapid Discrimination of Polymorphic Crystal Forms by Nonlinear Optical Stokes Ellipsometric Microscopy. *Analytical chemistry* (2016).

24 Newman, J. A. *et al.* Parts per million powder X-ray diffraction. *Analytical chemistry* **87**, 10950-10955 (2015).

25 Chowdhury, A. U., Zhang, S. & Simpson, G. J. Powders Analysis by Second Harmonic Generation Microscopy. *Analytical chemistry* **88**, 3853-3863 (2016).

26 Madden, J. T. ***et al.*** Integrated nonlinear optical imaging microscope for on-axis crystal detection and centering at a synchrotron beamline. *Journal of synchrotron radiation* **20**, 531-540 (2013).

27 Newman, J. A. ***et al.*** Guiding synchrotron X-ray diffraction by multimodal video-rate protein crystal imaging. *Journal of Synchrotron Radiation* **23** (2016).

28 Otsu, N. A threshold selection method from gray-level histograms. *Automatica* **11**, 23-27 (1975).

29 Harris, D. C. & Bertolucci, M. D. *Symmetry and spectroscopy: an introduction to vibrational and electronic spectroscopy*. (Courier Corporation, 1978).

30 Cardew, P. & Davey, R. in *Proceedings of the Royal Society of London A: Mathematical, Physical and Engineering Sciences.* 415-428 (The Royal Society).

31 Parrinello, M. & Rahman, A. Polymorphic transitions in single crystals: A new molecular dynamics method. *Journal of Applied physics* **52**, 7182-7190 (1981).

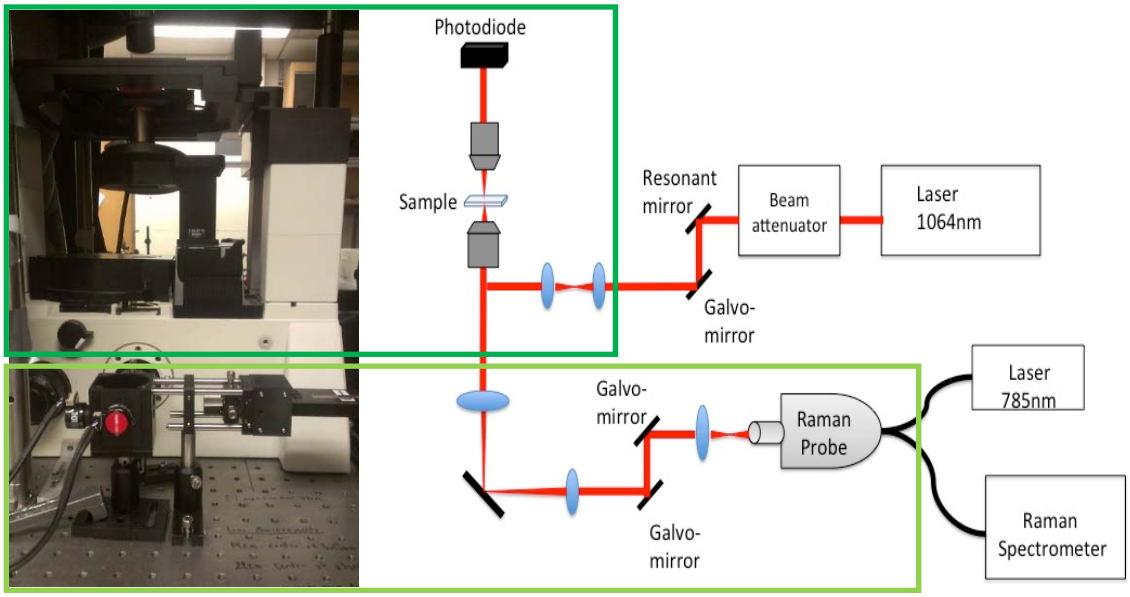

Figure 4.1. Raman spectroscopy integrated SHG microscope and its schematic diagram. The top box shows the SHG unit and the bottom rectangular box shows the Raman unit.

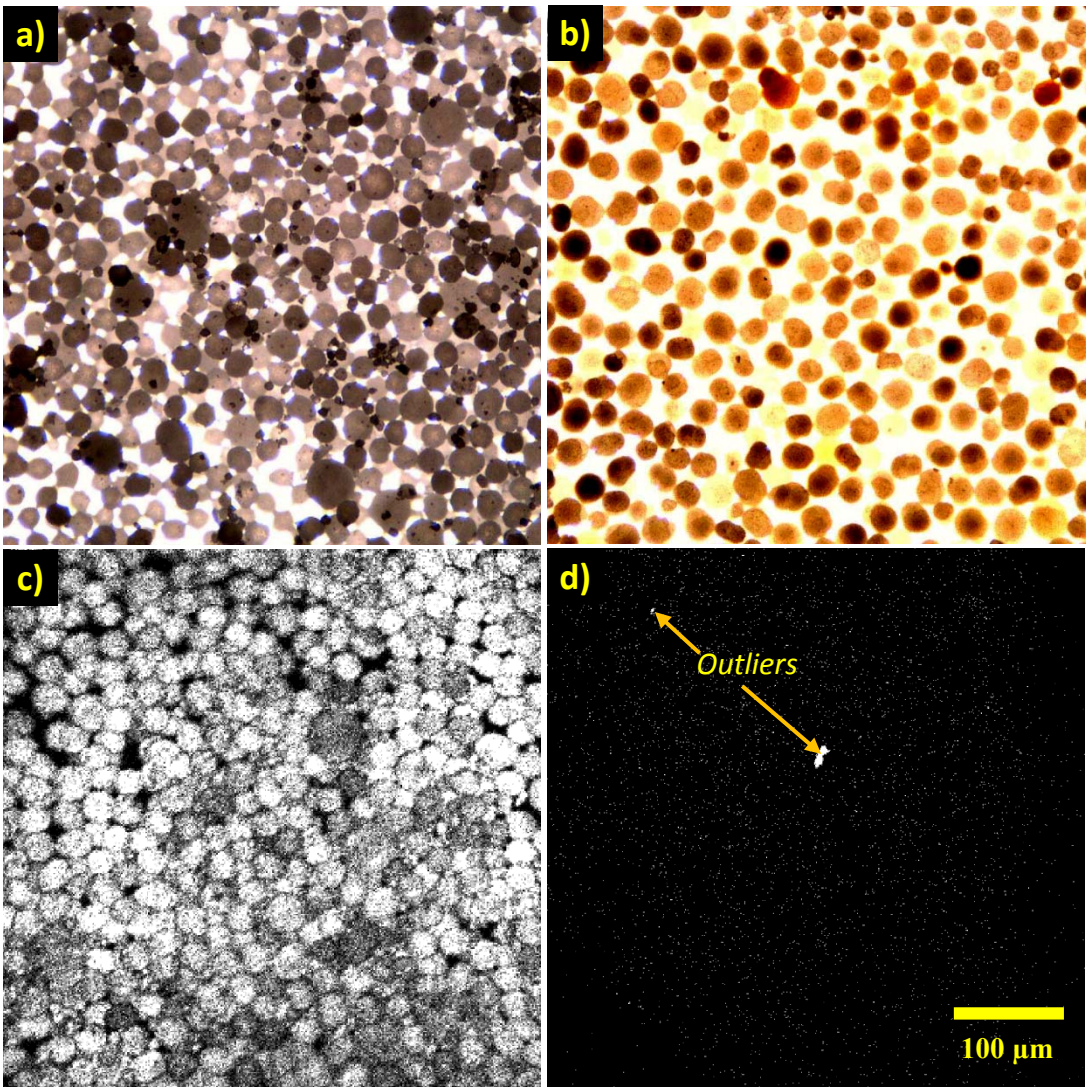

Figure 4.2: Pure sample measurement of Form I and Form II. Top row corresponds to bright field images and bottom row corresponds to SHG images of Form I and Form II, respectively. Bright outliers (greater than 3σ) in 4.2 d) were excluded from the analysis of the SHG activity / unit volume.

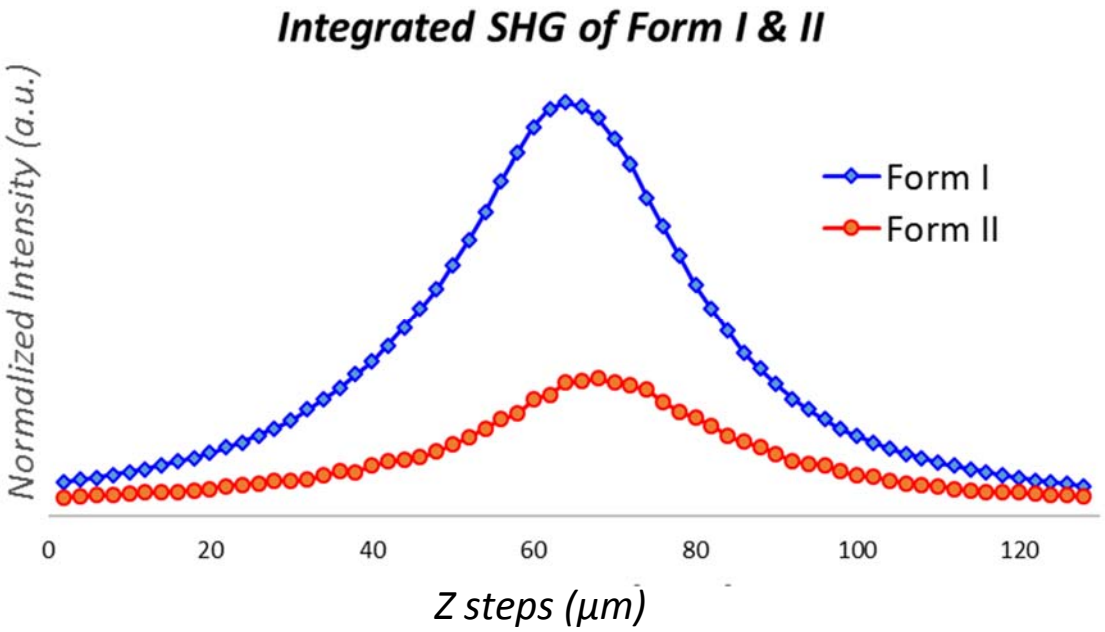

Figure 4.3: Integrated SHG along the Z-axis of Form I and Form II. Integrated SHG of Form II were rescaled by 100 folds. Outliers (bright SHG puncta in Form II) were excluded in this calculation.

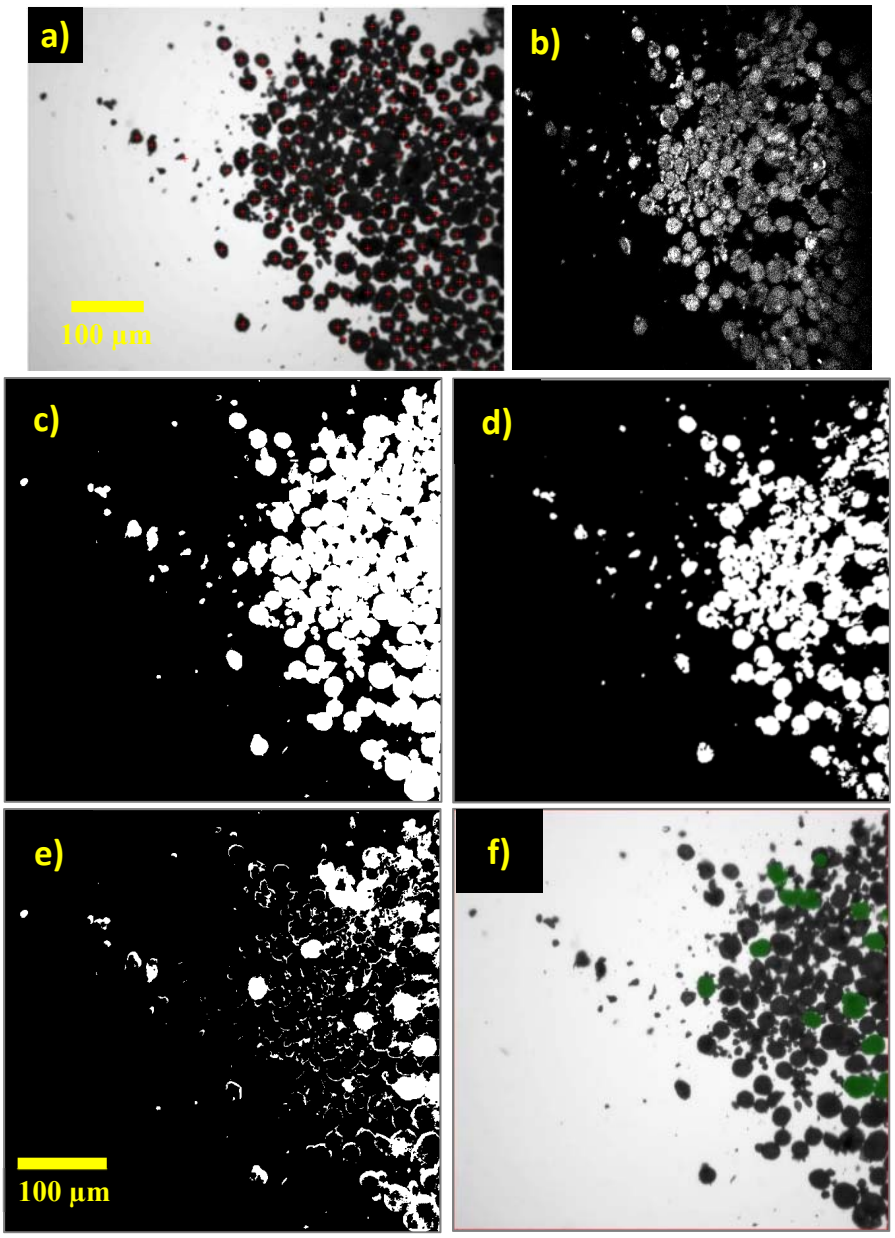

Figure 4.4: Representation of segmentation algorithm to recover the Form II particles. Brightfield (1a) and SHG (1b) images of a mixture of 10% clopidogrel bisulphate Form II to Form I. Red cross-hairs in the image indicate the representative candidates for the polymorphic form classification. Figure c) and d) correspond to the binary images created from the brightfield image and SHG image, respectively. Green circles in Figure f) indicate recovered particles of Form II.

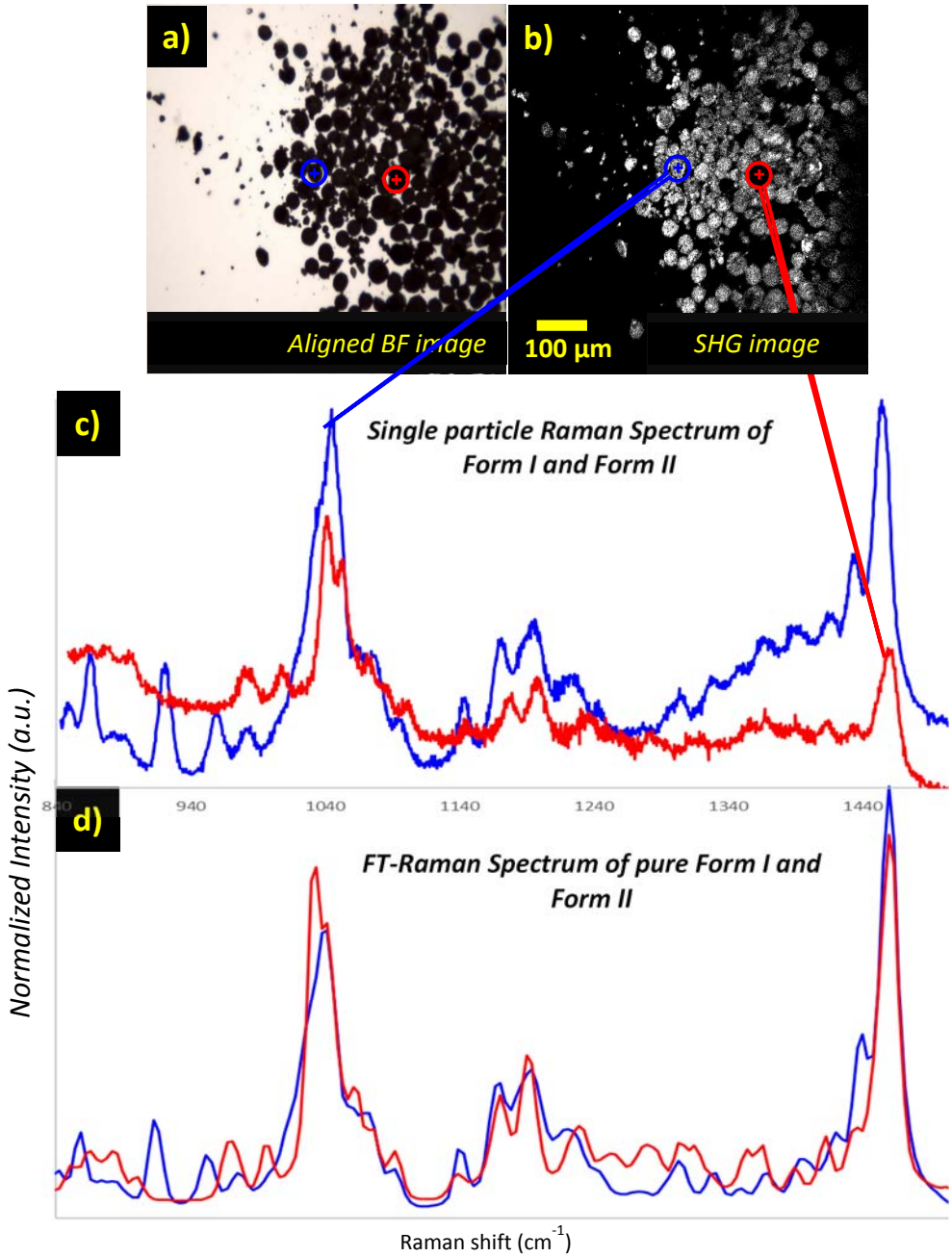

Figure 4.5: Crystal form classification confirmed by independent SHG-guided Raman analysis on a per-particle basis. Figure a) and b) correspond to brightfield and SHG image of a 10% mixture of Form II in Form I, respectively. Figure c) and d) correspond to single particle Raman spectrum and FT-Raman spectrum, respectively, of Form I and Form II. In both cases Raman spectrums confirm the classification made by SHG imaging.

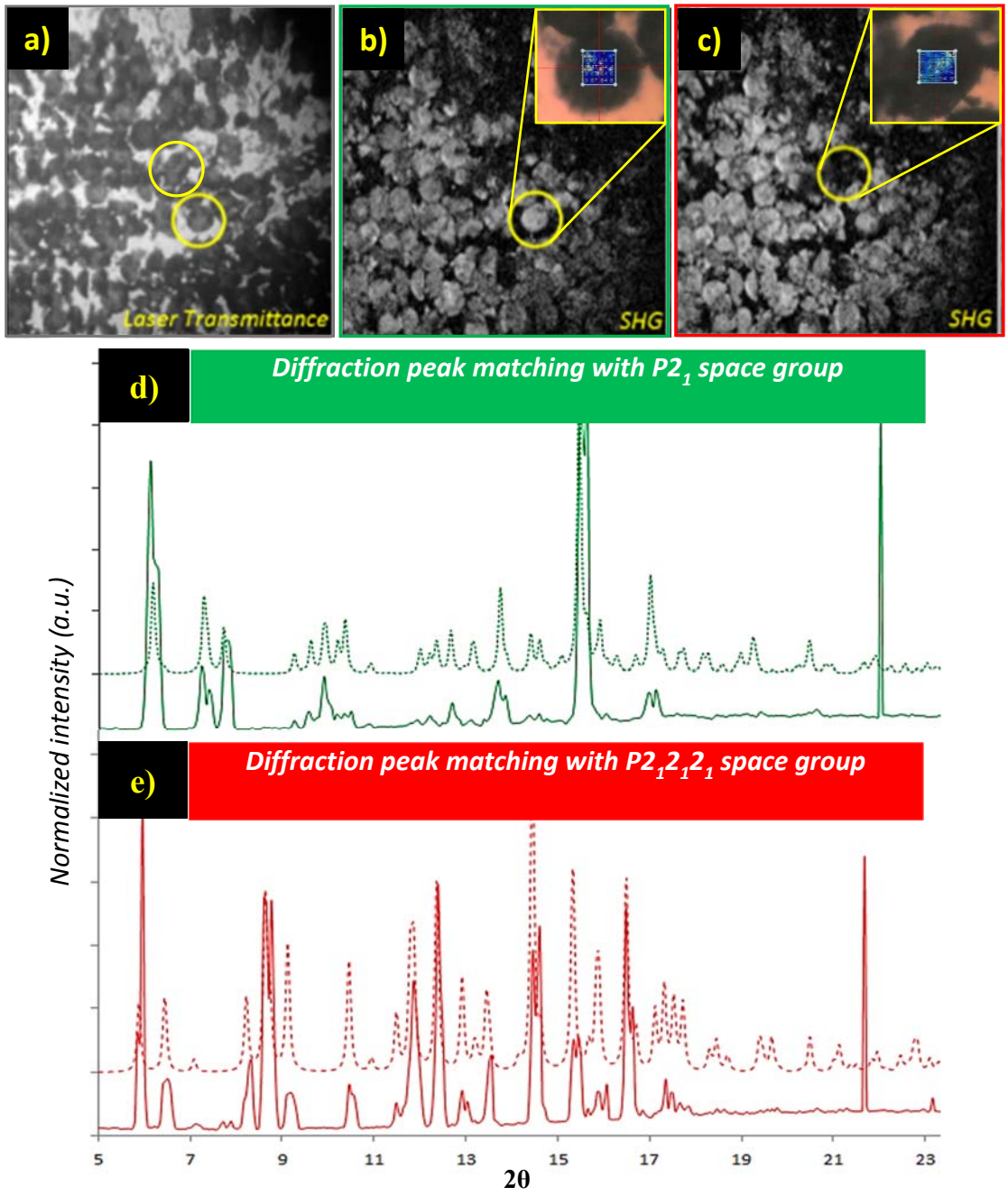

Figure 4.6. Initial classification by SHG/V measurement of 10% physical mixture of Form II in Form I, and validation by XRD measurement. Column 1 correspond to the bright field images of 1% mixture, and 2nd column correspond to the SHG images of the same FOV. Yellow circles indicate SHG high and SHG dim particles those are potential candidates for the diffraction measurements. Experimental diffraction patterns are compared to the theoretical prediction for Form I and Form II in figure 3e) and 3f) respectively.

CHAPTER 5. POWDER ANALYSIS BY SECOND HARMONIC GENERATION MICROSCOPY

5.1 Introduction

The SHG activity of powders is a common and important measurement, both historically for the characterization of efficiency in new nonlinear optical materials and more recently as an analytical tool for quantitative analysis of pharmaceutical materials. In the design of new materials for frequency conversion, powder second harmonic generation (PSHG) is routinely measured for preliminary assessments as it avoids the need to produce large single crystals. In pharmaceutical materials, Coquerel and coworkers used PSHG to observe structural phase transitions in powders,[1-3] identify SHG-active structural impurities,[3,4] and screen for the generation of homochiral conglomerates.[3,5] Measurement of the PSHG activity is also frequently reported as a powerful method for pharmaceutical crystal analysis, due to its low detection limit, fast response time, nondestructive nature, and low cost of automation.[1,6] The PSHG activity of active pharmaceutical ingredients (APIs) was shown to enable discrimination of polymorphism,[7-10] and quantify API crystallinity within mixtures.[7-9,11] Detection limits for trace API crystallinity within amorphous formulations in the parts per million regime have been reported.[6,12-14] Studies by Wanapun *et al*. yielded insights into the mechanism behind the milling-induced loss of crystallinity within API powders.[13] In studies by Berglund and coworkers, PSHG enabled

sensitive measurements of the induction times for crystallization from supersaturate solutions.[15] The sensitivity of SHG to polymorphism suggests the potential for expanded applications in routine crystal form screening of new APIs, which is routinely performed prior to development of final dosage forms. These practical applications appeal to the ever increasing demand in pharmaceutical industry for chiral crystal analysis, which boosts the development of enantioselective synthesis methods of pure enantiomer APIs.

Unfortunately, the large majority of these applications hinge on reliable quantitative analysis for reproducibly recovering SHG activities connected directly to lattice properties, and reproducible SHG signal quantification is often frustrated by the acquisition of SHG intensities that are also highly dependent on the crystal size distribution, the sample thickness, the presence or absence of phase-matching, and the packing density.[16-19] The most commonly accepted approach remains the Kurtz-Perry (KP) method in which the intensity of the transmitted and/or back-scattered SHG are recorded using a collimated fundamental source.[19] By repeating KP measurements using different particle sizes, it is possible to discriminate between phase matchable (PM) and non-phase matchable (NPM) materials from the SHG scaling with mean particle size. The presence of phase-matching, in which the refractive indices of the fundamental and doubled frequency are identical due to birefringence, can profoundly impact the net SHG intensity produced by a powder.[16-20] The influence of phase-matching is also generally highly size-dependent. As such, the inherent spread of crystal sizes present within a typical powder sample can be nontrivial to include in the modeling and data inversion.

Substantial improvements on the KP method have been suggested by several researchers. Aramburu *et. al*. have updated the KP method to include the effects of light

scattering in the analysis of the SHG process.[16] Kiguchi *et al.* have proposed a creative alternative approach, in which the powder measurements are performed using an evanescent wave in a total internal reflection configuration. In this manner, the interaction length with the fundamental beam in the powder is reduced to less than the wavelength of light, significantly reducing effects related to phase-matching.[20,21] Nevertheless, the limited number of observables present in ensemble-averaged experiments using collimated sources fundamentally complicates reproducible separation of the many competing contributions to the SHG intensity, and in turn the determination of the nonlinear susceptibility.

In this work, a microscopy-based analysis approach is described, which greatly increases the number of observables in powders analyses. The model includes consideration of the impact of the numerical aperture, optical scattering, packing density, crystal orientation, size, and phase-matching. Predictions of the model based on the focusing of a Gaussian beam are compared with experimental observables for both isolated nanoparticles and condensed powders.

5.2 Theoretical Foundation

In the present formulation, three separate effects can potentially limit the interaction length between the fundamental beam and a crystalline powder driving the production of SHG: i) the scattering length, ii) the forward coherence length, or iii) the depth of field. To treat scattering effects, a theoretical framework developed by Aramburu *et al.*,[16-18] which explicitly includes the role of optical scattering in the modeling, was modified for

compatibility with microscopy-based measurements. Using an equivalent spheres model, the scattering length l_s can be written in the following form.

$$l_s = \frac{1}{\rho \sigma_s} \tag{1}$$

In Equation (1), ρ is the density of scatterers and σ_s is the scattering cross section for each particle. In the limit of high refractive index mismatch (e.g., powder in air), the non-forward scattering cross-section $\sigma_{s,\text{"nonforward"}}$ becomes equivalent to the geometrical area of the particle, as both the scattered and transmitted portions of the beam will generally result in the loss of coherence. Assuming the refracted and scattered components are roughly equal in magnitude, the net scattering cross section σ_s is twice the non-forward cross section.

$$\sigma_{s,\text{"nonforward"}} \cong \pi R^2 \cong \tfrac{1}{2}\sigma_s \tag{2}$$

In Equation (2), R is the radius of an equivalent spherical scatter with a cross sectional area of πR^2. The decay length l_s can be expressed in terms of the fraction of occupied volume rather than the density by the substitution $f = \rho \frac{4}{3}\pi R^3$. Substitution into Equation (1) yields the following expression for l_s.

$$l_s \cong \frac{4\pi R^3}{3f}\frac{1}{2\pi R^2} = \frac{2R}{3f} \cong R \tag{3}$$

For a closed-packed assembly of equivalent spheres, the occupied volume approaches $f = 2/3$,[16] leading to the final approximation of $l_s \cong R$ in Equation (3).

5.2.1 Estimating the Effective Interaction Length Under Different Limiting Conditions

Three different interactions may ultimately dictate the effective interaction length over which SHG is coherently produced in a powdered sample: i) the depth of field l_d, ii) the coherence length l_c, or iii) the scattering length l_s. In this section, estimates for the effective volume contributing to the measured SHG intensity is provided for each limiting case.

i) Considering the simplest case first, the effective volume contributing to the detected SHG when the depth of field limits the interaction as illustrated in Figure 5.1a is simply given by the geometrical cross-sectional area of the particle multiplied by the depth of field l_d.

$$V_d = Al_d \tag{4}$$

ii) If the coherence length ultimately limits the interaction length as illustrated in Figure 5.1b, only the cross-sectional area of the particle within one coherence length will generally contribute to the detected SHG. The coherence length is by definition the length at which the fundamental and doubled frequencies are phase-shifted by π/2. At this length, the next incremental contribution to the SHG will transition from constructive to destructive interference. The effective volume evaluated by the coherence length is therefore slightly less than the geometrical length corresponding to traversing a distance of l_c through the medium by a net factor of π/2.

$$V_c = Al_c \frac{\int_0^{\pi/2} \cos z dz}{\int_0^{\pi/2} dz} = \tfrac{2}{\pi} Al_c \tag{5}$$

In Equation (5), the distance term z is the units of coherence length corresponds to the SHG produced by integration over an initial phase shift of zero and ending with a phase shift of π/2.

iii) If the scattering length limits the total interaction length as illustrated in Figure 5.1c, the depth of field is necessarily large relative to the particle radius, such that the effective volume V_s in the limit of spheroidal particles is given by the geometrical volume of an equivalent sphere with a cross-sectional area of A.

$$V_s = \tfrac{4}{3}\pi R^3 = \tfrac{4}{3} A l_s \tag{6}$$

In Equation (6), the approximation in Equation (3) for the effective particle radius R.

Since the scattering length l_s is relatively straightforward to measure experimentally from the ensemble-averaged Z-dependent integrated intensity, it is convenient as a reference point for identifying the conditions under which the appropriate expression for the effective volume should be used. The point at which the depth of field and the scattering length yield equivalent effective volumes corresponds to the following equality.

$$l_d = \tfrac{4}{3} l_s \tag{7}$$

Considering only these two contributions, the depth of field will dictate the interaction length when $l_d \leq \tfrac{4}{3} l_s$, and vice versa. A similar relationship can be established between l_s and l_c to identify the conditions under which the two effective volumes are equal.

$$l_c = \tfrac{2\pi}{3} l_s \tag{8}$$

5.2.2 Modeling Interactions in the Focal Volume

The optical model used is based on the paraxial approximation for a focused Gaussian beam, as described in Saleh and Teich,[22] and implicitly includes contributions from the forward coherence length and the depth of field. In brief, the amplitude and phase of the fundamental beam in the region neighboring the focal volume in the absence of scattering losses is given by the following expression.

$$E^{\omega}(z,\rho) = E_0^{\omega}\frac{W_0^{\omega}}{W^{\omega}(z)}\exp\left(\frac{-\rho^2}{W^{\omega}(z)}\right)\exp\left[-i\left(k_z^{\omega}z + k_z^{\omega}\frac{\rho^2}{2R^{\omega}(z)} - atan\left(\frac{z}{z_0}\right)\right)\right] \quad (9)$$

$$z_0^{\omega} = \frac{\lambda_0^{\omega}}{\pi\left(\theta_0^{\omega}\right)^2} \quad (10)$$

$$W_0^{\omega} = \sqrt{\frac{\lambda_0^{\omega} z_0^{\omega}}{\pi}} \quad (11)$$

$$W^{\omega}(z) = W_0^{\omega}\sqrt{1+\left(\frac{z}{z_0^{\omega}}\right)^2} \quad (12)$$

$$R^{\omega}(z) = z\left[1+\left(\frac{z_0^{\omega}}{z}\right)^2\right] \quad (13)$$

For the second harmonic beam generated in a copropagating direction, the following relations emerge.

$$E^{2\omega} = \left(\chi^{(2)} : E^{\omega}E^{\omega}\right) \quad (14)$$

$$\theta_0^{2\omega} = \tfrac{1}{\sqrt{2}}\theta_0^{\omega} \quad (15)$$

The reduction in the cone angle arises from squaring of the Gaussian beam profile as a consequence of the quadratic dependence of SHG on the incident intensity. This squaring results in a narrowing of the angular distribution.

$$z_0^{2\omega} = \frac{\lambda_0^{\omega}}{2}\frac{1}{\pi\theta_0^{2\omega}} \tag{16}$$

$$W_0^{2\omega} = \sqrt{\frac{\lambda_0^{\omega}}{2}\frac{z_0^{2\omega}}{\pi}} \tag{17}$$

$$k^{2\omega} = \frac{2\pi n^{2\omega}}{\left(\lambda_0^{\omega}/2\right)} \tag{18}$$

The corresponding expressions for $W^{2\omega}(z)$ and $R^{2\omega}(z)$ are exactly analogous to those in Equations (12) and (13), respectively, using the values of $W_0^{2\omega}$ and $z_0^{2\omega}$ from Equations (17) and (16). From these collective equations, the following expression describes the electric field for a propagating doubled frequency in the region adjacent to the focal volume.

$$E_i^{2\omega} = E_0^{2\omega}\frac{W_0^{2\omega}}{W^{2\omega}(z)}\exp\left(\frac{-\rho^2}{W^{2\omega}(z)}\right)\exp\left[-i\left(k_z^{2\omega}z + k_z^{2\omega}\frac{\rho^2}{2R^{2\omega}(z)} - atan\left(\frac{z}{z_0}\right)\right)\right] \tag{19}$$

In Equation (19), the expression describes the field arising from a pre-existing beam at the doubled frequency with a far-field amplitude of $E_0^{2\omega}$ but with characteristics identical to those expected for SHG within the focal volume.

In practice, the SHG field in a given Δz slice within the focal volume will consist of the coherent addition of the SHG produced in that slice with the pre-existing SHG generated from preceding slices. For coherent addition within a single crystal and under

phase-matched conditions, this summation produces a quadratic scaling of the field with propagation along z. Introducing both the quadratic scaling and the tensor describing frequency conversion in the crystal yields the following expression for the incremental addition to the field at each location from SHG.

$$E_i^{2\omega} = \left(\chi^{(2)};\hat{e}_j\hat{e}_k\right)\frac{W_0^{2\omega}}{W^{2\omega}(z)}\exp\left(\frac{-\rho^2}{W^{2\omega}(z)}\right)\exp\left[-i\left(k_z^{2\omega}z + k_z^{2\omega}\frac{\rho^2}{2R^{2\omega}(z)} - atan\left(\frac{z}{z_0}\right)\right)\right] \quad (20)$$

The factor of $\left(\chi^{(2)};\hat{e}_j\hat{e}_k\right)$ is a scalar proportionality constant describing the *i*-polarized doubled field produced within a crystal when driven by unit *j*-polarized and *k*-polarized fundamental fields, with all the spatial and angular information contained in the term to the right of this factor. In general, the net field at each location within the crystal will consist of the coherent sum of the SHG produced previously with that generated by each next slice. For a crystal positioned with the front face in the focal plane at $z = 0$, the net SHG is generated by integration over the intensity and phase of each contribution within the focal volume and the crystal from the front crystal face the interaction length l_{int}.

$$I_{net}^{2\omega} \propto \left|\int_0^{\infty}\int_0^{l_{int}} \left|E^{2\omega}(z,\rho)\right|^2 e^{i\delta}\,dz\,d\rho\right|^2 \quad (21)$$

The phase term δ in Equation (21) is given by the argument between the squared fundamental beam and the propagating second harmonic beam.

$$\delta(z,\rho) = \arg\left[\frac{\left(E^{\omega}(z,\rho)\right)^2}{E^{2\omega}(z,\rho)}\right] \quad (22)$$

In the absence of dispersion, only the Guoy phase shift given by the *atan* term in (19) will influence the relative phase between the fundamental and doubled frequencies (the sign change across the focal volume inverts the phase of the doubled frequency, but the quadratic dependence on the fundamental results in no sign change in the incremental contributions from SHG). However, the Guoy shift varies slowly when using low NA optics and rarely needs to be explicitly considered. In the presence of dispersion, the phase shift in Equation (22) typically results in oscillations in the SHG as a function of crystal thickness than vary with a periodicity approximately equal to the forward coherence length.

5.3 Experimental

5.3.1 Sample Preparation

500 nm diameter barium titanate ($BaTiO_3$) nanoparticles were purchased from US Research Nanomaterials, Inc. and suspended in polyethylene glycol (PEG, MW = 380-420 g/mole) in between cover slips was used for the preliminary study. The size distribution was confirmed using scanning electron microscopy (SEM). In order to prepare sample 0.01 g of BaTiO3 nanoparticles were added and mixed in 1g of molten PEG, which was kept in a hot water bath.

Sucrose was ground using a mortar and a pestle to make fine powder. The powder was sieved through a 25x25 μm^2 mesh before loading into 400 μm inner diameter square capillary tubes. All the capillaries were loaded up to similar height (~0.7 cm).

5.3.2 Simulations

Representative optical constants for the simulations were obtained using literature values. The refractive indices for 1,4-dioxane, 1,5-pentanediol, 1-butanol, propanol, acetonitrile, methanol, toluene, and benzene were generated from a five-parameter Cauchy equation using the coefficients from Moutzouris *et al*.[23] Optical constants for ethylene glycol were taken from Sani and Dell'Oro,[24] propylene glycol from Otanicar *et al.*,[25] acetone, methyl salicylate, ethyl salicylate, and cinnamaldehyde from Rheims *et al*.,[26] nitrobenzene and ethanol from Kedenburg *et al*.,[272630] and styrene from Sultanova *et al*.[28]

5.3.3 Imaging

A built-in-house beam scanning microscope was used in this experiment for Z-sectioning. A Tsunami ultrafast Ti:Sapphire mode-locked laser (800 nm, 80 MHz, 125 fs, 10 mW) was focused through a 10x objective (Nikon Plan Fluor, 0.30 N.A.), and the beam was scanned over the sample using a resonant fast-scan mirror (7.8 KHz, CambridgeTech) and a galvanometer slow-scan mirror. Z-scanning was achieved by translating the sample with a Newport motion controller. The detected SHG was collected back through the objective followed by a 680 nm long pass filter to a photomultiplier tube. A synchronous-digitization data acquisition module was used to time the data acquisition to the laser pulse frequency through a 10 MHz phase locked loop.[29] Images were created by binning the recorded SHG intensities into 512x512 pixels. Spatial resolution of this microscope was calibrated to 0.87 μm/pixel using a 1951 USAF resolution test grid. All measurements were performed with epi-detection on powders with thicknesses significantly greater than the

scattering length, such that the recovered SHG consists of contributions from both the directly backward-generated SHG and the forward-generated then subsequently backward scattered SHG. As such, it is assumed that the detected SHG collected by the objective provided a representative sampling proportional to the overall net SHG intensity produced from a given location.

5.4 Results and Discussion

5.4.1 Modeling the Impact of Numerical Aperture

An optical model is proposed, which explicitly considers a focused Gaussian beam, optical scattering effects, and phase matching. Predictions of the model are shown in Figure 5.2, highlighting the influence of the numerical aperture and tightness of focus on the disparity between the total SHG intensities produced from phase matched (PM) and non-phase matched (NPM) materials. Consistent with microscopy measurements, the traces correspond to single crystals rather than ensemble averages, differing only in the PM versus NPM nature of the nonlinear optical interaction. Calculations were performed using average refractive indices at 1064 nm and 532 nm, for sets of both non-aromatic and aromatic organic condensed phases as a function of the mean particle size (given by the equivalent radius R). In the PM cases, the depth of field dictated the interaction lengths, while in all the NPM cases considered the interaction length was limited by the scattering length. Several noteworthy trends emerge from the modeling predictions.

First and foremost, the difference between the SHG produced from PM and NPM crystallites is dramatically reduced with increases in the numerical aperture (NA). For the

nonaromatic organics with relatively long coherence lengths of ~31 μm, the ratio of the PM to NPM SHG intensities, $I_{PM}^{2\omega} / I_{NPM}^{2\omega}$, for a 100 μm crystal was 1.4, corresponding to only a 40% increase for PM crystallites. In contrast, that number jumped to $I_{PM}^{2\omega} / I_{NPM}^{2\omega} = 15$ for an NA of 0.1, and $I_{PM}^{2\omega} / I_{NPM}^{2\omega} = 32$ for an NA of 0.05. The marked decline in sensitivity to PM versus NPM in the 0.3 NA case arises as the coherence length l_c becomes small relative to the interaction length, which in the limit of large particles relative to l_c is set by the depth of field (corresponding to ~7 μm for a 0.3 NA and a 1064 nm source).

The preceding analysis espousing the benefits of higher NA measurements are partially offset in practice by a generally competing desire to reduce uncertainties from non-representative sampling, in which the measurements may be biased by not sampling a sufficiently large statistical population of particle sizes and orientations. Non-representative sampling can generally be minimized by expanding analyses to large fields of view to probe a greater population of crystallites. However, accessing a larger field of view by lower magnification generally corresponds to the use of a lower NA objective. Consequently, fewer total fields of view are required to generate results that statistically sample all crystal orientations, suggesting the desire for low magnification, low numerical aperture objectives.

In the present study, a balance was struck between these two competing forces based on analysis of the anticipated coherence length expected in a non-aromatic organic solid. Unfortunately, the optical constants of many organic solids are challenging to measure and/or find reported in the literature. However, a wealth of data exists for the wavelength dependent optical constants of pure organic liquids, which can serve as

surrogates for general estimations of coherence lengths in condensed phase organic materials. Pooling the results from 14 organic liquids yields an average coherence length for SHG with 1064 nm incident light of 24 μm (±11 μm). Considering just the non-aromatic organics consistent with sucrose increases the coherence length to 31 μm (±6 μm). Both of these values are on par with or greater than the ~17 μm depth of field obtained for the 10x objective used (detailed in the next section), such that the depth of field of the objective is likely to dictate the upper limit on the net interaction length rather than the forward coherence length. A higher NA objective would further reduce the impact of the forward coherence length, but would also likely sample a significantly smaller field of view with corresponding increases in total measurement time for representative sampling.

5.4.2 Isolated Point Source Measurements

As a prelude to powders analysis, a series of measurements was performed using $BaTiO_3$ nanoparticles as ground-truth point sources for characterizing the influence of particle position and orientation on the detected SHG intensity. Results highlighting two effects are shown in Figure 5.3. As one might expect, the brightness of SHG in any given field of view varied considerably from nanoparticle to nanoparticle, both due to the axial position of the particles relative to the focal plane and due to orientational effects. The axial position-dependence was corrected by analyzing each particle relative to the focal plane producing the maximum SHG intensity, as a prelude to analogous operations in powders. Measurements acquired without shifting result in significant broadening in the Z-profile due to convolution with the random distribution in position. Optical sectioning of a point

source (in this experiment 500 nm $BaTiO_3$ nanoparticles following Z-shifting) returns the squared intensity profile of the fundamental beam because the convolution of any function with an impulse function replicates the function centering the position at impulse.[30,31] From a selective cropping of 25 nanoparticles throughout the whole stack, a new image stack (125 pixels x125 pixels x length of z-scan) was created. A square area (30x30 pixels) around the particle was selected and cropped out from the entire stack. Following Z-correction, the integrated intensity as a function of axial displacement is well-fit to a Lorentzian distribution in Figure 5.3b., consistent with expectations for a Gaussian incident beam.[22] The recovered depth of field of 16.9 ± 0.1 μm (given by twice the Rayleigh range) is larger than the theoretically expected of 7.07 μm for a 0.3 N.A. 10X objective with an incident wavelength of 1064 nm, suggesting underfilling of the objective for an effective NA of 0.2.

From the Z-corrected images, a histogram of particle brightness is shown in Figure 5.3c. The measured distribution in blue is overlaid with the theoretical distribution in red generated from Monte Carlo simulations of the anticipated SHG intensity in which all nanoparticle orientations are equally probable. No adjustable parameters were used in the generation of the theoretical results, which were produced using previously reported tensor elements for $BaTiO_3$.[32] All simulated results were based on the hyperpolarizability of the lattice and independent of linear optical effects such as phase-matching. Since the nanoparticles are significantly smaller in dimension than the forward coherence length, the interplay between the linear and nonlinear optical properties is almost completely removed, with the observed SHG intensity per unit volume predicted and measured depending exclusively on the native hyperpolarizability of the lattice.

Despite the excellent correspondence between theory and experiment in studies of $BaTiO_3$ nanoparticles, the sample itself is not representative of typical powders. In general, the samples targeted for powders analysis by SHG will exhibit a diversity of sizes rather than be manufactured to within tight size tolerances as the case of the $BaTiO_3$ nanoparticles. Furthermore, most powders will exhibit much higher packing densities of SHG-active materials, with the density of $BaTiO_3$ carefully selected in the present study to ensure independent access to individual, well-separated nanoparticles. Nevertheless, the $BaTiO_3$ serves two important roles in the present work: i) for characterization of the axial profile of the beam as demonstrated in Figure 5.3b, and ii) for calibration as a reference material for absolute quantification of the lattice hyperpolarizabilities of powdered samples.

5.4.3 Crystal Orientation, Size, and Phase-Matching

The interdependence of the detected SHG intensity on the crystal size distribution and the differences in behaviors in the presence or absence of phase-matching are among the most challenging aspects for disentangling the linear and nonlinear optical properties in analyses of powdered samples. For collimated sources in which measurements are integrated over many crystals with many sizes and orientations, only a handful of experimental observables are dependent on numerous parameters related to the particles under analysis. However, SHG microscopy coupled with image analysis provides a convenient route forward by providing measurements on a per-particle basis.

Most directly, the theoretical framework developed in the Appendix suggests that the relatively rare occurrence of phase-matching in a phase matchable material can be

easily corrected by imaging. In the limit of the depth of field or scattering length being much smaller than the coherence length, the minor enhancement in the integrated SHG from relatively rare PM orientations are small enough to be neglected in the analysis. Conversely, as the NA is reduced and the mean particle size is increased, the disparity between the per-particle brightness under PM and NPM conditions rapidly increases. As the crystals become larger, a smaller fraction of them are opportunely oriented to generate phase matching, and the disparity between the brightness of those increasingly rare events and the NPM orientations becomes ever greater. Deviation from the anticipated behavior under NPM conditions illustrated in Figure 5.2 can be readily identified (e.g, by a statistical test), and the PM outliers separated for rejection or independent analysis.

Image analysis provides a means to both identify and correct SHG microscopy measurements in ways that have no simple analogs in measurements with collimated sources, such as in the Kurtz-Perry method. From inspection of the raw SHG images produced in powder measurements shown in Figure 5.5, only a relatively small fraction of the locations interrogated produced substantial SHG signals. The data shown in Figure 5.5b are Z-shifted on a per-pixel basis to remove effects related to variability in the axial positions of particles within the powder. Consequently, the dark locations in the images can be attributed to voids in the powder and/or regions rendered dark from scattering losses prior to intersection of the beam with SHG-active moieties.

In order to improve the accuracy of the determinations for the SHG-activity per unit volume of crystalline material, the void regions were omitted from the subsequent analysis. The void-rejection was accomplished based on maximization of the number of counted

particles in the image, illustrated in Figure 5.6. In brief, the number of particles identified in the images was determined as a function of an intensity threshold. For thresholds too low, coalescence between particles from dark counts and crystal overlap produced a small number of relatively large crystals. On the other extreme, too high of a threshold resulted in the identification of only a few of the very brightest crystals. Maximization of the particle number provides a reproducible compromise between potential bias introduced by these two limiting factors.

A z-test was performed to identify and reject anomalously bright rare particles in Figure 5.6 corresponding to potential phase-matched candidates. In brief, a single-sided confidence interval of 99.9% (i.e., 3σ) was used to identify particles statistically different from the parent population. Sucrose has been established as being phase-matchable,[33] such that the SHG intensity of a powder is potentially influenced greatly by the presence of a relatively small volume fraction of appropriately oriented crystals. However, the conditions for phase-matching constitute the exception rather than the rule, with the large majority of particles presenting in non-phase matched orientations. This disparity is clearly evident in Figure 5.6, in which the tail of the distribution in per-pixel brightness extends well into the wings to include a handful of anomalously bright particles. Particles with a per-pixel brightness exceeding three standard deviations (3σ) were removed from the pool prior to evaluation of the SHG activity per unit volume of crystalline material. This selective rejection strategy allowed both phase-matchable and nonphase-matchable materials to be characterized in equal mathematical footing. Rejection of the PM component in phase-matchable materials produced SHG intensities dominated by the inherent nonlinear optical

properties of the lattice largely independent of perturbations from linear optical effects in both PM and NPM materials.

5.4.4 Packing Density

Although often not explicitly included in models of powders, only the volume fraction of the powder that is present in the solid form can contribute to the detected SHG activity. As such, more densely packed powders of the same material are likely to produce a higher measured SHG intensity per unit area/volume than the same materials prepared with greater dead-volumes between crystallites. This effect is evident in Figure 5,7, in which the raw integrated SHG intensity was recorded at different positions within a capillary tube. The particle density toward the opening of the capillary is generally greater than in the interior, as higher forces are required to add additional material to a packed capillary than to fill the initially empty capillary tube. Consistent with these expectations, substantial variability was observed in the integrated SHG intensity recorded from different locations within the capillary tube.

Fortunately, the void rejection algorithm described in the preceding discussion on Crystal Orientation, Size, and Phase-Matching naturally accomplishes much of the corrections for packing density. A comparison of the integrated SHG intensity and the corresponding SHG activity per unit area correcting for voids is also given in Figure 5.7. In the uncorrected case, the variability from one field of view to another substantially exceeded the inherent measurement error, suggesting the dominant source of measurements variance was from systematic differences across multiple fields of view. However, the combination of dead-volume and bright outlier rejection resulted in a

statistically indistinguishable set of measurements at all locations along the capillary tube, with substantial corresponding reductions in measurement uncertainty.

Image analysis in this manner based on particle counting also has the additional advantage of directly providing the particle size distribution shown in Figure 5.8. Recovery of the full histogram of crystal sizes and the corresponding SHG activities on a per particle basis allows analyses that are fundamentally inaccessible from an integrating KP-type analysis, as detailed in the next section.

5.4.5 Prediction of the Model

The scattering model described in the Appendix results in several predictions that can be tested experimentally. Firstly, the model predicts a simple relationship between the mean particle size given by the equivalent radius R and the scattering length l_s of $l_s \cong R$. The fit of the ensemble-averaged SHG intensity as a function of Z-position in Figure 5.3 yields a value of l_s = 4.7 μm (±0.6 μm). From image analysis, a representative histogram of particle sizes for the sucrose powder explored are shown in Figure 5.8, with the mean particle area given by 82 μm^2. The particle area can be used to recover R by assuming an "equivalent sphere" scattering cross-section of πR^2,[16-18] yielding a value of R = 5.1 μm. Despite being calculated based on very different analyses, the values of l_s and R are easily within experimental error of each other, supporting the simple link between the mean particle size and the scattering length in the powder suggested by Equation 3 of the Appendix.

Because microscopy measurements recover a full histogram of size-dependent SHG activities, trends with respect to particle size can also be compared with theoretical predictions. The SHG activity per unit area is shown in Figure 5.9, calculated by combining the histogram of sizes with the integrated brightness on a per-particle basis. The experimental results are compared with predictions based on the model, assuming an interaction length dictated by the particle radius R when $R \leq l_s$ and by l_s when $l_s < R$. Good agreement is observed between the theoretical and experimental trends. Most notably, the model predicts fairly rapid saturation of the per-particle SHG with increasing particle radius in the regime $l_s < R$, in general agreement with observations.

From these combined measurements, the inherent mean SHG activity per unit volume can be recovered nominally independently of linear effects by combining the results from Figures 5.4 and 5.9. In brief, the volume is determined based by combining the mean SHG per unit area with the mean interaction length, in this case given by the scattering decay length of 4.7 μm when $R > l_s$ and by R for smaller particles. The SHG activity per unit volume is given by $\left\langle I^{2\omega}/V \right\rangle \cong \left\langle I^{2\omega}/A \right\rangle \Big/ \left(4l_s/3\right)$, where the factor of $4l_s/3$ arises from ratio of the volume to area of a sphere. The orientationally averaged values for the effective susceptibility of sucrose normalized to $BaTiO_3$ is 4.3%, corresponding to a ratio of the SHG intensity per unit volume of 0.19% relative to $BaTiO_3$. Using literature values for the susceptibility element of $BaTiO_3$ of d_{15} = 17.2 pm/V, d_{31} = 18.0 pm/V, and d_{33} = 6.6 pm/V,[32] isotropic orientational averaging as described by Bersohn *et al.*[34] for hyper-Rayleigh scattering (HRS) results in an effective susceptibility of $\left\langle \chi_{eff} \right\rangle_{\theta\psi\phi}$ = 17.7 pm/V for $BaTiO_3$. In brief, a statistical assembly of particles with uniformly distributed

orientations will converge to an isotropically averaged laboratory-frame squared magnitude of $\left\langle \vec{\chi}^{*}_{ZZZ}\vec{\chi}_{ZZZ} \right\rangle_{\theta\psi\phi}$ for coparallel polarized detection and $\left\langle \vec{\chi}^{*}_{YZZ}\vec{\chi}_{YZZ} \right\rangle_{\theta\psi\phi}$ for cross polarized detection, the square root of which was used to evaluate $\left\langle \chi_{eff} \right\rangle_{\theta\psi\phi}$. Using the 4.3% scaling yields a corresponding value for sucrose of $\left\langle \chi_{eff} \right\rangle_{\theta\psi\phi}$ = 0.76 pm/V.

The results obtained in the present study correspond to a per-volume SHG activity for sucrose that are roughly an order of magnitude larger than previous reports. In early studies by Kurtz and coworkers using KDP powder as a reference material, SHG activities of ~0.08 pm/V were reported based on measurements of powders prepared by mechanical grinding with sizes on the order of 40-120 μm.[33] Similar results were obtained in more recent studies by Piela and coworkers, in which the SHG coefficients for sucrose were determined to be ~0.11 pm/V (also prepared by mechanical grinding, but with no estimation of the anticipated size distribution).[35] In contrast, the present measurements were performed for a powder with a mean particle size of only ~10 μm in diameter and a much shorter interaction length. Two likely possibilities emerge for the disparity: i) the microscopy measurements of sucrose produce a higher per-volume SHG activity than conventional powder measurements, or ii) the microscopy measurements of $BaTiO_3$ nanoparticles yield lower than anticipated per-volume SHG activity. A combination of both effects is possible. In the case of sucrose, the interaction length may have been over-estimated if based on the coherence length rather than the scattering length, such that the effective volume over which the SHG activity arose was smaller than anticipated. Furthermore, if the $BaTiO_3$ reference nanoparticles were not perfectly single-crystalline or included an amorphous surface layer, the effective volume contributing to the detected

SHG may be less than the geometrical particle volume, leading to a corresponding over-estimation of the sucrose activity. We tentatively attribute the disparity primarily to the first of the two considered interactions, as a fair body of work has evolved supporting the formation of single-domain $BaTiO_3$ particles in the size regime used herein (500 nm).[36,37] The good agreement between the predictions and observations in the SHG microscopy analysis presented herein are consistent with recent comparisons between predicted and measured SHG activities of several pharmaceutical solids based on SHG imaging. In that previous work, generally good agreement was observed between the integrated SHG intensity measured using an objective with a comparable NA and *ab initio* predictions based on molecular hyperpolarizability calculations for the lattices. This agreement is quite remarkable, as no corrections for phase-matching were made to the measurements and no particle size information was recorded or used in the analysis.

As a consequence of its preferential selectivity for the nonlinear optical properties alone, SHG microscopy using a suite of different NA's as illustrated in Figure 5.2 generally provides information that is highly complementary to that recovered by the Kurtz-Perry method.[19] The KP method yields integrated values depending on both the linear and nonlinear optical properties, particularly in phase-matchable materials. However, much of the SHG intensity in a phase-matchable material arises from a relatively small population of appropriately oriented crystallites. As the mean particle size increases, the number of particles capable of PM measurements is linearly reduced and the brightness per PM particle quadratically increased, resulting in an overall linear intensity scaling with mean particle size.[16] Consequently, the statistical tests designed to selectively identify outliers should be significantly more effective as the particle size is increased. SHG microscopy

measurements as a function of NA can potentially not only provide the inherent lattice hyperpolarizability from the statistical population of SHG activities, but also clearly identify between phase-matchable and non-phase matchable materials based on simple statistical outlier tests of particle brightness.

5.5 Summary

A method is described for removing phase-matching effects in SHG measurements of powders. The general measurement flow is as follows:

1. Record a *Z*-stack of SHG microscopy measurements for the powder in question

2. Process images as illustrated in Figure 5.5: i) *Z*-shift the pixels such that the maximum intensity in the *Z*-stack at every position is at $Z = 0$, ii) for the $Z = 0$ plane, select a lower intensity threshold based on maximizing the total number of particles in an image or set of images, and iii) reject outlying particles with intensities greater than three standard deviations of the mean, corresponding to possible phase-matched orientations.

3. Measure the attenuation length by integrating the SHG intensity in each *Z*-plane and fitting the result to the Lorentzian⊗exponential convolution as illustrated in Figure 5.4.

4. Determine the asymptotic value of the SHG intensity per unit area $\left\langle I^{2\omega}/A \right\rangle$ in the limit of large *R* using particle counting algorithms as illustrated in Figure 5.9.

5. Convert $\left\langle I^{2\omega}/A \right\rangle$ to the average SHG intensity per unit volume $\left\langle I^{2\omega}/V \right\rangle$ by dividing by the effective interaction length. Depending on the numerical aperture and average crystal size, the interaction length could be dictated by the scattering length l_s, the depth of field

l_d, or the average forward coherence length l_c. The corresponding scaling of the interaction lengths to convert to effective volume in each case are derived explicitly in the Appendix.

a. If $l_s << (l_c, l_d)$, $\left\langle I^{2\omega}/V \right\rangle \cong \left\langle I^{2\omega}/A \right\rangle / \left(4 l_s/3\right)$

b. If $l_d << (l_c, l_s)$, $\left\langle I^{2\omega}/V \right\rangle \cong \left\langle I^{2\omega}/A \right\rangle / l_d$

c. If $l_c << (l_d, l_s)$, $\left\langle I^{2\omega}/V \right\rangle \cong \left\langle I^{2\omega}/A \right\rangle / \left(\pi l_c/2\right)$

6. Normalize the recovered <SHG/V> to a standard (e.g., $BaTiO_3$ nanoparticles of known size).

Measurements performed using this approach for sucrose powder yielded good agreement between several theoretical predictions and experimental observations. The measured scattering length was found to be in excellent agreement with the effective radius based on the particle size distribution determined by image analysis of SHG micrographs. The model also resulted in marked reductions in measurement uncertainties related to variance in packing density. Furthermore, the SHG-activity as a function of particle size could be determined by taking advantage of the inherent variability in crystal dimensions within a powder, yielding size-dependent SHG activity in good general agreement with the expectations of the model from a single powder sample with no adjustable parameters.

5.6 Conclusion

The proposed microscopy-based approach provides a nice complement to alternative established approaches based on ensemble averaged measurements with collimated or gently focused incident beams. In particular, the proposed approach yields measurements that are largely immune to complications from phase-matching, providing measurements of the nonlinear susceptibility more directly tied to the native nonlinear optical properties of the lattice.

5.6 References

1 Clevers, S. *et al.* Detection of order–disorder transition in organic solids by using temperature resolved second harmonic generation (TR-SHG). *Journal of Molecular Structure* **1078**, 61-67, doi:10.1016/j.molstruc.2014.04.007 (2014).

2 Clevers, S., Simon, F., Sanselme, M., Dupray, V. & Coquerel, G. Monotropic Transition Mechanism ofm-Hydroxybenzoic Acid Investigated by Temperature-Resolved Second Harmonic Generation. *Crystal Growth & Design* **13**, 3697-3704, doi:10.1021/cg400712s (2013).

3 Simon, F., Clevers, S., Dupray, V. & Coquerel, G. Relevance of the Second Harmonic Generation to Characterize Crystalline Samples. *Chemical Engineering & Technology* **38**, 971-983, doi:10.1002/ceat.201400756 (2015).

4 Clevers, S., Simon, F., Dupray, V. & Coquerel, G. Temperature resolved second harmonic generation to probe the structural purity of m-hydroxybenzoic acid. *Journal of thermal analysis and calorimetry* **112**, 271-277 (2013).

5 Galland, A. *et al.* Spotting conglomerates by second harmonic generation. *Crystal Growth and Design* **9**, 2713-2718 (2009).

6 Newman, J. A. *et al.* Parts per Million Powder X-ray Diffraction. *Analytical chemistry* **87**, 10950-10955 (2015).

7 Lee, C. J., Strachan, C. J., Manson, P. J. & Rades, T. Characterization of the bulk properties of pharmaceutical solids using nonlinear optics□a review. *Journal of pharmacy and pharmacology* **59**, 241-250 (2007).

8 Rawle, C. B. *et al.* Towards characterization and identification of solid state pharmaceutical mixtures through second harmonic generation. *Journal of pharmaceutical sciences* **95**, 761-768 (2006).

9 Strachan, C. J., Lee, C. J. & Rades, T. Partial characterization of different mixtures of solids by measuring the optical nonlinear response. *Journal of pharmaceutical sciences* **93**, 733-742 (2004).

10 Thomas, S. P., Nagarajan, K. & Row, T. G. Polymorphism and tautomeric preference in fenobam and the utility of NLO response to detect polymorphic impurities. *Chemical Communications* **48**, 10559-10561 (2012).

11 Strachan, C. J., Windbergs, M. & Offerhaus, H. L. Pharmaceutical applications of non-linear imaging. *International journal of pharmaceutics* **417**, 163-172 (2011).

12 Schmitt, P. D., Trasi, N. S., Taylor, L. S. & Simpson, G. J. Finding the Needle in the Haystack: Characterization of Trace Crystallinity in a Commercial Formulation of Paclitaxel Protein-Bound Particles by Raman Spectroscopy Enabled by Second Harmonic Generation Microscopy. *Molecular pharmaceutics* **12**, 2378-2383 (2015).

13 Wanapun, D., Kestur, U., Taylor, L. & Simpson, G. Single particle nonlinear optical imaging of trace crystallinity in an organic powder. *Analytical chemistry* **83**, 4745-4751 (2011).

14 Wanapun, D., Kestur, U. S., Kissick, D. J., Simpson, G. J. & Taylor, L. S. Selective detection and quantitation of organic molecule crystallization by second harmonic generation microscopy. *Analytical chemistry* **82**, 5425-5432 (2010).

15 LeCaptain, D. J. & Berglund, K. A. The applicability of second harmonic generation for in situ measurement of induction time of selected crystallization systems. *Journal of crystal growth* **203**, 564-569 (1999).

16 Aramburu, I., Ortega, J., Folcia, C. & Etxebarria, J. Second harmonic generation by micropowders: a revision of the Kurtz–Perry method and its practical application. *Applied Physics B* **116**, 211-233 (2014).

17 Aramburu, I., Ortega, J., Folcia, C. & Etxebarria, J. Second-harmonic generation in dry powders: A simple experimental method to determine nonlinear efficiencies under strong light scattering. *Applied Physics Letters* **104**, 071107 (2014).

18 Aramburu, I. *et al.* Accurate determination of second order nonlinear optical coefficients from powder crystal monolayers. *Journal of Applied Physics* **109**, 113105 (2011).

19 Kurtz, S. & Perry, T. A powder technique for the evaluation of nonlinear optical materials. *Journal of Applied Physics* **39**, 3798-3813 (1968).

20 Kiguchi, M., Kato, M., Okunaka, M. & Taniguchi, Y. New method of measuring second harmonic generation efficiency using powder crystals. *Applied physics letters* **60**, 1933-1935 (1992).

21 Kiguchi, M., Kato, M., Kumegawa, N. & Taniguchi, Y. Technique for evaluating second□order nonlinear optical materials in powder form. *Journal of applied physics* **75**, 4332-4339 (1994).

22 Saleh, B. E., Teich, M. C. & Saleh, B. E. *Fundamentals of photonics*. Vol. 22 (Wiley New York, 1991).

23 Moutzouris, K. *et al.* Refractive, dispersive and thermo-optic properties of twelve organic solvents in the visible and near-infrared. *Applied Physics B* **116**, 617-622 (2014).

24 Sani, E. & Dell'Oro, A. Optical constants of ethylene glycol over an extremely wide spectral range. *Optical Materials* **37**, 36-41 (2014).

25 Otanicar, T. P., Phelan, P. E. & Golden, J. S. Optical properties of liquids for direct absorption solar thermal energy systems. *Solar Energy* **83**, 969-977 (2009).

26 Rheims, J. & Wriedt, T. Refractive-index measurements in the near-IR using an Abbe refractometer. *Measurement Science and Technology* **8**, 601 (1997).

27 Kedenburg, S., Vieweg, M., Gissibl, T. & Giessen, H. Linear refractive index and absorption measurements of nonlinear optical liquids in the visible and near-infrared spectral region. *Optical Materials Express* **2**, 1588-1611 (2012).

28 Sultanova, N., Kasarova, S. & Nikolov, I. Dispersion Proper ties of Optical Polymers. *Acta Physica Polonica-Series A General Physics* **116**, 585 (2009).

29 Muir, R. D., Sullivan, S. Z., Oglesbee, R. A. & Simpson, G. J. Synchronous digitization for high dynamic range lock-in amplification in beam-scanning microscopy. *Review of Scientific Instruments* **85**, 033703 (2014).

30 Bracewell, R. The fourier transform and iis applications. *New York* **5** (1965).

31 Sibarita, J.-B. in *Microscopy Techniques* 201-243 (Springer, 2005).

32 Pressley, R. J. & Company, C. R. *CRC handbook of lasers: with selected data on optical technology*. (Chemical Rubber Co., 1971).

33 Bourhill, G. *et al.* Powder second harmonic generation efficiencies of saccharide materials. *Chemistry of materials* **5**, 802-808 (1993).

34 Bersohn, R., Pao, Y. H. & Frisch, H. Double□Quantum Light Scattering by Molecules. *The Journal of Chemical Physics* **45**, 3184-3198 (1966).

35 Szostak, M. M., Piela, K., Hołderna-Natkaniec, K., Natkaniec, I. & Bidzińska, E. Optical nonlinearity and electric conductivity origin study on sucrose crystal by using IR, Raman, INS, NMR, and EPR spectroscopies. *Carbohydrate research* **395**, 29-37 (2014).

36 Kim, E. *et al.* Second-harmonic generation of single BaTiO3 nanoparticles down to 22 nm diameter. *ACS nano* **7**, 5343-5349 (2013).

37 Rogov, A., Mugnier, Y. & Bonacina, L. Harmonic nanoparticles: noncentrosymmetric metal oxides for nonlinear optics. *Journal of Optics* **17**, 033001 (2015).

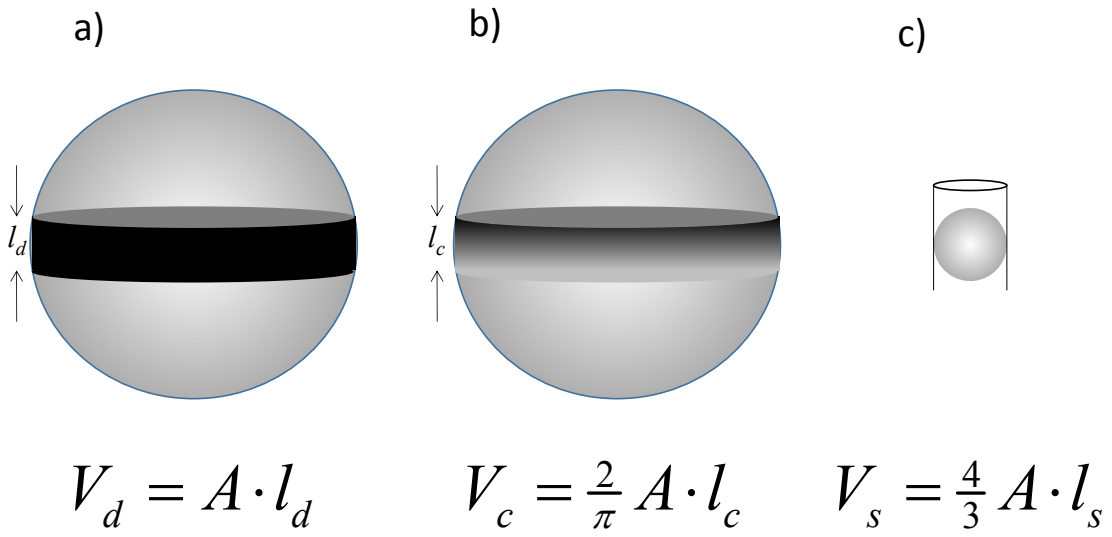

Figure 5.1: Pictorial depiction of the effective volumes associated with the different limiting interaction lengths. In a), the total volume is given by the product of the geometrical area and the depth of field. In b), the coherence length is scaled by a cosine function, illustrated by the gray-scale in the disc. In c), the volume is equivalent to that of a sphere of cross-section πR^2.

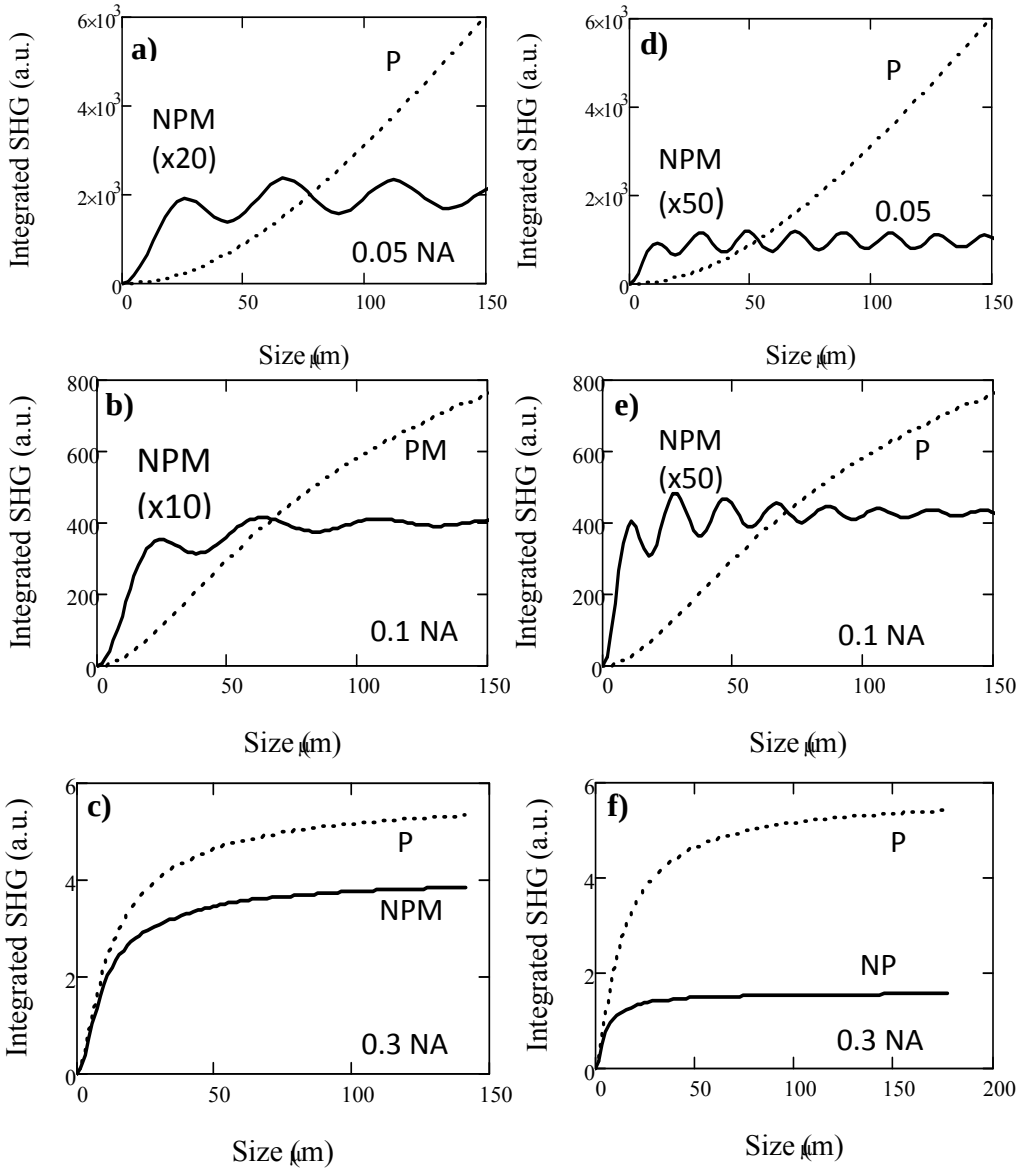

Figure 5.2. Theoretical SHG activity of a powder under phase matched (PM) and non-phase matched (NPM) conditions calculated for different numerical apertures, in which the interaction length is dictated by the dimensions of the particle or the optical scattering length (whichever is shorter). The top curve corresponds most closely to the conventional KP method using nominally collimated light, while the bottom is more representative of the measurement configuration used in the present study. Calculations were performed using average optical constants and coherence lengths from nine non-aromatic (a-c) and seven aromatic (d-f) organic molecules.

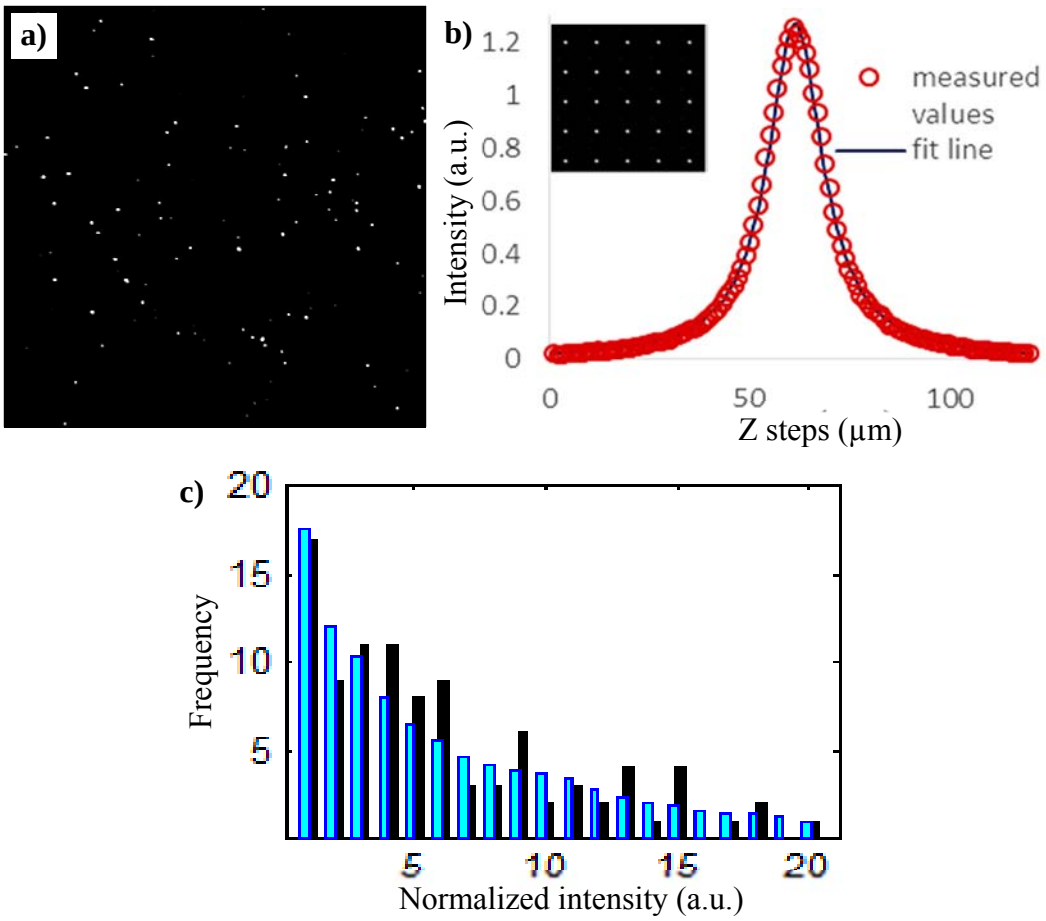

Figure 5.3: Recovery of the beam intensity profile as a function of axial position. a) Image of the brightest frame from the optical sectioning of 500nm $BaTiO_3$ nanoparticles suspended in polyethylene glycol. 25 nanoparticles were randomly chosen from the raw image and cropped with 30x30 pixels centering the corresponding particle to make a new image stack. Surface of each individual nanoparticle's area was shifted accordingly to bring all nanoparticles in the same focal plane. b) Shows the fitting of the measured SHG intensity to a Lorentzian function. Each circle corresponds to the mean integrated SHG of each frame from the new surface shifted image stack. The recovered Rayleigh range of the Lorentzian beam profile was 8.44±0.05 μm. The brightest frame of the new image stack is shown in the inset. (C) Intensity distribution of particles (filled column) from the brightest frame of a surface shifted image *(N* = 97), compared to the theoretical prediction of the intensity distribution (lightly filled) based on literature values for the tensor elements of $BaTiO_3$.

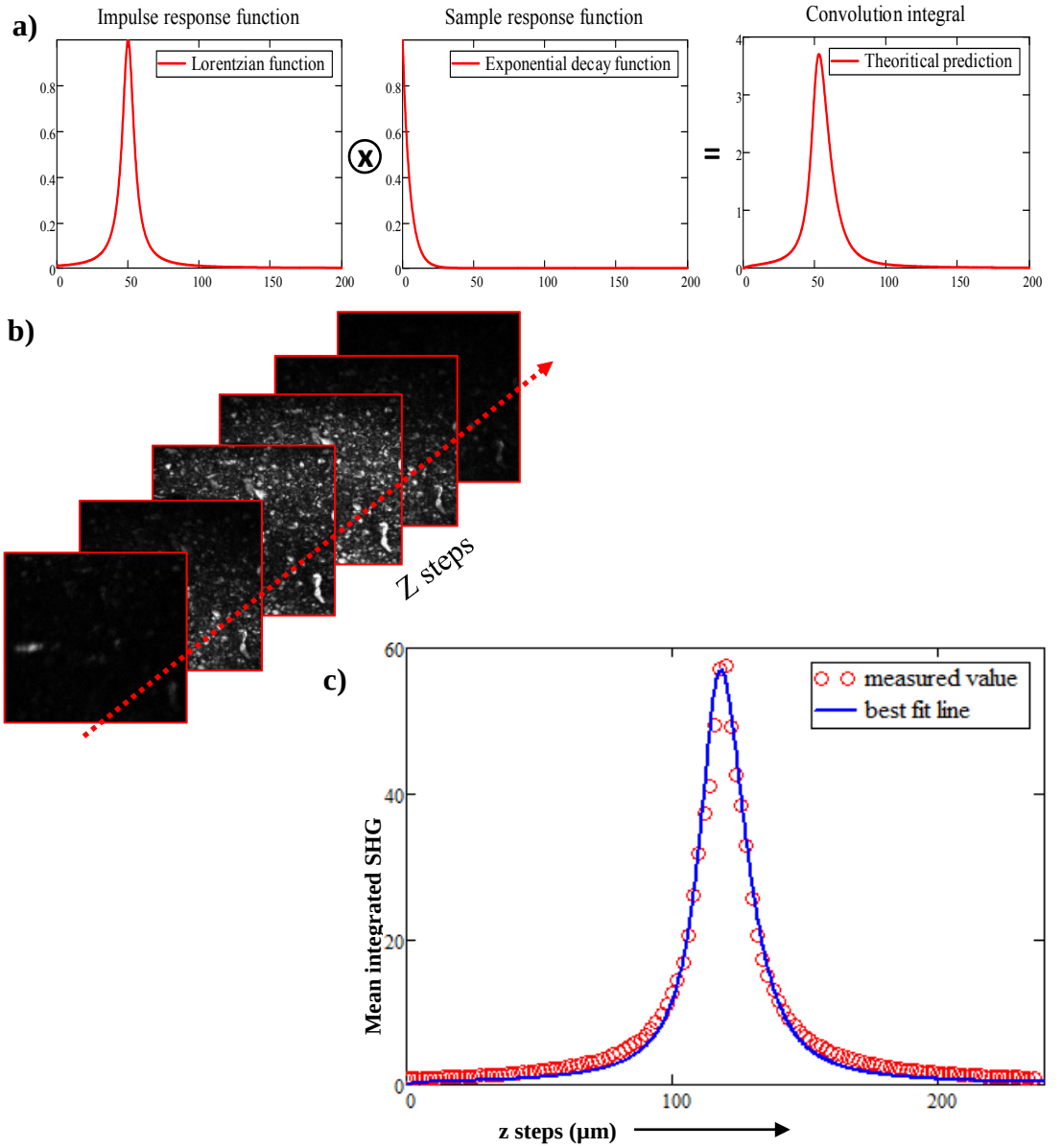

Figure 5.4: Determination of the scattering length l_s. a) A depicted analytical expression for the measured intensity from an optical sectioning, which is a convolution of a Lorentzian beam profile with a single-sided exponential decay function. b) Representative image of optical sectioning. c) Corresponds to the mean integrated SHG from the surface shifted image fitted to the convolution integral. Using the measured Rayleigh range of the Lorentzian function from Figure 2, the recovered scattering length was 4.7± 0.6 µm.

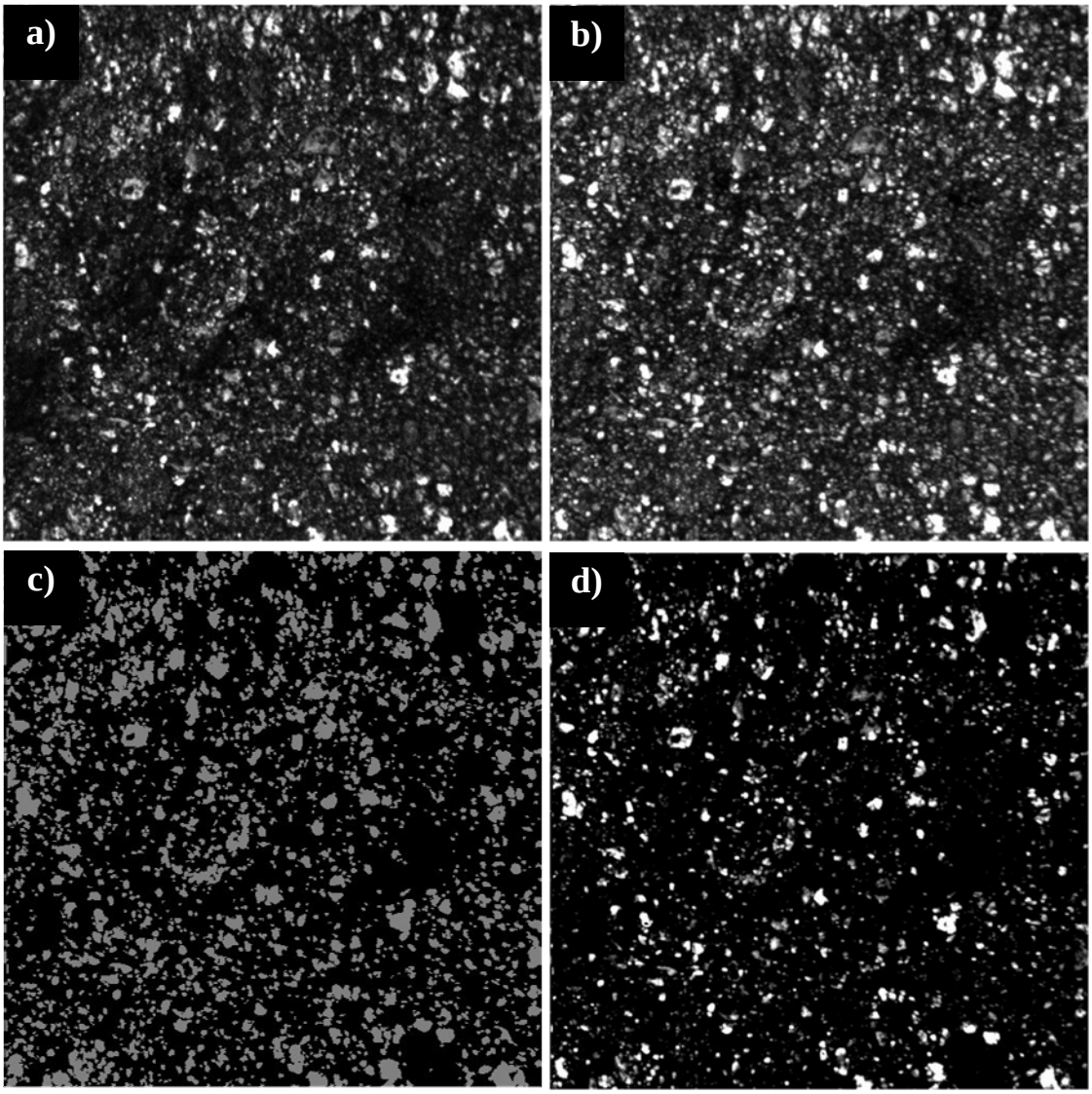

Figure 5.5: Illustration of the image processing. (a) Representative SHG image of sample surface, (b) brightest frame following per-pixel Z-shifting, (c) binary mask containing particles size 4μm^2< area of particles <625 μm^2, (d) representative raw image of sample surface after all the processing.

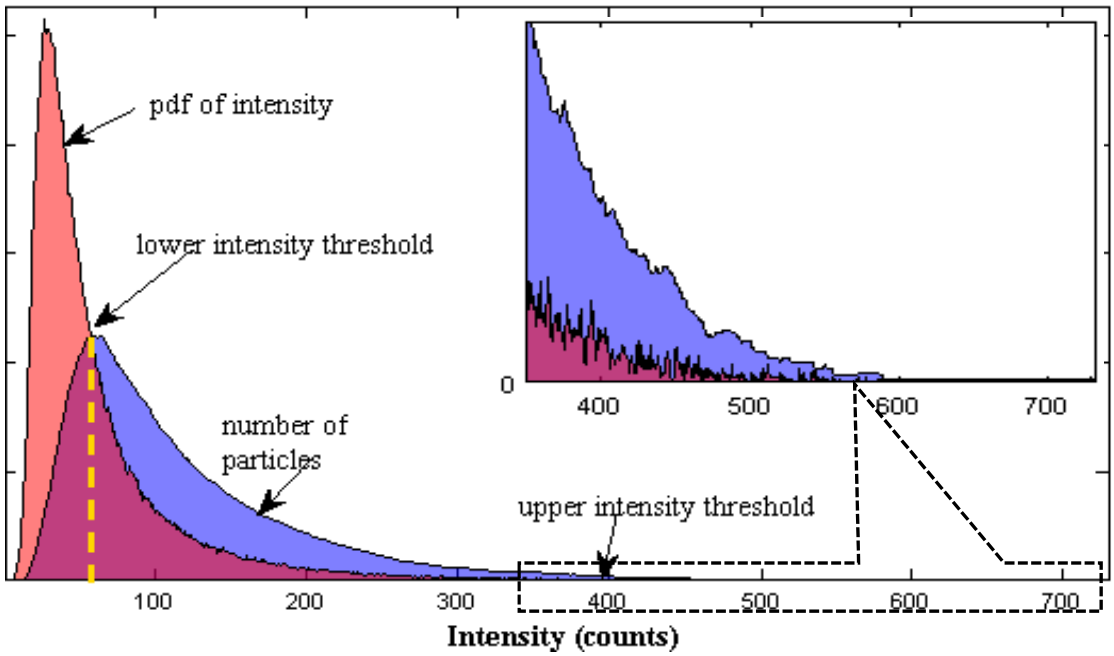

Figure 5.6: Illustration of the approach used to select the lower and upper thresholds prior to particle counting. The red plot to the left represents the histogram of per-pixel intensities from the brightest frame of a Z-shifted stack. The blue plot to the right represents the number of particles recovered from the brightest image frame. The yellow dashed line indicates the lower intensity threshold that maximizes the number of particles. The upper intensity threshold was set by discarding values exceeding standard deviations (3σ) of the mean intensity.

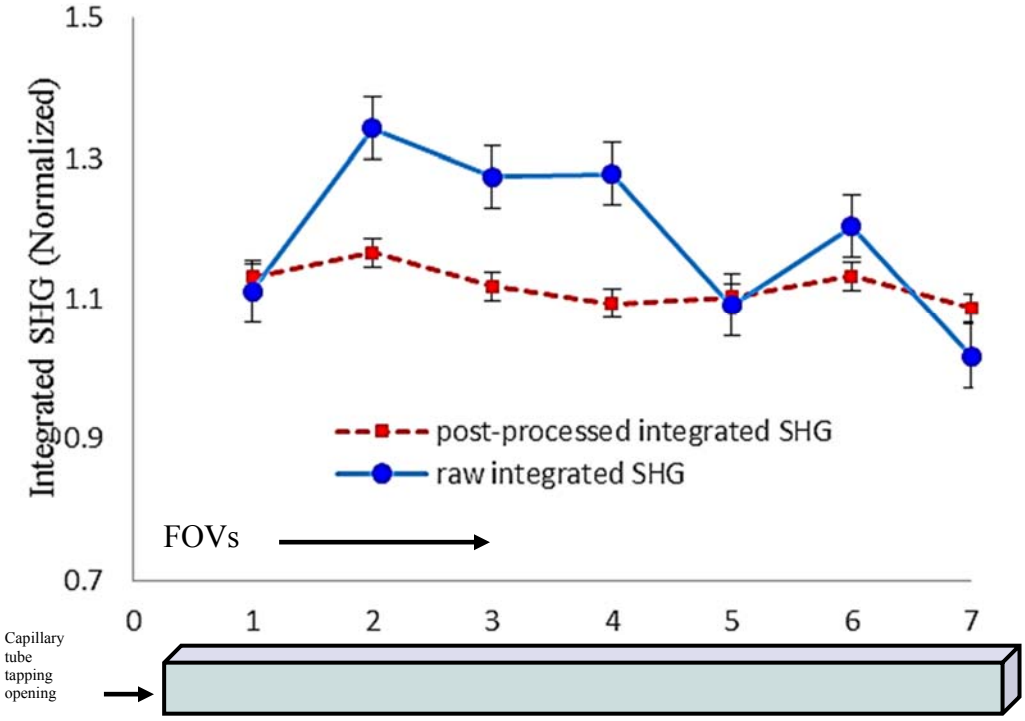

Figure 5.7: Comparison of the raw versus corrected SHG intensity measured from the different locations in a packed capillary tube (normalized to 500 nm of $BaTiO_3$ nanoparticles). Measurement uncertainty was reduced ~90% by combining SHG measurements with image analysis.

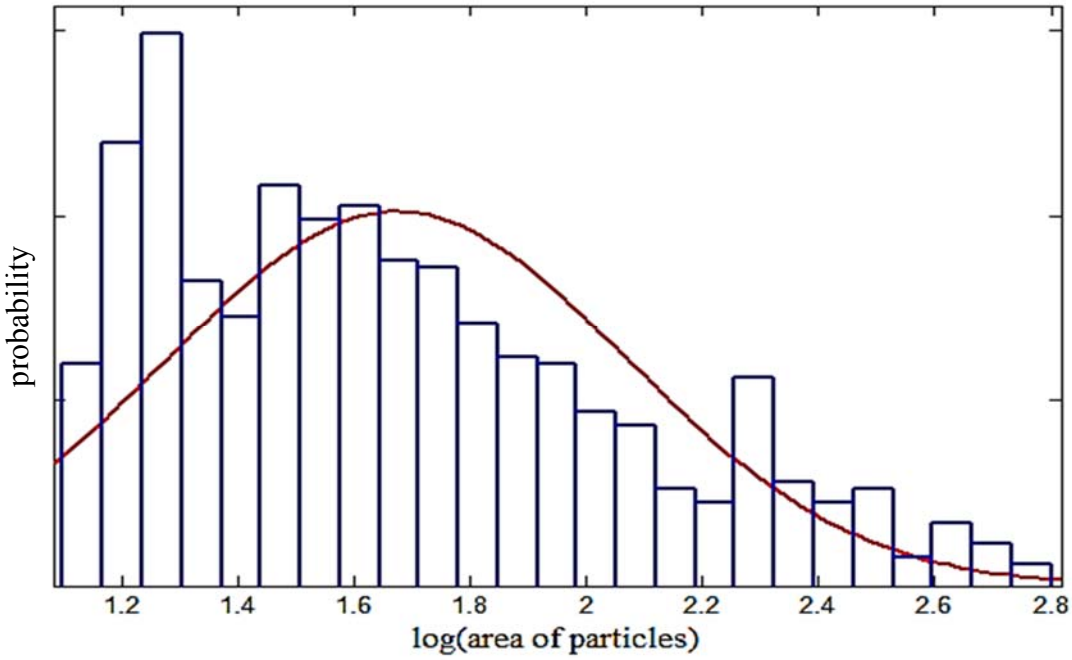

Figure 5.8: Histogram of $\log_{10}$(particle area) fitted to a normal distribution, corresponding to a log-normal distribution in particle sizes. The mean particle size was 82 μm^2.

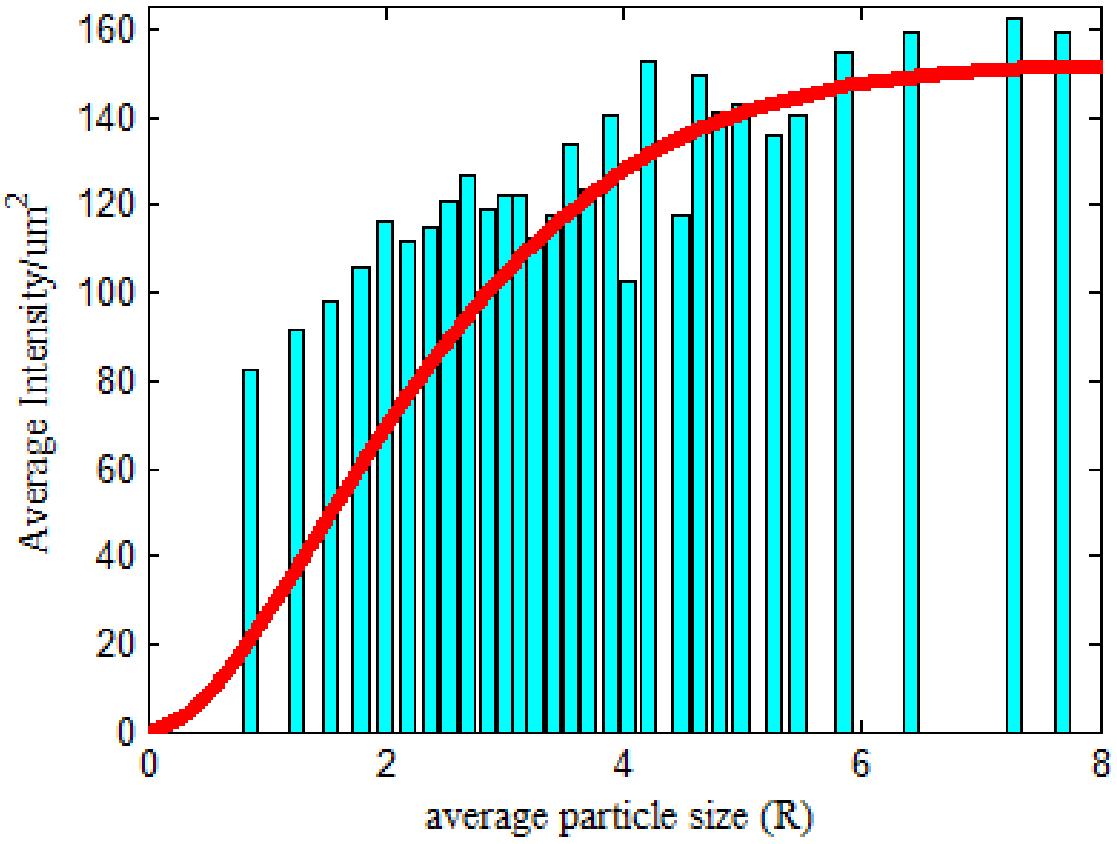

Figure 5.9: The measured size-dependent SHG intensity recovered from the histogram of particle intensities (vertical bars) is compared with the theoretical predictions of the model using the measured scattering length with the intensity scaling as the only adjustable parameter (solid curve).

VITA

VITA

Azhad Ul-Alam Chowdhury was born on December 15, 1977, in Dist. Khulna, Bangladesh, to Monowara Begum and late Samsul Alam Chowdhury. He came to the United States in 2005 with a diversity visa lottery. He started his college education in 2006 at York College of the City University of New York in New York. He got married to Tasmiyah K. Ansari in 2009. In the following Year, by the grace of Almighty Allah, he had a baby boy, Izaan Chowdhury, with Tasmiyah. Azhad Chowdhury graduated from York College in 2011 majored in chemistry under the guidance of Dr. Jong I. Lee. Following Graduation, he moved to West Lafayette, Indiana, and joined the Simpson group at Purdue University, with research interests of instrument and method development toward the analysis of pharmaceutical formulations. In his spare time, he loves to spend time with his family.

PUBLICATIONS

JACS
JOURNAL OF THE AMERICAN CHEMICAL SOCIETY
Article
pubs.acs.org/JACS

Kinetic Trapping of Metastable Amino Acid Polymorphs

Azhad U. Chowdhury, Christopher M. Dettmar, Shane Z. Sullivan, Shijie Zhang, Kevin T. Jacobs, David J. Kissick, Thora Maltais, Hartmut G. Hedderich, Patricia A. Bishop, and Garth J. Simpson*

Department of Chemistry, Purdue University, 560 Oval Drive, West Lafayette, Indiana 47907, United States

Supporting Information

ABSTRACT: Second harmonic generation (SHG) microscopy measurements indicate that inkjet-printed racemic solutions of amino acids can produce nanocrystals trapped in metastable polymorph forms upon rapid solvent evaporation. Polymorphism impacts the composition, distribution, and physico-kinetic properties of organic solids, with energetic arguments favoring the most stable polymorph. In this study, unfavored noncentrosymmetric crystal forms were observed by SHG microscopy. Polarization-dependent SHG measurement and synchrotron X-ray microdiffraction analysis of individual printed drops are consistent with formation of homochiral crystal production. Fundamentally, these results provide evidence supporting the ubiquity of Ostwald's Rule of Stages, describing the hypothesized transitioning of crystals between metastable polymorphic forms in the early stages of crystal formation. Practically, the presence of homochiral metastable forms has implications on chiral resolution and on solid form preparations relying on rapid solvent evaporation.

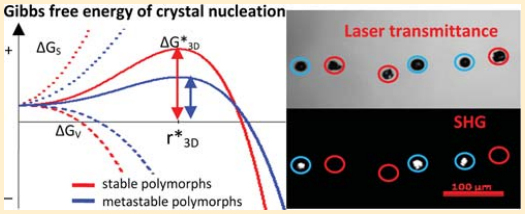

1. INTRODUCTION

The crystalline form of a solid can profoundly affect its physical and chemical properties, with both stable and metastable crystal polymorphs potentially accessible during crystal formation. In a few relatively rare cases, the time frame for polymorph transitioning can be long enough to enable detection of the metastable intermediates using conventional existing methods.[1−3] Perhaps the most famous example involves the case of ritonavir (Norvir).[4−6] Only when a more thermodynamically stable Form II polymorph of ritonavir first appeared in commercial Norvir gel caps was it realized that the initial form was metastable. The more stable Form II exhibited much slower dissolution kinetics, and the product had to be withdrawn from the market and reformulated.

Formation of metastable polymorphs can be interpreted thermodynamically according to the Ostwald−Lussac's Rule of Stages, which states that the form having the Gibbs free energy closest to the solvated molecules in the mother liquor will crystallize first,[1,7,8] followed by adiabatic transitions through increasingly more stable forms before ultimately arriving at the most stable crystal form.[3] However, this purely thermodynamic argument is based on an adiabatic limit. In practice, direct observation of such polymorph transitions are challenging given the rare and transient nature of crystal nucleation. More than a century after the original hypothesis by Ostwald, methods are now becoming available to systematically observe polymorphic transitions experimentally according to the Ostwald Rule of Stages at the individual building-block scale in a few model systems.[9−11] Studies of colloidal crystal nucleation have provided a route for increasing the size of the "molecule" to one large enough to observe by conventional optical microscopy.[3,9] Experiments of protein crystallization[12] and simulations of relatively simple model systems[11,13−16] also support a multistep process for crystallogenesis. The most compelling evidence for direct observation of rapid transitioning according to the Ostwald Rule of Stages in a system with directional bonding arguably comes from electron microscopy measurements of $LiFePO_4$ nanocrystals.[3] In this study Chung and co-workers observed at least four different polymorphic forms of the inorganic crystal sequentially at atomic resolution during high-temperature crystal formation. However, these atom/particle model systems generally consist of relatively simple highly symmetric building blocks with low barriers for interconversion between polymorphs and correspondingly facile polymorph transitioning. More complex molecules of low symmetry with greater conformational freedom generally can be expected to exhibit larger entropic barriers for interconversion. Consequently, studies working toward the broader goal of characterizing complex molecular species have been limited primarily by the difficulties in definitively isolating and characterizing the individual transient structures at low concentration and small sizes generated during the very earliest stages following crystal nucleogenesis.

According to classical nucleation theory, the rates of formation and growth of crystal nuclei arise from an interplay between surface free energy (ΔG_S) and bulk free energy (ΔG_B).[10,12,17,18] The critical cluster size for nucleation corresponds to the maximum in the total free energy surface, as shown in Figure 1. The polymorph with the lowest barrier for nucleation may not necessarily correspond to the most thermodynamically stable bulk form. The transition to the most

Received: October 7, 2013
Published: January 22, 2014

   dx.doi.org/10.1021/ja410293p | J. Am. Chem. Soc. 2014, 136, 2404−2412

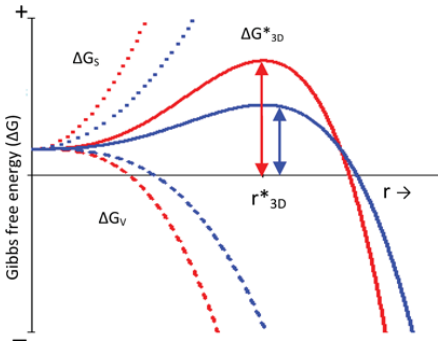

Figure 1. Change in Gibbs free energy change (ΔG) as a function of the radius of the cluster. Solid lines are the net free energy change of a cluster as a function of radius. Surface (dotted) and bulk (dashed) free energy represent the positive and negative contributions to the total energy. Critical radii (r^*_{3D}) and the corresponding (ΔG^*_{3D}) for two different polymorphs correspond to the maxima in the solid traces.

stable form can arise from two mechanisms. First, the relatively unstable polymorph can spontaneously convert to the alternative form, which requires another solid-state nucleation event. Second, the presence of crystallites of the stable polymorphic form elsewhere within the mother liquor can grow at the expense of the metastable forms through Ostwald ripening. In either case evidence of these polymorphic transformations is difficult to obtain as crystal nucleation is intrinsically a rare event and polymorphic changes upon nucleation are generally expected to be short lived.

The conditions most likely to result in long-lived metastable polymorph generation correspond to small, confined volumes and rapid desolvation to reduce the possibility of ripening or interconversion. Inkjet printing, which deposits picoliter dots of solutions on substrates, is well matched to these requirements. In addition, inkjet printing can serve as a model for other deposition techniques involving rapid solvent evaporation, including spray drying, which is used routinely in the preparation of high surface area APIs.[19]

In the current study, piezoelectric inkjet printing was employed to produce metastable polymorphs of proline and second harmonic generation (SHG) microscopy used as a probe for identifying noncentrosymmetric (metastable) crystal domain formation. Two algorithm approaches, principal component analysis (PCA) and autocorrelation, have been used on the polarization-dependent SHG images and X-ray diffraction images of inkjet-printed dots to verify the presence of kinetically trapped metastable polymorphs of proline upon rapid crystallization from racemic solutions. The majority of the amino acids, including both proline and serine, produce centrosymmetric racemic cocrystals when crystallized from racemic aqueous solutions.[20−22] Consequently, any noncentrosymmetric crystal forms prepared from such solutions would necessarily be metastable. However, crystal polymorphism studies using conventional methods (e.g., diffraction, Raman, infrared spectroscopy, NMR, calorimetry, etc.) typically do not have the sensitivity to selectively identify small quantities of the rare, unfavored polymorphs in mixtures.[23]

Second-harmonic generation can be used as a contrast mechanism, as it is highly selective for noncentrosymmetric submicrometer-sized noncentrosymmetric (i.e., chiral) crystals[23] and produces no coherent SHG signal from liquids (even from a noncentrosymmetric solution), gases, and amorphous solids.[20,23−26] Crystals grown from a racemic proline solution are expected to be centrosymmetric, racemic cocrystals[22] and should not produce any SHG signal. However, the presence of detectable SHG signal from inkjet-printed microcrystals can serve as a simple indicator of the presence or absence of metastable polymorphic forms. Polarization-resolved SHG microscopy can further enhance the information content of SHG measurements,[27,28] given the sensitivity of the polarization dependence of SHG to crystal form and orientation. SHG can also be used to rapidly identify regions of interest for X-ray diffraction analysis, which in turn can be used to characterize polymorphism.[28−30] Here, we demonstrate the use of autocorrelation analysis of scattering patterns to recover high signal-to-noise XRD "powder patterns" from picograms to femtograms of material produced by piezoelectric inkjet printing and use this approach for structural analysis of the metastable forms.

2. METHODS

D-Proline and L-proline, assay ≥ 99%, were purchased from Sigma-Aldrich and used without any further purification. Homochiral solutions (0.7 M) of each were made in deionized water, and racemic solution was prepared by obtaining an equal volume of each. In order to produce thermodynamically controlled racemic proline crystals, the racemic solution was kept on the hot plate with gentle heat for 30 min to prepare a supersaturated solution and then cooled to room temperature and kept in a fume hood overnight for spontaneous crystallization. Fine white crystals were formed. Racemic mixtures of dry proline crystals were prepared by crushing equal parts of the two homochiral proline powders in a mortar and pestle.

Homochiral and racemic proline solutions were printed on hydrophobic glass coverslips and on MiTeGen UV−vis 100 μm MicroTip by a Fujifilm Dimatix Material printer DMP 2800. Proline solutions were printed in dot matrix arrays with 80 μm periodicity between spots and 120 μm periodicity between rows, respectively (10 × 10 array). A standard monopolar waveform with an average jetting voltage of 33 V and nozzle temperature of 48 °C were used to print the arrays. Deposited volumes of <8 and <2 fL were estimated from the residual solid on the substrate in the array dots from homochiral and racemic solutions. The average printing time of each pattern was ∼10−12 s.

A built-in-house beam-scanning SHG microscope was used to acquire images. Beam scanning was performed with a resonant vibrating mirror (∼8 kHz, EOPC) along the fast-axis scan and a galvanometer (Cambridge) for slow-axis scanning. The 80 MHz Ti:sapphire pulsed laser (Spectra-Physics Mai Tai) of 100 fs pulse width directed through the scan mirrors and focused onto the sample using a 10× objective of working distance 1.6 cm (Nikon, N.A. = 0.30). Under typical operating conditions, the incident wavelength was 800 nm, with 80 mW laser power recorded before the objective. In order to reduce 1/f noise in the polarization-dependent measurements, a custom electro-optical modulator (EOM, Conoptics) was positioned in the beam path, enabling high-frequency (16 MHz) modulation of the polarization state of the beam. The laser repetition rate was doubled by an orthogonal pulse pair generator, in which the primary beam was split and recombined following a 6.25 ns delay to produce an interleaved pulse train of orthogonal polarizations prior to the EOM.[31] Synchronous digitization of each laser pulse with strict timing control was used to identify the polarization dependence of each incident laser shot.[32] Polarized transmission SHG signals were collected, with dichroic mirrors and narrow band-pass filters (Chroma HQ400/20 m-2p) centered around 400 nm placed prior to the photomultiplier tube detectors (Burke, XP 2920PC). Matlab code was written in-house to control the scanning mirrors and communication with the data acquisition electronics. Concurrently with the transmission SHG detection, bright-field images were acquired by

dx.doi.org/10.1021/ja410293p | J. Am. Chem. Soc. 2014, 136, 2404−2412

measuring the extinction of the 800 nm beam using a photodiode, also acquired in transmission. Bright-field and SHG images were rendered and analyzed with Image J to produce a set of 10 unique polarization-dependent images per detector, and "analyze particles" options were used to measure the area of each dot in bright field as well as SHG active regions.[33]

X-ray microdiffraction measurements were acquired at GM/CA beamline 23-ID-B with a 10 μm diameter, 12.0 keV X-ray beam with 1 s exposure time, at a photon flux of 1.3×10^{10} photons s^{-1} (5-fold attenuation) and detector distance of 150 mm, at the Advanced Photon Source within Argonne National Laboratory.[28−30] An SHG microscope built into the beamline and described previously was used to discriminate between the SHG-active and -inactive dots in inkjet-printed arrays and position them within a collimated 10 μm diameter X-ray beam.[30] Diffraction patterns were collected from both SHG-active and -inactive dots of racemic proline and from pure L-proline dot.

Analysis of the X-ray scattering images was performed by autocorrelation over the azimuthal rotation angle for peak detection in order to suppress diffuse scatter and improve the S/N of the diffraction measurements. In brief, scattering images were transformed into polar coordinates by use of python image processing,[34] followed by autocorrelation along the φ axis which was performed by the Wiener-Kmintchine method.[35,36] The differences between the asymptotic mean of the azimuthal autocorrelogram and the mean of the autocorrelogram over steps of 1−4 pixels were plotted as a function of the radial 2θ angle. This algorithm served to retain sharp features in the scattering pattern consistent with diffraction while suppressing rolling features from diffuse scattering arising from amorphous materials or through inelastic scattering events. For comparative purposes, conventional powder XRD scattering patterns were also produced simply by integration over all the azimuthal angles and all regions probed by the X-ray beam.

For the polarization-dependent studies, principal component analysis (PCA) was performed on 10 different input and output SHG polarization combinations using R v.2.15 with the built-in PCA function (princomp).[28,37] Each pixel in the SHG images was treated as a "hyperspectral" vector in a 10-dimensional polarization space.[27] PCA separates the data into the eigenvectors or principal components that maximize the total variance in the data set, the first few of which provide the greatest separation within the polarization-dependent dimensions.

3. RESULTS AND DISCUSSION

Laser transmittance and SHG images of racemic proline crystals produced by solvent evaporation from racemic solutions and physical mixtures (1:1 mass ratio) of two homochiral powder are presented in Figure 2. The crystals of homochiral proline from aqueous solution adopt a $P2_12_12_1$ space group as the thermodynamically favored form,[38] which is SHG active. A physical mixture of the two homochiral crystalline materials prepared by grinding produced an ensemble that was racemic overall but still primarily comprised of homochiral crystalline domains. SHG imaging of these materials produced a strong signal. The disparity between the bright regions in the SHG image and the optical transmittance images suggests that scattering losses in the optically opaque regions attenuated the SHG response, either through scattering of the fundamental and the corresponding reduction of SHG or through the scattering of the coherent SHG to angles outside the acceptance cone of the collection objective. Alternatively, the darker regions could correspond to domains in which the racemic solid dispersion has undergone phase transformation to either an amorphous material or the racemic cocrystal.[39] The racemic proline cocrystal produced upon crystallization of proline from a racemic solution adopts a $P2_1/c$ space group[22] with a centrosymmetric lattice, which is forbidden by symmetry

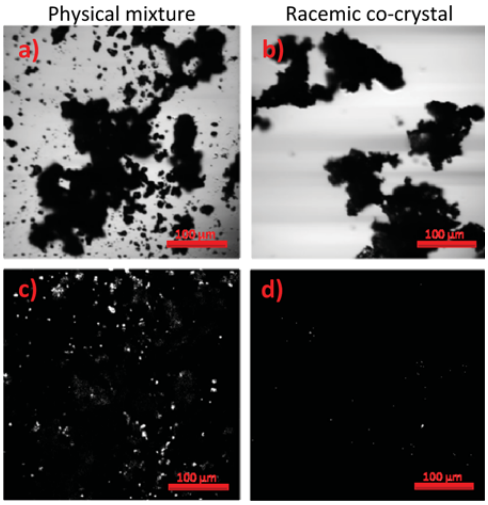

Figure 2. Bright-field images of laser transmittance (top row) and SHG images (bottom row) of racemic proline, obtained from two different conditions. The physical mixture (a and c) was made by grinding equal amounts of D- and L-proline in a mortar and pestle. Overnight crystallization of a saturated racemic proline solution produces white racemic cocrystals (b and d), which was also crushed in a mortar and pestle for imaging. Racemic crystals did not produce any detectable SHG signals.

from producing SHG.[24,26] Combining the results from all of the considered cases, the SHG activity was >50-fold in the physical mixture of homochiral crystals than in the powders produced upon crystallization from a racemic solution.

Inkjet-printing racemic proline solutions on hydrophobic glass slides produced markedly different results. Figure 3a and

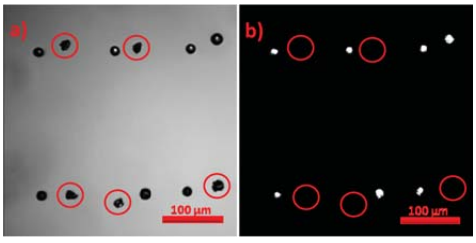

Figure 3. Bright-field (a) and SHG (b) images of dot matrix-printed racemic solution. There are 12 dots of racemic proline in the field of view. Seven of them formed a round-shaped dot, while the remaining five formed jagged shapes. Only the round-shaped dot generated substantial amounts of SHG.

3b are bright-field and SHG images of inkjet-printed racemic proline solution, respectively. Seven out of 12 printed dots produced SHG signal, while the other five did not (red circles in Figure 3b) show any SHG activity. Similar SHG activity was observed from multiple dot arrays (not shown) with >60% of printed racemic dots exhibiting SHG activity. The average SHG photon counts of 45 ± 6 from racemic dots were comparable to the average SHG counts of 45 ± 5 from $BaTiO_3$ nanocrystals (200 nm) in polyethylene glycol (PEG) from the same laser power. SHG signals (Figure 3b) coincide qualitatively with

locations of laser extinction (Figure 3a), although extinction arose over quantitatively larger areas. From the SHG intensity measurements (presented in Table 1), 82 ± 2% of the area within the homochiral dot was SHG active, compared to just 58 ± 2% in the racemic dot exhibiting SHG activity.

Table 1. Statistical Details of Bright-Field and SHG Images of Inkjet-Printed Dot Matrices of Proline Solution (uncertainties correspond to 95% confidence intervals)

proline	average area in bright field (pixels)	SHG active area (pixels)	SHG active area (%)	avg SHG intensity (counts)
D-proline	375 ± 3	310 ± 3	83 ± 1	9 ± 2
L-proline	336 ± 4	270 ± 4	80 ± 2	6 ± 2
racemic proline	235 ± 4	137 ± 4	58 ± 2	45 ± 6

Several possible origins of the observed SHG activity upon inkjet printing were considered. SHG is well known to arise at interfaces between centrosymmetric media from local symmetry breaking.[24,26] In heterogeneous dots, multiple interfaces between amorphous and/or crystalline domains may be present, contributing to interfacial SHG. The anticipated magnitude of the interfacial response can be estimated based on the relative number of bulk versus interfacial molecules producing signal. Assuming a ∼1 μm^2 beam waist and a similarly sized crystal, the number of interfacial molecules is roughly 10^4-fold lower than the number of bulk molecules within a crystalline lattice (assuming a ∼10 Å lattice constant). Given the quadratic scaling of SHG with number density, this difference corresponds to a ∼10^8-fold difference in anticipated SHG from the interface of a centrosymmetric or amorphous media versus a noncentrosymmetric crystalline lattice. The observation of SHG activity comparable in brightness to the highly SHG-active $BaTiO_3$ nanoparticles suggests formation of bulk-allowed noncentrosymmetric crystal domains within the dot and not SHG arising from interfaces. In addition, SHG from impurities in the racemic solutions is unlikely to serve as a major source of background, as those same solutions were used to prepare the SHG-inactive samples by slow drying. Therefore, the SHG activity from inkjet printing of the racemic solutions was attributed to noncentrosymmetric crystal formation.

Inkjet-printed homochiral proline samples were also studied, prepared from the same stock solutions used to produce the racemic solutions, producing representative SHG micrographs shown in Figure 4. The top row are laser transmittance images, and the bottom row are SHG images of inkjet-printed homochiral (D and L) proline. The average areas of the homochiral dots were larger than the racemic dots, possibly attributed to a lower surface tension, higher contact angle, and more spherical initial droplet of a homochiral proline solution compared to that of the racemic solution. Secondary dot formation adjacent to the main drop, known as satellites, was observed from nonuniform ejection of the ink dot from the cartridge from nonideal matching of the ink to the jetting waveform, incorrect voltages, or high surface tension. No surfactant was used in these studies, which introduced additional challenges in control proper drop formation. The observation of clearly detectable SHG activity from each dot (Figure 4c and 4d) is consistent with formation of the known thermodynamically favored and SHG-active $P2_12_12_1$ space group[38,40] adopted by homochiral proline upon crystallization from aqueous solution.

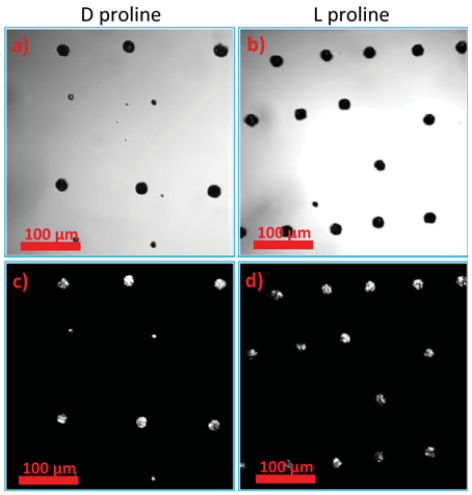

Figure 4. Bright-field (a and b) and SHG image of inkjet-printed D- and L-proline (c and d) are shown for comparing the bright-field and SHG images; all dots in the field of view are SHG active.

The disparities between the total printed areas of the dot and the fraction of them that exhibited SHG activity suggest that a significant amorphous content remained following printing. For the dot prepared from homochiral solutions, all published polymorphs of proline identified by the authors fall into space groups that are allowed for SHG.[38,41] Therefore, it is reasonable to assign the SHG-inactive area to regions containing either amorphous proline or nanocrystalline proline with crystal sizes falling below the detection limits of SHG (i.e., SHG amorphous). In the racemic dot, the SHG-inactive domains could correspond to either amorphous proline or SHG-inactive racemic cocrystals. If it is assumed that 20% of the area corresponds to amorphous material as in the homochiral dot, then the inactive co-crystal may potentially occupy 22% area of the remaining 80% area. However, this SHG-inactive fraction represents the minor constituent within the dot, rather than the major. Both the cross-sectional area of the dot exhibiting SHG activity and the integrated brightness of the racemic dot (the SHG active racemic crystals were 2−3 times brighter than crystals in either homochiral dot) suggest that the majority of the printed volume corresponds to an SHG-active metastable polymorphic form.

In order to confirm that the SHG-active domains were indeed from metastable crystal forms, SHG-active inkjet-printed dots prepared from racemic solutions were rehydrated by extended exposure to 100% relative humidity and reanalyzed (Supporting Information). The rehydrated dots exhibited SHG activities that were reduced 5-fold (18%) compared to the initially prepared dots after 24 h in 100% relative humidity, which is consistent with interconversion to more stable crystal forms.

While the simple SHG intensity measurements summarized in Figures 3 and 4 indicate the presence of SHG-active crystals produced from the racemic solution, the SHG intensity alone provides little meaningful information on the forms of the crystals produced. The observation of SHG activity could potentially be arising from either homochiral crystallization, from generation of noncentrosymmetric racemic cocrystals with

dx.doi.org/10.1021/ja410293p | J. Am. Chem. Soc. 2014, 136, 2404−2412

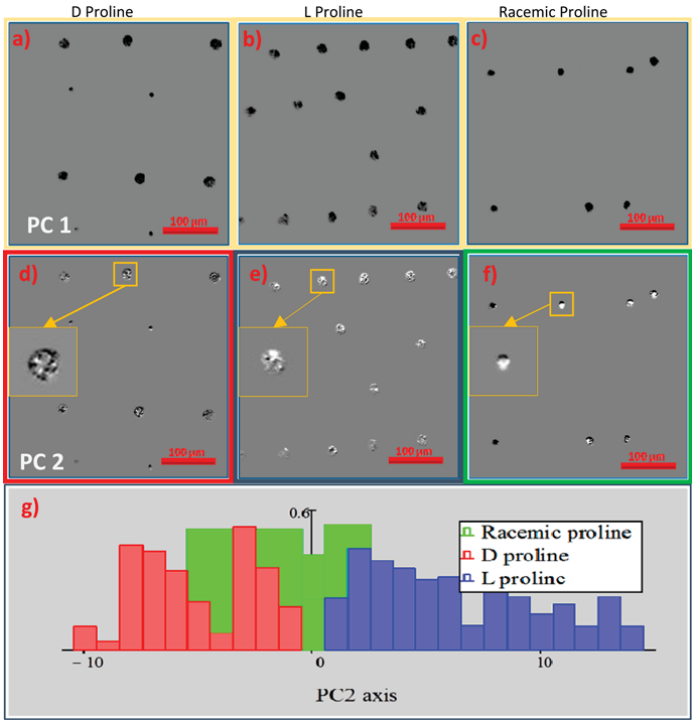

Figure 5. (a–c and d–f) Images of the first two principle components of proline. (g) Histogram of all SHG active D-proline, L-proline, and racemic proline crystals. PC1 corresponds mostly to overall signal intensity, and PC2 corresponds mostly to the polarization-dependent SHG response. D and L crystals give similar overall intensity and were separable only in their polarization-dependent response. Racemic proline had a less characteristic polarization-dependent response but was characteristically brighter than D and L crystals.

both enantiomers present within the lattice, or some combination of the two.

Polarization-dependent SHG measurements were acquired and interpreted using principal component analysis (PCA) to aid in assessing the crystal forms produced upon inkjet printing the racemic solutions. A set of 10 polarization-dependent micrographs was used to define a 10-dimensional "polarization space", with PCA used to reduce the majority of the relevant polarization-dependent information to a few key principal components containing the majority of the intrinsic information content in the polarization-dependent data set. PCA results from the 10 different polarization combination images of inkjet-printed racemic proline solution and a histogram of all the dot are presented in Figure 5. Together, PC1 and PC2 contain 96% of the total signal variance. The first principal component, PC1, was dominated by differences in overall intensity as a function of location.[28,42,43] Therefore, PC2 carried the majority of the polarization dependence of the measurements. This interpretation is also consistent with previous work designed to detect different crystal domains by SHG imaging demonstrating that PC2 carries the majority of the polarization-dependent information.[28] Figure 5g is the histogram of PC2 values averaged within each dot.

Interestingly, the histogram of PC2 values indicates reasonable separation between D- and L-proline by polarization-dependent SHG microscopy. This result is somewhat surprising given that SHG is not predicted to enable discrimination between the two enantiomers from an isotropic population of crystal orientations (analogous to hyper-Rayleigh scattering). The ability to resolve the two therefore suggests preferred crystal orientation (e.g., from heterogeneous templating by the solid interface). It is even more remarkable that the influence of absolute chirality appears to provide a greater inherent variance in the SHG measurements than changes related to the random population of azimuthal orientations of the crystals. Both effects can be seen by inspection of the PC2 images in Figure 5, in which the PC2 values varied significantly within the individual dot (attributed to a population of oriented crystals), but integration over the dots nevertheless produced overall darker spots for the D-proline and vice versa for the L-proline.

Dot arrays prepared from printing the racemic solution produced PC2 values intermediate between the two homochiral crystal results. These observations are consistent with formation of a population of homochiral crystals within the dot generated from printing the racemic solution. However, several alternative possibilities were also considered. First, the SHG activity could be emerging from a noncentrosymmetric polymorph that still includes both enantiomers within the unit cell. No such forms are known for proline but could still be formed under kinetic control. It would be coincidental for the polarization dependence of such a form to lie between the two homochiral poles in

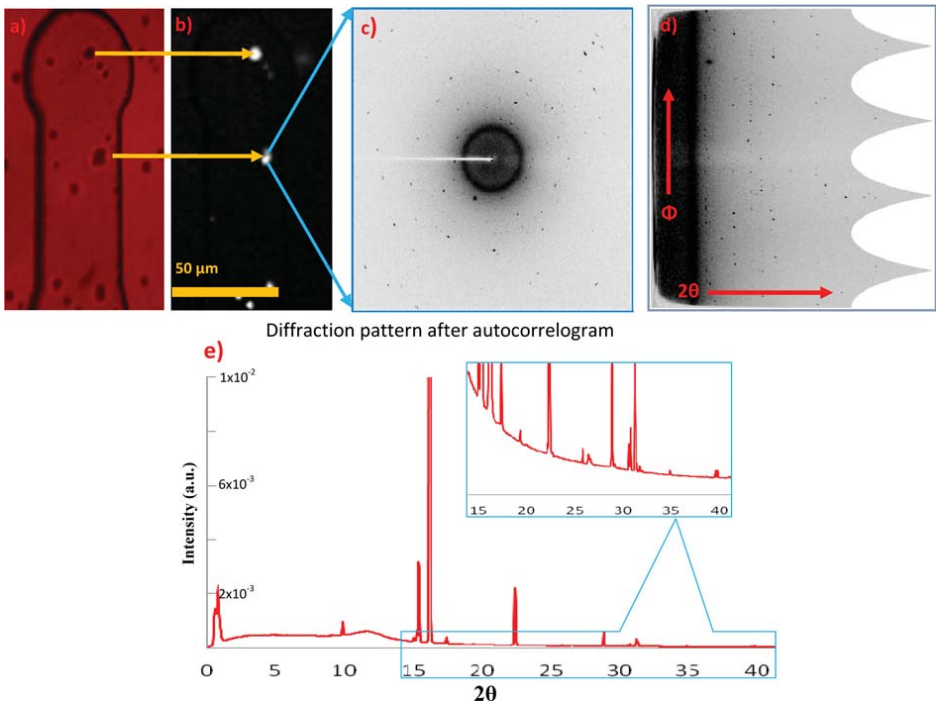

Figure 6. (a and b) Laser bright-field and SHG images of inkjet-printed L-proline on a microtip, respectively. White spots in b are the SHG active inkjet-printed drops. (c) X-ray diffraction image of a single 10 × 10 μm spot obtained from the center of the corresponding SHG active droplet. Dark spots in this diffraction image correspond to high signal-to-noise diffraction peaks arising from the crystal. (d) Diffraction image remapped into polar coordinates, in which ϕ is the azimuthal rotation angle and 2θ is the proportional to the distance from the image center, corresponding to the location of the undiffracted beam. The powder-like pattern shown in e was produced by autocorrelation along the azimuthal direction to select for sharp diffraction spots, followed by integration over the baseline-subtracted autocorrelogram. High signal-to-noise of the diffracted peak is shown in the inset.

the histogram within Figure 5, but the possibility cannot be definitively excluded based solely on the SHG measurements.

X-ray microdiffraction measurements using synchrotron radiation were also performed to characterize the structures produced upon inkjet printing of proline solutions (Figure 6). Figure 6a and 6b shows the bright-field and SHG images of L-proline printed onto an X-ray microtip, respectively. Using a microfocused beam only 10 μm in diameter to reduce background scatter, diffraction analysis could be performed on each individual printed dot. A representative scattering pattern is shown in Figure 6c. The small probed volume and even smaller crystal sizes associated with the diffraction measurements placed them between the two extreme limits of single-crystal diffraction and powder X-ray diffraction (PXRD), in which a statistical population of crystal sizes and orientations are probed. The conditions of the current experiments preclude the ability to obtain large single crystals from inkjet-printed drops; however, they also do not produce enough microcrystals to approximate all possible crystal orientations. Consequently, an autocorrelation-based approach was developed to recover a powder-like pattern from the spots present in the scattering image, illustrated in Figure 6. First, the scattering image was transformed from Cartesian coordinates to radial coordinates, after first performing calibration to place the center of the undiffracted beam within one pixel of the center of the 4096 × 4096 element X-ray detection array. Following this transformation, the diffuse rings circling the beam stop in the initial image appear as vertical swaths in radial coordinates. Next, autocorrelation was performed along the azimuthal axis (vertical axis in Figure 6d). From the autocorrelogram at each radial 2θ distance, integration was performed over the short-lived features (1−4 pixels) corresponding to spots in the original scattering image, followed by subtraction of the asymptotic baseline arising from the diffuse scattering background. Autocorrelation provides no discrimination based on absolute azimuthal position, recovering a one-dimensional diffraction pattern analogous to what one might obtain by powder XRD (Figure 6e). Similar analyses were performed on several printed dots of the racemic solution (both SHG active and SHG inactive) as well as a printed dot of homochiral L-proline.

Even with the autocorrelation analysis, the small volumes within each printed dot did not allow for statistical sampling of crystal orientations, complicating quantitative determination of crystal form directly from the relative intensities of the diffracted peaks. Therefore, the positions of peaks with S/N > 100 were used as the primary factor for structural assignment. A comparison of these peak intensities is presented in Figure 7.

dx.doi.org/10.1021/ja410293p | J. Am. Chem. Soc. 2014, 136, 2404−2412

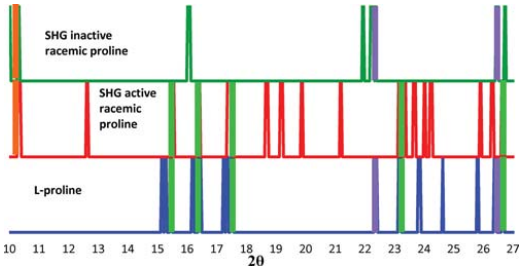

Figure 7. Comparison of the XRD peak positions for a racemic dot exhibiting no SHG activity (top row), racemic dots that were bright for SHG (middle row), and a SHG-active dot of L-proline. Peaks correspond to locations of diffraction exhibiting S/N > 100. Intensities were omitted as orientational affects make these nontrivial to compare. Purple shading indicates regions where L-proline peaks match the SHG inactive racemate spots, green highlights where L-proline and the SHG active racemate spots match, and orange highlights where the two racemates share peaks missing from the L-proline samples.

The integrated intensities under these similar diffraction peaks were calculated along with total area under each peak in between 10° and 28° diffraction angles. Results indicate that 64% of the integrated peak intensity from SHG-active racemic dot corresponded to 2θ locations also present for L-proline, while only 5% of the area under the peak is present for SHG-silent racemic proline. These results further support the polarization-dependent SHG analyses, suggesting that the homochiral metastable crystal polymorph forms upon rapid inkjet printing from an aqueous solution.

Interestingly, about one-third of the diffracted intensity within the SHG-active racemic dot did not overlap with diffraction peaks observed in either the homochiral dot or the racemic SHG-inactive dot. This disparity could arise from undersampling of the homochiral dot, such that not all 2θ diffraction locations were adequately sampled within the limited number of dots analyzed. Alternatively, additional crystal forms may be present that do not correspond to constituents of either of the other two sets of dots (i.e., homochiral and racemic SHG inactive). Nevertheless, it appears that the homochiral metastable crystals comprise the majority composition of the racemic SHG-active dots based on X-ray microdiffraction analysis. Consequently, the SHG-active domains are attributed to homochiral crystalline domains, with an equal probability of forming from the D- or L-enantiomers on a single nanocrystal basis.

In addition to the SHG and XRD analyses, confocal Raman measurements within individual inkjet-printed dots were acquired by signal integration for 1.5 h in a single inkjet confocal volume positioned within the printed dots and compared with Raman spectra of the pure powders generated with 10 s integration times (summarized in the Supporting Information). For dots printed from the homochiral solutions, spectral features qualitatively similar to those observed from the racemic powder were observed. However, interpretation of the spectra was complicated by preferred orientation effects, as the relative intensities of the different Raman features are markedly different for the inkjet-printed proline versus the powder spectra. Attempts were made to obtain confocal Raman spectra of the SHG-active dots produced from racemic solutions, but no sharp spectral features consistent with crystalline lysine were observable, prohibiting meaningful assessment of crystal polymorphism by Raman. The absence of detectable Raman is attributed to the relatively weak Raman cross-section of proline, the trace quantities of crystalline material present, and the relatively high detection limits of Raman microscopy compared to both SHG and the minibeam synchrotron XRD method developed in this work. The S/N of the most prominent Raman peak was 16 after 1.5 h of signal averaging, compared to a S/N of >3000 from the synchrotron XRD measurements for a 1 s XRD integration time per pixel and 250 μs per pixel integration time for SHG.

The phase diagram of proline provides a framework for describing the thermodynamic driving factors underpinning crystallization (Figure 8). Klussmann, Blackmond, and co-

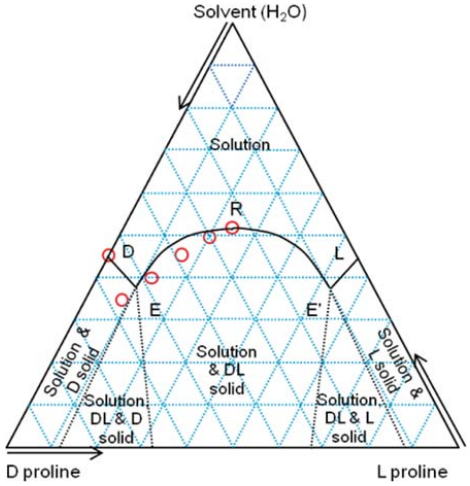

Figure 8. Ternary phase diagram of D-proline, L-proline, and H_2O at 25 °C. Experimental data points (red circles) are plotted in this triplot according to their mass percentage, and it is assumed that the data points are symmetric about the vertical axis. Solid lines connecting points DER and RE′L represent the saturated solution, and E, E′ are the eutectic composition. The eutectic mass percentage was found to be 74%, calculated from the solubility of homochiral and racemic proline.

workers presented a framework for predicting the anticipated eutectic points from combined solubility measurements of the enantiopure homochiral form and the racemic cocrystal.[44−46] Using this model, the solid lines for the phase boundaries were calculated using just the solubilities of the racemic and homochiral solutions. In the case of proline crystallizing from an aqueous solution, the solubilities of the two crystal forms are similar, with a solubility ratio of $\alpha = [\text{racemic}]_{sat}/[\text{enantiopure}]_{sat} = 0.78$, resulting in an anticipated eutectic point corresponding to a 0.89 mol fraction of pure enantiomer (or equivalently, and enantiomeric excess of 0.74). These results are in good qualitative agreement with previous studies of the crystallization of proline from hydrophobic solvents ($CHCl_3$ and $CHCl_3$/MeOH mixtures), in which the racemic form was found to exhibit substantially lower solubility than the enantiopure form and indicating a strong preference for formation of the racemic cocrystal.[44,46] However, the measured phase diagram in Figure 8 is in better qualitative agreement with the previous crystallizations in DMSO yielding a solubility

ratio closer to 1. Quantitatively the solubility ratio in DMSO was reported to be $\alpha = 1.155$,[44] while the measurements presented here indicate $\alpha = 0.78$ in H_2O. Overall, the slightly lower solubility of the racemic form suggests that both crystal forms are energetically accessible under the conditions of the experiment, but the racemic cocrystal is clearly the thermodynamically favored crystal produced from a racemic solution. Therefore, observation of SHG-active forms emerging from a racemic solution indicates that crystallization is proceeding under kinetic control.

The presence of transient SHG-active polymorphic forms can be understood qualitatively from classical nucleation theory. Homogeneous crystal nucleation is driven by the interplay between an interfacial free energy cost and a volume free energy gain under conditions of supersaturation (Figure 1). Polymorphic forms with different interfacial free energy costs and volume gains have the potential to exhibit lower barriers for initial nucleation.[8,17] Under adiabatic conditions, curve crossing between different polymorphic forms can arise to ultimately favor growth of the most thermodynamically stable crystal form. However, curve crossing may be avoided under nonadiabatic conditions of rapid solvent evaporation, promoting continued growth of kinetically trapped metastable polymorphs. If the SHG-active polymorphs are comprised of homochiral crystalline domains, transitioning to the more stable racemic cocrystal would require significant changes in the fundamental composition of the lattice, which may explain the presence of a relatively large kinetic barrier to interconversion.

4. CONCLUSION

The rapid drying of inkjet-printed dots of racemic proline solutions on substrates produce SHG-active domains. These domains were attributed to the presence of metastable polymorphic forms kinetically trapped during rapid solvent desolvation, which supports Ostwald's conjecture of polymorph transitioning during crystallogenesis. Given the ubiquity of inkjet printing and the related approach of spray drying as a preparative method for pharmaceutical ingredients combined with the impact of crystal polymorphism on bioavailability, these findings may help guide future API formulation strategies that involve inkjet printing and spray drying.

For example, the possibility of a kinetic route to enable homochiral resolution has potential implications in pharmaceutical syntheses and preparation of final dosage forms. While crystallization is arguably the most energy-efficient means of resolving homochiral compounds from an enantiomeric mixture, the process is only currently viable in the absence of resolving agents (e.g., chiral salts) under conditions in which the homochiral polymorph is the thermodynamically most stable form. Unfortunately, homochiral crystallization is often found to be the exception rather than the rule, with most compounds favoring racemic cocrystal production as in proline. However, if the emerging crystal form can be placed under kinetic control rather than thermodynamic control, a host of new possible options and architectures emerge for efficient chiral resolution through crystallization. SHG imaging may help enable such developments by rapidly identifying and optimizing potentially promising conditions.

■ ASSOCIATED CONTENT

Supporting Information

SHG micrographs of racemic dots prior to and following extended exposure in a 100% relative humidity environment; confocal Raman spectra for inkjet-printed dots and pure powders. This material is available free of charge via the Internet at http://pubs.acs.org.

■ AUTHOR INFORMATION

Corresponding Author

gsimpson@purdue.edu

Notes

The authors declare no competing financial interest.

■ ACKNOWLEDGMENTS

The authors gratefully acknowledge Dr. Alexander Wei for his help with the inkjet printing and Dr. Duangporn Wanapun for her contributions in the instrumental and experimental design. Support was provided by the National Institutes of Health, Award Nos. NIH-R01GM103401 and NIH-R01GM103910, the National Institute for Pharmaceutical Technology and Education (NIPTE), Award No. NIPTE-106361, and support for algorithm development and integrated XRD & SHG instrumentation by the Center for Direct Catalytic Conversion of Biomass to Biofuels (C3Bio), an Energy Frontier Research Center funded by the U.S. Department of Energy, Office of Science, Office of Basic Energy Sciences, Award No. DE-SC0000997.

■ REFERENCES

(1) Nývlt, J. *Cryst. Res. Technol.* **1995**, *30*, 443−449.
(2) Hamilton, B. D.; Hillmyer, M. A.; Ward, M. D. *Cryst. Growth Des.* **2008**, *8*, 3368−3375.
(3) Chung, S.-Y.; Kim, Y.-M.; Kim, J.-G.; Kim, Y.-J. *Nat. Phys.* **2008**, *5*, 68−73.
(4) Chemburkar, S. R.; Bauer, J.; Deming, K.; Spiwek, H.; Patel, K.; Morris, J.; Henry, R.; Spanton, S.; Dziki, W.; Porter, W.; Quick, J.; Bauer, P.; Donaubauer, J.; Narayanan, B. A.; Soldani, M.; Riley, D.; McFarland, K. *Org. Process Res. Dev.* **2000**, *4*, 413−417.
(5) Morissette, S. L.; Soukasene, S.; Levinson, D.; Cima, M. J.; Almarsson, O. *Natl. Acad. Sci. U.S.A.* **2003**, *100*, 2180−2184.
(6) Bauer, J.; Spanton, S.; Henry, R.; Quick, J.; Dziki, W.; Porter, W.; Morris, J. *Pharm. Res.* **2001**, *18*, 859−866.
(7) Terry, T. *Org. Process Res. Dev.* **2003**, *7*, 1017−1027.
(8) Wilhelm, O. *Z. Phys. Chem.* **1897**, *22*, 289−330.
(9) Gasser, U.; Weeks, E. R.; Schofield, A.; Pusey, P. N.; Weitz, D. A. *Science* **2001**, *292*, 258−262.
(10) Zhang, T. H.; Liu, X. Y. *Angew. Chem., Int. Ed. Engl.* **2009**, *48*, 1308−1312.
(11) Chakraborty, D.; Patey, G. N. *J. Phys. Chem. Lett.* **2013**, *4*, 573−578.
(12) Vekilov, P. G. *J. Cryst. Growth* **2005**, *275*, 65−76.
(13) Anwar, J.; Boateng, P. K. *J. Am. Chem. Soc.* **1998**, *120*, 9600−9604.
(14) Anwar, J.; Zahn, D. *Angew. Chem., Int. Ed. Engl.* **2011**, *50*, 1996−2013.
(15) Lutsko, J.; Nicolis, G. *Phys. Rev. Lett.* **2006**, *96*, 046102.
(16) Mucha, M.; Jungwirth, P. *J. Phys. Chem. B* **2003**, *107*, 8271−8274.
(17) Erdemir, D.; Lee, A. Y.; Myerson, A. S. *Acc. Chem. Res.* **2009**, *42*, 621−629.
(18) Vekilov, P. G. *Cryst. Growth Des.* **2010**, *10*, 5007−5019.
(19) Basaran, O. a.; Gao, H.; Bhat, P. P. *Annu. Rev. Fluid Mech.* **2013**, *45*, 85−113.
(20) Hall, V. J.; Simpson, G. J. *J. Am. Chem. Soc.* **2010**, *132*, 13598−13599.
(21) Jean, J., André Collet, S. H. W. *Enantiomers, Racemates, and Resolutions*; Wiley: New York, 1981.
(22) Myung, S.; Pink, M.; Baik, M. H.; Clemmer, D. E. *Acta Crystallogr., Sect. C* **2005**, *61*, o506−8.

(23) Wanapun, D.; Kestur, U. S.; Kissick, D. J.; Simpson, G. J.; Taylor, L. S. *Anal. Chem.* **2010**, *82*, 5425−5432.
(24) Boyd, R. W. *Nonlinear Optics*, 3rd ed.; Academic Press: Rocheste, NY, 2008; pp 2−4.
(25) Knight, P. L. *Opt. Acta Int. J. Opt.* **1985**, *32*, 1−2.
(26) Stegeman, G. I.; Stegeman, R. A. *Nonlinear Optics: Phenomena, Materials and Devices*; John Wiley & Sons: NJ, 2012.
(27) Begue, N. J.; Simpson, G. J. *Anal. Chem.* **2010**, *82*, 559−566.
(28) DeWalt, E. L.; Begue, V. J.; Ronau, J. a; Sullivan, S. Z.; Das, C.; Simpson, G. J. *Acta Crystallogr., Sect. D: Biol. Crystallogr.* **2013**, *69*, 74−81.
(29) Kissick, D. J.; Dettmar, C. M.; Becker, M.; Mulichak, A. M.; Cherezov, V.; Ginell, S. L.; Battaile, K. P.; Keefe, L. J.; Fischetti, R. F.; Simpson, G. J. *Acta Crystallogr., Sect. D: Biol. Crystallogr.* **2013**, *69*, 843−851.
(30) Madden, J. T.; Toth, S. J.; Dettmar, C. M.; Newman, J. A; Oglesbee, R. A; Hedderich, H. G.; Everly, R. M.; Becker, M.; Ronau, J. A; Buchanan, S. K.; Cherezov, V.; Morrow, M. E.; Xu, S.; Ferguson, D.; Makarov, O.; Das, C.; Fischetti, R.; Simpson, G. J. *J. Synchrotron Radiat.* **2013**, *20*, 531−540.
(31) Jr, S. E. *J. Light Technol.* **1992**, *10*, 28−35.
(32) Muir, R. D.; Sullivan, S. Z.; Oglesbee, R.; Simpson, G. J. *Rev. Sci. Instrum.***2013**, accepted for publication.
(33) Abramoff, M. D.; Magalhaes, P. J.; Ram, S. J. *Biophotonics Int.* **2004**, *11*, 36−42.
(34) Klington, J. python image information along a polar coordinate system - Stack Overflow; http://stackoverflow.com/questions/3798333/image-information-along-a-polar-coordinate-system/3806851#3806851 (accessed Aug 27, 2013).
(35) Wiener, N. *Acta Math.* **1930**, *55*, 117−258.
(36) Khintchine, A. *Math. Ann.* **1934**, *109*, 604−615.
(37) Jolliffe, I. T. Principal Components in Regression Analysis. In *Principal Component Analysis*; Springer: New York, 2002; pp 167−198.
(38) Wright, B. A.; Cole, P. A. *Acta Crystallogr.* **1949**, *2*, 129−130.
(39) Carter, C. Barry, M. G. N. *Ceramic Materials*; Springer New York: New York, 2007; pp 444−462.
(40) Wampler, R. D.; Kissick, D. J.; Dehen, C. J.; Gualtieri, E. J.; Grey, J. L.; Wang, H.-F.; Thompson, D. H.; Cheng, J.-X.; Simpson, G. J. *J. Am. Chem. Soc.* **2008**, *130*, 14076−14077.
(41) Seijas, L. E.; Delgado, G. E.; Mora, A. J.; Fitch, A. N.; Brunelli, M. *Powder Diffr.* **2012**, *25*, 235−240.
(42) Lee, J. L. S.; Gilmore, I. S.; Seah, M. P. *Surf. Interface Anal.* **2008**, *40*, 1−14.
(43) Loukas, C. G.; Wilson, G. D.; Vojnovic, B.; Linney, A. *Cytom. A* **2003**, *55*, 30−42.
(44) Klussmann, M.; White, A. J. P.; Armstrong, A.; Blackmond, D. G. *Angew. Chem., Int. Ed. Engl.* **2006**, *45*, 7985−7989.
(45) Klussmann, M.; Iwamura, H.; Mathew, S. P.; Wells, D. H.; Pandya, U.; Armstrong, A.; Blackmond, D. G. *Nature* **2006**, *441*, 621−623.
(46) Kellogg, R. M. *Angew. Chem., Int. Ed. Engl.* **2007**, *46*, 494−497.

analytical chemistry

Article

pubs.acs.org/ac

Powders Analysis by Second Harmonic Generation Microscopy

Azhad U. Chowdhury, Shijie Zhang, and Garth J. Simpson*

Department of Chemistry, Purdue University, 560 Oval Drive, West Lafayette, Indiana 47907, United States

ABSTRACT: A microscopy approach is developed for quantifying second harmonic generation (SHG) activity of powders that largely decouples linear and nonlinear optical interactions. Decoupling the linear and nonlinear optical effects provides a means to independently evaluate and optimize the role of each in crystal engineering efforts and facilitates direct comparisons between experimental and computational predictions of lattice hyperpolarizabilities. In this respect, the microscopy-based approach nicely complements well-established Kurtz-Perry (*J. Appl. Phys.* **1968**, *39*, 3798) and related methods, in which collimated sources are used for powders analysis. Using a focused fundamental beam places a controllable upper bound on the interaction length, given by the depth of field. Because measurements are performed on a per-particle basis, crystal size-dependent trends can be recovered from a single powdered sample. An analytical model that includes scattering losses of a focused Gaussian beam reliably predicted several experimental observations. Specifically, the measured scattering length for SHG was in excellent agreement with the value predicted based on the particle size distribution. Additionally, histograms of the SHG intensities as functions of particle size and orientation agreed nicely with predictions from the model.

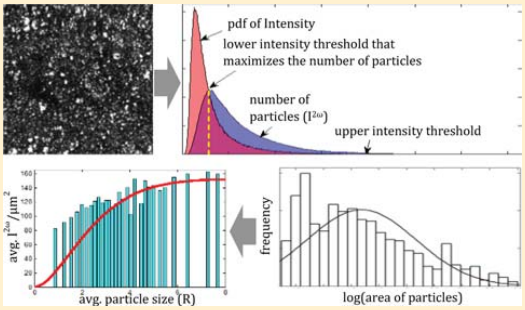

The SHG activity of powders is a common and important measurement, both historically for the characterization of efficiency in new nonlinear optical materials and more recently as an analytical tool for quantitative analysis of pharmaceutical materials. In the design of new materials for frequency conversion, powder second harmonic generation (PSHG) is routinely measured for preliminary assessments as it avoids the need to produce large single crystals. In pharmaceutical materials, Coquerel and co-workers used PSHG to observe structural phase transitions in powders,[1−3] identify SHG-active structural impurities,[3,4] and screen for the generation of homochiral conglomerates.[3,5] Measurement of the PSHG activity is also frequently reported as a powerful method for pharmaceutical crystal analysis, due to its low detection limit, fast response time, nondestructive nature, and low cost of automation.[1,6] The PSHG activity of active pharmaceutical ingredients (APIs) was shown to enable discrimination of polymorphism[7−10] and quantify API crystallinity within mixtures.[7−9,11] Detection limits for trace API crystallinity within amorphous formulations in the parts per million regime have been reported.[6,12−14] Studies by Wanapun et al. yielded insights into the mechanism behind the milling-induced loss of crystallinity within API powders.[13] In studies by Berglund and co-workers, PSHG enabled sensitive measurements of the induction times for crystallization from supersaturated solutions.[15] The sensitivity of SHG to polymorphism suggests the potential for expanded applications in routine crystal form screening of new APIs, which is routinely performed prior to development of final dosage forms. These practical applications appeal to the ever increasing demand in pharmaceutical industry for chiral crystal analysis, which boosts the development of enantioselective synthesis methods of pure enantiomer APIs.

The large majority of these applications hinge on reliable quantitative analysis for reproducibly recovering SHG activities connected directly to lattice properties. However, reproducible SHG signal quantification is often frustrated by the acquisition of SHG intensities that are also highly dependent on the crystal size distribution, the sample thickness, the presence or absence of phase-matching, and the packing density.[16−19] The most commonly accepted approach remains the Kurtz-Perry (KP) method in which the intensity of the transmitted and/or backscattered SHG are recorded using a collimated fundamental source.[19] By repeating KP measurements using different particle sizes, it is possible to discriminate between phase matchable (PM) and nonphase matchable (NPM) materials from the dependence of the SHG with mean. The presence of phase-matching, in which the refractive indices of the fundamental and doubled frequency are identical due to a perfect matching of dispersion and birefringence, can profoundly impact the net SHG intensity produced by a powder.[16−20] The influence of phase-matching is also generally highly size-dependent. As such, the inherent spread of crystal sizes present within a typical powder sample can be nontrivial to include in the modeling and data inversion.

Received: December 31, 2015
Accepted: March 1, 2016
Published: March 1, 2016

   DOI: 10.1021/acs.analchem.5b04942
Anal. Chem. 2016, 88, 3853−3863

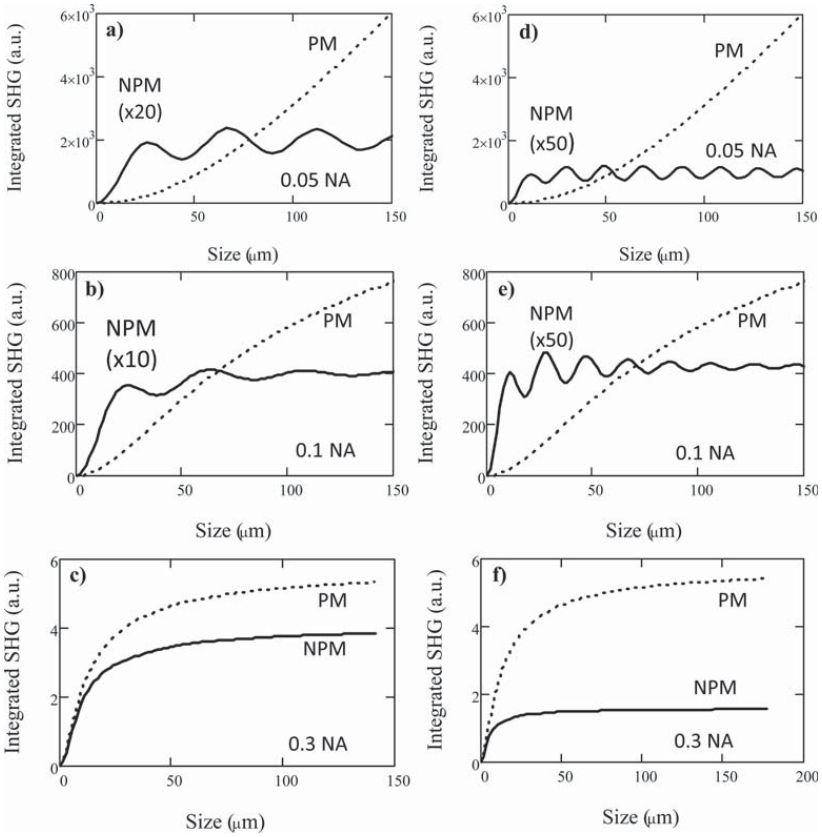

Figure 1. Theoretical SHG activity of a powder under phase matched (PM) and nonphase matched (NPM) conditions calculated for different numerical apertures, in which the interaction length is dictated by the dimensions of the particle or the optical scattering length (whichever is shorter). The top curve corresponds most closely to the conventional KP method using nominally collimated light, while the bottom is more representative of the measurement configuration used in the present study. Calculations were performed using average optical constants and coherence lengths from nine nonaromatic (a–c) and seven aromatic (d–f) organic molecules.

Substantial improvements on the KP method have been suggested by several researchers. Aramburu et al. have updated the KP method to include the effects of light scattering in the analysis of the SHG process.[16] Kiguchi et al. have proposed a creative alternative approach, in which the powder measurements are performed using an evanescent wave in a total internal reflection configuration. In this manner, the interaction length with the fundamental beam in the powder is reduced to less than the wavelength of light, significantly reducing effects related to phase-matching.[20,21] Nevertheless, the limited number of observables present in ensemble-averaged experiments using collimated sources fundamentally complicates reproducible separation of the many competing contributions to the SHG intensity and, in turn, the determination of the nonlinear susceptibility.

In this work, a microscopy-based analysis approach is described, which greatly increases the number of observables in powders analyses. The model includes consideration of the impact of the numerical aperture, optical scattering, packing density, crystal orientation, size, and phase-matching. Predictions of the model based on the focusing of a Gaussian beam are compared with experimental observables for both isolated nanoparticles and condensed powders.

EXPERIMENTAL SECTION

Sample Preparation. The 500 nm diameter barium titanate ($BaTiO_3$) nanoparticles were purchased from US Research Nanomaterials, Inc. and suspended in polyethylene glycol (PEG, MW = 380–420 g/mol) in between coverslips. The size distribution was confirmed using scanning electron microscopy (SEM). In order to prepare the sample, 0.01 g of $BaTiO_3$ nanoparticles were added and mixed in 1 g of molten PEG, which was kept in a hot water bath.

Sucrose was ground using a mortar and a pestle to make a fine powder. The powder was sieved through a 25 × 25 μm^2 mesh before loading into 400 μm inner diameter square capillary tubes. All the capillaries were loaded up to a similar height (~0.7 cm).

Simulations. Representative optical constants for the simulations were obtained using literature values. The refractive indices for 1,4-dioxane, 1,5-pentanediol, 1-butanol, propanol, acetonitrile, methanol, toluene, and benzene were generated from a five-parameter Cauchy equation using the coefficients

DOI: 10.1021/acs.analchem.5b04942
Anal. Chem. 2016, 88, 3853–3863

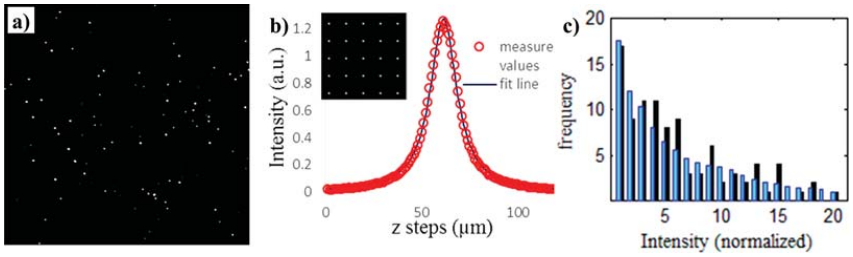

Figure 2. Recovery of the beam intensity profile as a function of axial position. (a) Image of the brightest frame from the optical sectioning of 500 nm $BaTiO_3$ nanoparticles suspended in polyethylene glycol. A total of 25 nanoparticles were randomly chosen from the raw image and cropped with 30 × 30 pixels centering the corresponding particle to make a new image stack. Surface of each individual nanoparticle's area was shifted accordingly to bring all nanoparticles in the same focal plane. (b) Fitting of the measured SHG intensity to a Lorentzian function. Each circle corresponds to the mean integrated SHG of each frame from the new surface shifted image stack. The recovered Rayleigh range of the Lorentzian beam profile was 8.44 ± 0.05 μm. The brightest frame of the new image stack is shown in the inset. (c) Intensity distribution of particles (filled column) from the brightest frame of a surface shifted image (N = 97), compared to the theoretical prediction of the intensity distribution (lightly filled) based on literature values for the tensor elements of $BaTiO_3$.

from Moutzouris et al.[22] Optical constants for ethylene glycol were taken from Sani and Dell'Oro,[23] propylene glycol from Otanicar et al.,[24] acetone, methyl salicylate, ethyl salicylate, and cinnamaldehyde from Rheims et al.,[25] nitrobenzene and ethanol from Kedenburg et al.,[26] and styrene from Sultanova et al.[27]

Imaging. A built-in-house beam scanning microscope was used in this experiment for Z-sectioning. A Tsunami ultrafast Ti:sapphire mode-locked laser (800 nm, 80 MHz, 125 fs, 10 mW) was focused through a 10× objective (Nikon Plan Fluor, numerical aperture, NA = 0.30), and the beam was scanned over the sample using a resonant fast-scan mirror (7.8 kHz, CambridgeTech) and a galvanometer slow-scan mirror. Z-scanning was achieved by translating the sample with a Newport motion controller. The detected SHG was collected back through the objective followed by a 680 nm long pass filter to a photomultiplier tube. A synchronous-digitization data acquisition module was used to time the data acquisition to the laser pulse frequency through a 10 MHz phase locked loop.[28] Images were created by binning the recorded SHG intensities into 512 × 512 pixels. Spatial resolution of this microscope was calibrated to 0.87 μm/pixel using a 1951 USAF resolution test grid. All measurements were performed with epi-detection on powders with thicknesses significantly greater than the scattering length, such that the recovered SHG consists of contributions from both the directly backward-generated SHG and the forward-generated then subsequently backward scattered SHG. As such, it is assumed that the detected SHG collected by the objective provided a representative sampling proportional to the overall net SHG intensity produced from a given location.

RESULTS AND DISCUSSION

Modeling the Impact of Numerical Aperture. An optical model is proposed and detailed in the Appendix, which explicitly considers a focused Gaussian beam, optical scattering effects, and phase matching. Predictions of the model are shown in Figure 1, highlighting the influence of the numerical aperture and tightness of focus on the disparity between the total SHG intensities produced from PM and NPM materials. Consistent with microscopy measurements, the traces correspond to single crystals rather than ensemble averages, differing only in the PM versus NPM nature of the nonlinear optical interaction. Calculations were performed using average refractive indices at 1064 and 532 nm, for sets of both nonaromatic and aromatic organic condensed phases as a function of the mean particle size (given by the equivalent radius R). In the PM cases, the depth of the field dictated the interaction lengths, while in all the NPM cases considered the interaction length was limited by the scattering length. Several noteworthy trends emerge from the modeling predictions.

First and foremost, the difference between the SHG produced from PM and NPM crystallites is dramatically reduced with increases in the numerical aperture (NA). For the nonaromatic organics with relatively long coherence lengths of ∼31 μm, the ratio of the PM to NPM SHG intensities, $I^{2\omega}_{PM}/I^{2\omega}_{NPM}$, for a 100 μm crystal was 1.4, corresponding to only a 40% increase for PM crystallites. In contrast, that number jumped to $I^{2\omega}_{PM}/I^{2\omega}_{NPM}$ = 15 for an NA of 0.1, and $I^{2\omega}_{PM}/I^{2\omega}_{NPM}$ = 32 for an NA of 0.05. The marked decline in sensitivity to PM versus NPM in the 0.3 NA case arises as the coherence length l_c becomes small relative to the interaction length, which in the limit of large particles relative to l_c is set by the depth of field (corresponding to ∼7 μm for a 0.3 NA and a 1064 nm source).

The preceding analysis espousing the benefits of higher NA measurements are partially offset in practice by a generally competing desire to reduce uncertainties from nonrepresentative sampling, in which the measurements may be biased by not sampling a sufficiently large statistical population of particle sizes and orientations. Nonrepresentative sampling can generally be minimized by expanding analyses to large fields of view to probe a greater population of crystallites. However, accessing a larger field of view by lower magnification generally corresponds to the use of a lower NA objective. Consequently, fewer total fields of view are required to generate results that statistically sample all crystal orientations, suggesting the desire for low magnification, low numerical aperture objectives.

In the present study, a balance was struck between these two competing effects based on analysis of the anticipated coherence length expected in a nonaromatic organic solid. Unfortunately, the optical constants of many organic solids are challenging to measure and/or find reported in the literature. However, a wealth of data exists for the wavelength dependent optical constants of pure organic liquids, which can serve as surrogates for general estimations of coherence lengths in condensed phase organic materials. Pooling the results from 14 organic liquids yields an average coherence length for SHG

DOI: 10.1021/acs.analchem.5b04942
Anal. Chem. 2016, 88, 3853−3863

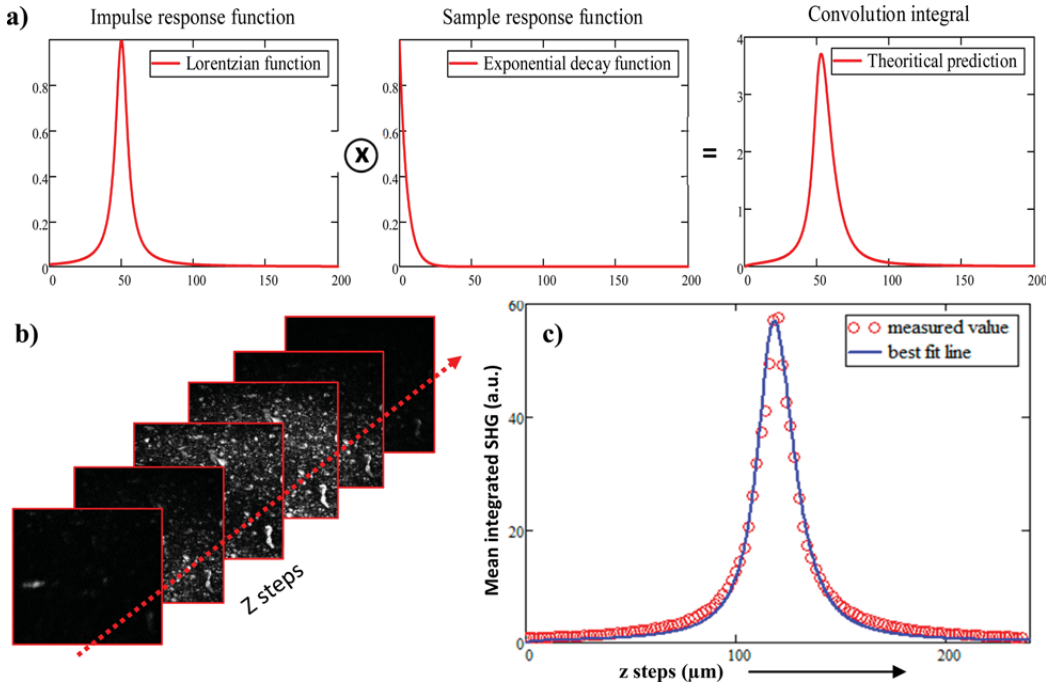

Figure 3. Determination of the scattering length l_s. (a) Depicted analytical expression for the measured intensity from an optical sectioning, which is a convolution of a Lorentzian beam profile with a single-sided exponential decay function. (b) Representative image of optical sectioning. (c) Mean integrated SHG from the surface shifted image fitted to the convolution integral. Using the measured Rayleigh range of the Lorentzian function from Figure 2, the recovered scattering length was 4.7 ± 0.6 μm.

with 1064 nm incident light of 24 μm (±11 μm). Considering just the nonaromatic organics consistent with sucrose increases, the coherence length is 31 μm (±6 μm). Both of these values are on par with or greater than the ∼17 μm depth of field obtained for the 10× objective used (detailed in the next section), such that the depth of field of the objective is likely to dictate the upper limit on the net interaction length rather than the forward coherence length. A higher NA objective would further reduce the impact of the forward coherence length but would also likely sample a significantly smaller field of view with corresponding increases in total measurement time for representative sampling.

Isolated Point Source Measurements. As a prelude to powders analysis, a series of measurements was performed using $BaTiO_3$ nanoparticles as ground-truth point sources for characterizing the influence of particle position and orientation on the detected SHG intensity. Results highlighting two effects are shown in Figure 2. As one might expect, the brightness of SHG in any given field of view varied considerably from nanoparticle to nanoparticle, both due to the axial position of the particles relative to the focal plane and due to orientational effects. The axial position-dependence was corrected by analyzing each particle relative to the focal plane producing the maximum SHG intensity, as a prelude to analogous operations in powders. Measurements acquired without shifting result in significant broadening in the Z-profile due to convolution with the random distribution in position. Optical sectioning of a point source (in this experiment 500 nm $BaTiO_3$ nanoparticles following Z-shifting) returns the squared intensity profile of the fundamental beam because the convolution of any function with an impulse function replicates the function centering the position at impulse.[29,30] From a selective cropping of 25 nanoparticles throughout the whole stack, a new image stack (125 pixels × 125 pixels × length of z-scan) was created. A square area (30 × 30 pixels) around the particle was selected and cropped out from the entire stack. Following Z-correction, the integrated intensity as a function of axial displacement is well-fit to a Lorentzian distribution in Figure 2b, consistent with expectations for a Gaussian incident beam.[31] The recovered depth of field of 16.9 ± 0.1 μm (given by twice the Rayleigh range) is larger than the theoretically expected of 7.07 μm for a 0.3 N.A. 10× objective with an incident wavelength of 1064 nm, suggesting underfilling of the objective for an effective NA of 0.2.

From the Z-corrected images, a histogram of particle brightness is shown in Figure 2c. The measured distribution in dark blue is overlaid with the theoretical distribution in light blue generated from Monte Carlo simulations of the anticipated SHG intensity in which all nanoparticle orientations are equally probable. No adjustable parameters were used in the generation of the theoretical results, which were produced using previously reported tensor elements for $BaTiO_3$.[32] All simulated results were based on the hyperpolarizability of the lattice and independent of linear optical effects such as phase-matching. Since the nanoparticles are significantly smaller in dimension than the forward coherence length, the interplay between the linear and nonlinear optical properties is almost completely removed, with the observed SHG intensity per unit volume predicted and measured depending exclusively on the native hyperpolarizability of the lattice.

DOI: 10.1021/acs.analchem.5b04942
Anal. Chem. 2016, 88, 3853−3863

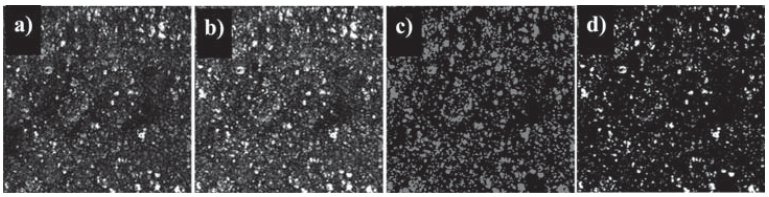

Figure 4. Illustration of the image processing: (a) representative SHG image of sample surface, (b) brightest frame following per-pixel Z-shifting, (c) binary mask containing particles size 4 μm^2< area of particles <625 μm^2, (d) representative raw image of sample surface after all the processing.

Despite the excellent correspondence between theory and experiment in studies of $BaTiO_3$ nanoparticles, the sample itself is not representative of typical powders. In general, the samples targeted for powders analysis by SHG will exhibit a diversity of sizes rather than be manufactured to within tight size tolerances as the case of the $BaTiO_3$ nanoparticles. Furthermore, most powders will exhibit much higher packing densities of SHG-active materials, with the density of $BaTiO_3$ carefully selected in the present study to ensure independent access to individual, well-separated nanoparticles. Nevertheless, the $BaTiO_3$ serves two important roles in the present work: (i) for characterization of the axial profile of the beam as demonstrated in Figure 2b and (ii) for calibration as a reference material for absolute quantification of the lattice hyperpolarizabilities of powdered samples.

Optical Scattering Measurements. The experimental impact of optical scattering on quantification based on SHG microscopy measurements is shown in Figure 3. In the figure, images were Z-shifted on a per-pixel basis, then integrated across the field of view at each Z-position relative to the maximum. The overall measured signal is expected to decay exponentially following the Beer−Lambert law due to scattering losses.[33] Therefore, the Z-dependent SHG can be modeled by the convolution of a Lorentzian beam profile and a single-sided exponential function depicted in Figure 3a. Accordingly, the integrated intensity data were fit to such a model, producing a decay length for the SHG of 4.71 ± 0.06 μm. The measured exponential decay length is significantly shorter than the depth of field and the anticipated forward coherence length, consistent with the limits illustrated in Figure 1 suggesting minimal differences in the SHG produced from PM versus NPM particles. The short decay length observed in measurements is therefore consistent with only a relatively minor skewness perturbation to the otherwise nominally Lorentzian distribution shown in Figure 3c. The rapid decay observed in the present studies suggests that the bulk of the signal in the microscopy measurements originates from a skin depth of only a few micrometers.

These observations are in good qualitative agreement with previous studies using optical clearing to probe SHG of powders.[16,17] By immersing the sample in a refractive index matched oil, the overall SHG activity of the powder was found to substantially increase, attributable to the increase in penetration depth.[16] By increasing the width of the exponential function in Figure 3a, the resulting convolved function will be much more highly skewed with a significantly longer tail and a larger integral, consistent with the ensemble-averaged observations from the optical clearing studies. As such, systems exhibiting relatively long penetration depths associated with low optical scattering and/or long depths of field are likely to exhibit greater dependence of the detected SHG intensity by the Kurtz-Perry method on both the linear and nonlinear optical properties. For collimated sources averaging over large areas, unambiguously disentangling these two contributions is generally not trivial, as has been indicated previously.[16]

Crystal Orientation, Size, and Phase-Matching. The interdependence of the detected SHG intensity on the crystal size distribution and the differences in behaviors in the presence or absence of phase-matching are among the most challenging aspects for disentangling the linear and nonlinear optical properties in analyses of powdered samples. For collimated sources in which measurements are integrated over many crystals with many sizes and orientations, only a handful of experimental observables are dependent on numerous parameters related to the particles under analysis. However, SHG microscopy coupled with image analysis provides a convenient route forward by providing measurements on a per-particle basis.

Most directly, the theoretical framework developed in the Appendix suggests that the relatively rare occurrence of phase-matching in a phase matchable material can be easily corrected by imaging. In the limit of the depth of field or scattering length being much smaller than the coherence length, the minor enhancement in the integrated SHG from relatively rare PM orientations are small enough to be neglected in the analysis. Conversely, as the NA is reduced and the mean particle size is increased, the disparity between the per-particle brightness under PM and NPM conditions rapidly increases. As the crystals become larger, a smaller fraction of them are opportunely oriented to generate phase matching, and the disparity between the brightness of those increasingly rare events and the NPM orientations becomes ever greater. Deviation from the anticipated behavior under NPM conditions illustrated in Figure 1 can be readily identified (e.g, by a statistical test), and the PM outliers separated for rejection or independent analysis.

Image analysis provides a means to both identify and correct SHG microscopy measurements in ways that have no simple analogs in measurements with collimated sources, such as in the Kurtz-Perry method. From inspection of the raw SHG images produced in powder measurements shown in Figure 4, only a relatively small fraction of the locations interrogated produced substantial SHG signals. The data shown in Figure 4b are Z-shifted on a per-pixel basis to remove effects related to variability in the axial positions of particles within the powder. Consequently, the dark locations in the images can be attributed to voids in the powder and/or regions rendered dark from scattering losses prior to intersection of the beam with SHG-active moieties.

In order to improve the accuracy of the determinations for the SHG-activity per unit volume of crystalline material, the void regions were omitted from the subsequent analysis. The

DOI: 10.1021/acs.analchem.5b04942
Anal. Chem. 2016, 88, 3853−3863

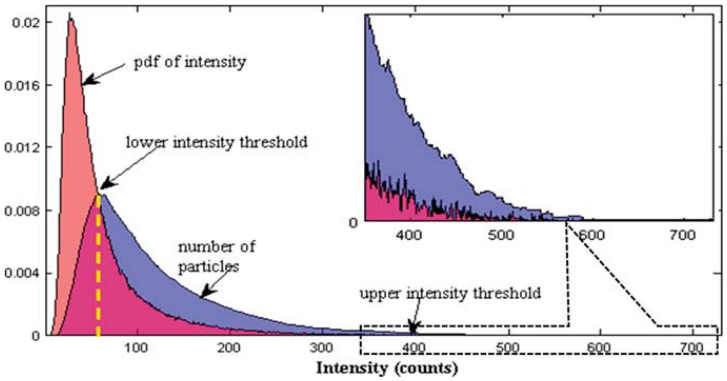

Figure 5. Illustration of the approach used to select the lower and upper thresholds prior to particle counting. The red plot to the left represents the histogram of per-pixel intensities from the brightest frame of a Z-shifted stack. The blue plot to the right represents the number of particles recovered from the brightest image frame. The yellow dashed line indicates the lower intensity threshold that maximizes the number of particles. The upper intensity threshold was set by discarding values exceeding standard deviations (3σ) of the mean intensity.

void-rejection was accomplished based on maximization of the number of counted particles in the image, illustrated in Figure 5. In brief, the number of particles identified in the images was determined as a function of an intensity threshold. For thresholds too low, coalescence between particles from dark counts and crystal overlap produced a small number of relatively large crystals. On the other extreme, too high of a threshold resulted in the identification of only a few of the very brightest crystals. Maximization of the particle number provides a reproducible compromise between potential bias introduced by these two limiting factors.

A z-test was performed to identify and reject anomalously bright rare particles in Figure 5 corresponding to potential phase-matched candidates. In brief, a single-sided confidence interval of 99.9% (i.e., 3σ) was used to identify particles statistically different from the parent population. Sucrose has been established as being phase-matchable,[34] such that the SHG intensity of a powder is potentially influenced greatly by the presence of a relatively small volume fraction of appropriately oriented crystals. However, the conditions for phase-matching constitute the exception rather than the rule, with the large majority of particles presenting in nonphase matched orientations. This disparity is clearly evident in Figure 5, in which the tail of the distribution in per-pixel brightness extends well into the wings to include a handful of anomalously bright particles. Particles with a per-pixel brightness exceeding three standard deviations (3σ) were removed from the pool prior to evaluation of the SHG activity per unit volume of crystalline material. This selective rejection strategy allowed both phase-matchable and nonphase-matchable materials to be characterized in equal mathematical footing. Rejection of the PM component in phase-matchable materials produced SHG intensities dominated by the inherent nonlinear optical properties of the lattice largely independent of perturbations from linear optical effects in both PM and NPM materials.

Packing Density. Although often not explicitly included in models of powders, only the volume fraction of the powder that is present in the solid form can contribute to the detected SHG activity. As such, more densely packed powders of the same material are likely to produce a higher measured SHG intensity per unit area/volume than the same materials prepared with greater dead-volumes between crystallites. This effect is evident in Figure 6, in which the raw integrated SHG intensity was recorded at different positions within a capillary tube. The

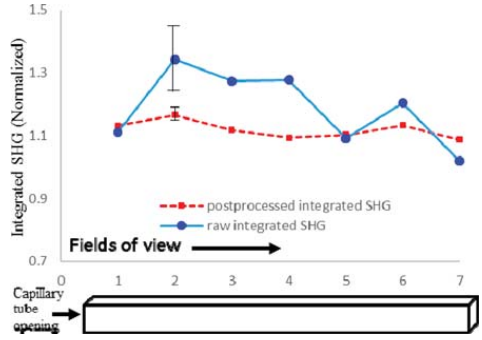

Figure 6. Comparison of the raw versus corrected SHG intensity measured from the different locations in a packed capillary tube (normalized to 500 nm of $BaTiO_3$ nanoparticles). Measurement uncertainty was reduced ~90% by combining SHG measurements with image analysis.

particle density toward the opening of the capillary are generally greater than in the interior, as higher forces are required to add additional material to a packed capillary than to fill the initially empty capillary tube. Consistent with these expectations, substantial variability was observed in the integrated SHG intensity recorded from different locations within the capillary tube.

Fortunately, the void rejection algorithm described in the preceding discussion on Crystal Orientation, Size, and Phase-Matching naturally accomplishes much of the corrections for packing density. A comparison of the integrated SHG intensity and the corresponding SHG activity per unit area correcting for voids is also given in Figure 6. In the uncorrected case, the variability from one field of view to another substantially exceeded the inherent measurement error, suggesting the dominant source of measurements variance was from systematic differences across multiple fields of view. However, the combination of dead-volume and bright outlier rejection resulted in a statistically indistinguishable set of measurements

DOI: 10.1021/acs.analchem.5b04942
Anal. Chem. 2016, 88, 3853−3863

at all locations along the capillary tube, with substantial corresponding reductions in measurement uncertainty.

Image analysis in this manner based on particle counting also has the additional advantage of directly providing the particle size distribution shown in Figure 7. Recovery of the full

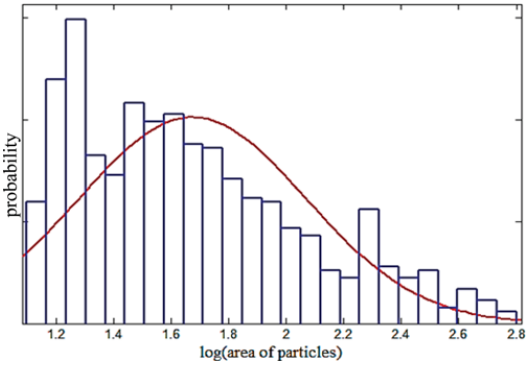

Figure 7. Histogram of $\log_{10}$(particle area) fitted to a normal distribution, corresponding to a log-normal distribution in particle sizes. The mean particle size was 82 μm^2.

histogram of crystal sizes and the corresponding SHG activities on a per particle basis allows analyses that are fundamentally inaccessible from an integrating KP-type analysis, as detailed in the next section.

Predictions of the Model. The scattering model described in the Appendix results in several predictions that can be tested experimentally. First, the model predicts a simple relationship between the mean particle size given by the equivalent radius R and the scattering length l_s of $l_s \cong R$. The fit of the ensemble-averaged SHG intensity as a function of Z-position in Figure 2 yields a value of l_s = 4.7 μm (±0.6 μm). From image analysis, a representative histogram of particle sizes for the sucrose powder explored are shown in Figure 7, with the mean particle area given by 82 μm^2. The particle area can be used to recover R by assuming an "equivalent sphere" scattering cross-section of πR^2,[16−18] yielding a value of R = 5.1 μm. Despite being calculated based on very different analyses, the values of l_s and R are easily within experimental error of each other, supporting the simple link between the mean particle size and the scattering length in the powder suggested by eq 3 of the Appendix.

Because microscopy measurements recover a full histogram of size-dependent SHG activities, trends with respect to particle size can also be compared with theoretical predictions. The SHG activity per unit area is shown in Figure 8, calculated by combining the histogram of sizes with the integrated brightness on a per-particle basis. The experimental results are compared with predictions based on the model, assuming an interaction length dictated by the particle radius R when $R \leq l_s$ and by l_s when $l_s < R$. Good agreement is observed between the theoretical and experimental trends. Most notably, the model predicts fairly rapid saturation of the per-particle SHG with increasing particle radius in the regime $l_s < R$, in general agreement with observations.

From these combined measurements, the inherent mean SHG activity per unit volume can be recovered nominally independently of linear effects by combining the results from

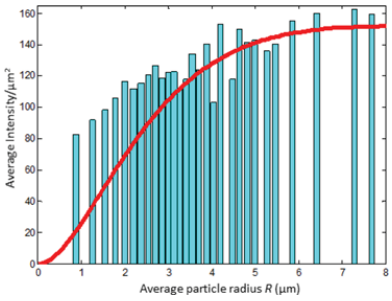

Figure 8. Measured size-dependent SHG intensity recovered from the histogram of particle intensities (vertical bars) is compared with the theoretical predictions of the model using the measured scattering length with the intensity scaling as the only adjustable parameter (solid curve).

Figures 3 and 8. In brief, the volume is determined based by combining the mean SHG per unit area with the mean interaction length, in this case given by the scattering decay length of 4.7 μm when $R > l_s$ and by R for smaller particles. The SHG activity per unit volume is given by $\langle I^{2\omega}/V\rangle \cong \langle I^{2\omega}/A\rangle/(4l_s/3)$, where the factor of $4l_s/3$ arises from ratio of the volume to area of a sphere. The orientationally averaged values for the effective susceptibility of sucrose normalized to $BaTiO_3$ is 4.3%, corresponding to a ratio of the SHG intensity per unit volume of 0.19% relative to $BaTiO_3$. Using literature values for the susceptibility element of $BaTiO_3$ of d_{15} = 17.2 pm/V, d_{31} = 18.0 pm/V, and d_{33} = 6.6 pm/V,[32] isotropic orientational averaging as described by Bersohn et al.[35] for hyper-Rayleigh scattering (HRS) results in an effective susceptibility of $\langle\chi_{eff}\rangle_{\theta\psi\phi}$ = 17.7 pm/V for $BaTiO_3$. In brief, a statistical assembly of particles with uniformly distributed orientations will converge to an isotropically averaged laboratory-frame squared magnitude of $\langle\vec{\chi}^*_{ZZZ}\vec{\chi}_{ZZZ}\rangle_{\theta\psi\phi}$ for coparallel polarized detection and $\langle\vec{\chi}^*_{YZZ}\vec{\chi}_{YZZ}\rangle_{\theta\psi\phi}$ for cross polarized detection, the combined square root of which was used to evaluate $\langle\chi_{eff}\rangle_{\theta\psi\phi}$. Using the 4.3% scaling yields a corresponding value for sucrose of $\langle\chi_{eff}\rangle_{\theta\psi\phi}$ = 0.76 pm/V.

The results obtained in the present study correspond to a per-volume SHG activity for sucrose that are roughly an order of magnitude larger than previous reports. In early studies by Kurtz and co-workers using KDP powder as a reference material, SHG activities of ∼0.08 pm/V were reported based on measurements of powders prepared by mechanical grinding with sizes on the order of 40−120 μm.[34] Similar results were obtained in more recent studies by Piela and co-workers, in which the SHG coefficients for sucrose were determined to be ∼0.11 pm/V (also prepared by mechanical grinding but with no estimation of the anticipated size distribution).[36] In contrast, the present measurements were performed for a powder with a mean particle size of only ∼10 μm in diameter and a much shorter interaction length. Two likely possibilities emerge for the disparity: (i) the microscopy measurements of sucrose produce a higher per-volume SHG activity than conventional powder measurements or (ii) the microscopy measurements of $BaTiO_3$ nanoparticles yield lower than anticipated per-volume SHG activity. A combination of both effects is possible. In the case of sucrose, the interaction length may have been overestimated if based on the coherence length rather than

DOI: 10.1021/acs.analchem.5b04942
Anal. Chem. 2016, 88, 3853−3863

the scattering length, such that the effective volume over which the SHG activity arose was smaller than anticipated. Furthermore, if the $BaTiO_3$ reference nanoparticles were not perfectly single-crystalline or included an amorphous surface layer, the effective volume contributing to the detected SHG may be less than the geometrical particle volume, leading to a corresponding overestimation of the sucrose activity. We tentatively attribute the disparity primarily to the first of the two considered interactions, as a fair body of work has evolved supporting the formation of single-domain $BaTiO_3$ particles in the size regime used herein (500 nm).[37,38]

The good agreement between the predictions and observations in the SHG microscopy analysis presented herein are consistent with recent comparisons between predicted and measured SHG activities of several pharmaceutical solids based on SHG imaging.[6] In that previous work,[6] generally good agreement was observed between the integrated SHG intensity measured using an objective with a comparable NA and *ab initio* predictions based on molecular hyperpolarizability calculations for the lattices. This agreement is quite remarkable, as no corrections for phase-matching were made to the measurements and no particle size information was recorded or used in the analysis.

As a consequence of its preferential selectivity for the nonlinear optical properties alone, SHG microscopy, as illustrated in Figure 1 generally provides information that is highly complementary to that recovered by the Kurtz-Perry method.[19] The KP method yields integrated values depending on both the linear and nonlinear optical properties, particularly in phase-matchable materials. However, much of the SHG intensity in a phase-matchable material arises from a relatively small population of appropriately oriented crystallites. As the mean particle size increases, the number of particles capable of PM measurements is linearly reduced and the brightness per PM particle quadratically increased, resulting in an overall linear intensity scaling with mean particle size.[16] Consequently, the statistical tests designed to selectively identify outliers should be significantly more effective as the particle size is increased. SHG microscopy measurements as a function of NA can potentially not only provide the inherent lattice hyperpolarizability from the statistical population of SHG activities but also clearly identify between phase-matchable and nonphase matchable materials based on simple statistical outlier tests of particle brightness.

SUMMARY

A method is described for removing phase-matching effects in SHG measurements of powders. The general measurement flow is as follows:

(1) Record a *Z*-stack of SHG microscopy measurements for the powder in question.

(2) Process images as illustrated in Figure 4: (i) *Z*-shift the pixels such that the maximum intensity in the *Z*-stack at every position is at $Z = 0$, (ii) for the $Z = 0$ plane, select a lower intensity threshold based on maximizing the total number of particles in an image or set of images, and (iii) reject outlying particles with intensities greater than three standard deviations of the mean, corresponding to possible phase-matched orientations.

(3) Measure the attenuation length by integrating the SHG intensity in each *Z*-plane and fitting the result to the Lorentzian ⊗ exponential convolution as illustrated in Figure 3.

(4) Determine the asymptotic value of the SHG intensity per unit area $\langle I^{2\omega}/A\rangle$ in the limit of large *R* using particle counting algorithms as illustrated in Figure 8.

(5) Convert $\langle I^{2\omega}/A\rangle$ to the average SHG intensity per unit volume $\langle I^{2\omega}/V\rangle$ by dividing by the effective interaction length. Depending on the numerical aperture and average crystal size, the interaction length could be dictated by the scattering length l_s, the depth of field l_d, or the average forward coherence length l_c. The corresponding scaling of the interaction lengths to convert to effective volume in each case are derived explicitly in the Appendix.

$$\text{If } l_s << (l_c, l_d),\ \langle I^{2\omega}/V\rangle \cong \langle I^{2\omega}/A\rangle/(4l_s/3) \quad \text{(a)}$$

$$\text{If } l_d << (l_c, l_s),\ \langle I^{2\omega}/V\rangle \cong \langle I^{2\omega}/A\rangle/l_d \quad \text{(b)}$$

$$\text{If } l_c << (l_d, l_s),\ \langle I^{2\omega}/V\rangle \cong \langle I^{2\omega}/A\rangle/(\pi l_c/2) \quad \text{(c)}$$

(6) Normalize the recovered ⟨SHG/V⟩ to a standard (e.g., $BaTiO_3$ nanoparticles of known size).

Measurements performed using this approach for sucrose powder yielded good agreement between several theoretical predictions and experimental observations. The measured scattering length was found to be in excellent agreement with the effective radius based on the particle size distribution determined by image analysis of SHG micrographs. The model also resulted in marked reductions in measurement uncertainties related to variance in packing density. Furthermore, the SHG-activity as a function of particle size could be determined by taking advantage of the inherent variability in crystal dimensions within a powder, yielding size-dependent SHG activity in good general agreement with the expectations of the model from a single powder sample with no adjustable parameters.

The proposed microscopy-based approach provides a nice complement to alternative established approaches based on ensemble averaged measurements with collimated or gently focused incident beams. In particular, the proposed approach yields measurements that are largely immune to complications from phase-matching, providing measurements of the nonlinear susceptibility more directly tied to the native nonlinear optical properties of the lattice.

APPENDIX

Theoretical Foundation

In the present formulation, three separate effects can potentially limit the interaction length between the fundamental beam and a crystalline powder driving the production of SHG: (i) the scattering length, (ii) the forward coherence length, or (iii) the depth of field. To treat scattering effects, a theoretical framework developed by Aramburu et al.,[16−18] which explicitly includes the role of optical scattering in the modeling, was modified for compatibility with microscopy-based measurements. Using an equivalent spheres model, the scattering length l_s can be written in the following form.

$$l_s = \frac{1}{\rho\sigma_s} \quad (1)$$

In eq 1, ρ is the density of scatterers and σ_s is the scattering cross section for each particle. In the limit of high refractive index mismatch (e.g., powder in air), the non-forward scattering cross-section $\sigma_{s,\text{"nonforward"}}$ becomes equivalent to the geometrical area of the particle, as both the scattered and

DOI: 10.1021/acs.analchem.5b04942
Anal. Chem. 2016, 88, 3853−3863

transmitted portions of the beam will generally result in the loss of coherence. Assuming the refracted and scattered components are roughly equal in magnitude, the net scattering cross section σ_s is twice the non-forward cross section.

$$\sigma_{s,\text{"nonforward"}} \cong \pi R^2 \cong \frac{1}{2}\sigma_s \tag{2}$$

In eq 2, R is the radius of an equivalent spherical scatter with a cross-sectional area of πR^2. The decay length l_s can be expressed in terms of the fraction of occupied volume rather than the density by the substitution $f = \rho\frac{4}{3}\pi R^3$. Substitution into eq 1 yields the following expression for l_s.

$$l_s \cong \frac{4\pi R^3}{3f}\frac{1}{2\pi R^2} = \frac{2R}{3f} \cong R \tag{3}$$

For a closed-packed assembly of equivalent spheres, the occupied volume approaches $f = 2/3$,[16] leading to the final approximation of $l_s \cong R$ in eq 3.

Estimating the Effective Interaction Length under Different Limiting Conditions. As described in the main manuscript, three different interactions may ultimately dictate the effective interaction length over which SHG is coherently produced in a powdered sample: (i) the depth of field l_d, (ii) the coherence length l_c, or (iii) the scattering length l_s. In this section, estimates for the effective volume contributing to the measured SHG intensity is provided for each limiting case. (i) Considering the simplest case first, the effective volume contributing to the detected SHG when the depth of field limits the interaction as illustrated in Figure 9a is simply given by the geometrical cross-sectional area of the particle multiplied by the depth of field l_d.

$$V_d = Al_d \tag{4}$$

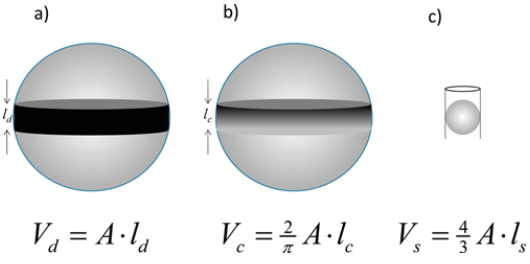

Figure 9. Pictorial depiction of the effective volumes associated with the different limiting interaction lengths. (A) Total volume is given by the product of the geometrical area and the depth of field. (b) Coherence length is scaled by a cosine function, illustrated by the gray scale in the disc. (c) Volume is equivalent to that of a sphere of cross-section πR^2.

(ii) If the coherence length ultimately limits the interaction length as illustrated in Figure 9b, only the cross-sectional area of the particle within one coherence length will generally contribute to the detected SHG. The coherence length is by definition the length at which the fundamental and doubled frequencies are phase-shifted by $\pi/2$. At this length, the next incremental contribution to the SHG will transition from constructive to destructive interference. The effective volume evaluated by the coherence length is therefore less than the geometrical length corresponding to traversing a distance of l_c through the medium by a net factor of $\pi/2$.

$$V_c = Al_c\frac{\int_0^{\pi/2}\cos z\ \mathrm{d}z}{\int_0^{\pi/2}\mathrm{d}z} = \frac{2}{\pi}Al_c \tag{5}$$

(iii) If the scattering length limits the total interaction length as illustrated in Figure 9c, the depth of field is necessarily large relative to the particle radius, such that the effective volume V_s in the limit of spheroidal particles is given by the geometrical volume of an equivalent sphere with a cross-sectional area of A.

$$V_s = \frac{4}{3}\pi R^3 = \frac{4}{3}Al_s \tag{6}$$

In eq 6, the approximation in eq 3 for the effective particle radius R.

Since the scattering length l_s is relatively straightforward to measure experimentally from the ensemble-averaged Z-dependent integrated intensity, it is convenient as a reference point for identifying the conditions under which the appropriate expression for the effective volume should be used. The point at which the depth of field and the scattering length yield equivalent effective volumes corresponds to the following equality.

$$l_d = \frac{4}{3}l_s \tag{7}$$

Considering only these two contributions, the depth of field will dictate the interaction length when $l_d \leq 4/3l_s$ and vice versa. A similar relationship can be established between l_s and l_c to identify the conditions under which the two effective volumes are equal.

$$l_c = \frac{2\pi}{3}l_s \tag{8}$$

Modeling Interactions in the Focal Volume. The optical model used is based on the paraxial approximation for a focused Gaussian beam, as described in Saleh and Teich,[31] and implicitly includes contributions from the forward coherence length and the depth of field. In brief, the amplitude and phase of the fundamental beam in the region neighboring the focal volume in the absence of scattering losses is given by the following expression.

$$E^{\omega}(z,\rho) = E_0^{\omega}\frac{W_0^{\omega}}{W^{\omega}(z)}\exp\left(\frac{-\rho^2}{W^{\omega}(z)}\right)\exp\left[-i\left(k_z^{\omega}z + k_z^{\omega}\frac{\rho^2}{2R^{\omega}(z)} - a\tan\left(\frac{z}{z_0}\right)\right)\right] \tag{9}$$

$$z_0^{\omega} = \frac{\lambda_0^{\omega}}{\pi(\theta_0^{\omega})^2} \tag{10}$$

$$W_0^{\omega} = \sqrt{\frac{\lambda_0^{\omega}z_0^{\omega}}{\pi}} \tag{11}$$

$$W^{\omega}(z) = W_0^{\omega}\sqrt{1 + \left(\frac{z}{z_0^{\omega}}\right)^2} \tag{12}$$

DOI: 10.1021/acs.analchem.5b04942
Anal. Chem. 2016, 88, 3853−3863

$$R^{\omega}(z) = z\left[1 + \left(\frac{z_0^{\omega}}{z}\right)^2\right] \tag{13}$$

For the second harmonic beam generated in a copropagating direction, the following relations emerge.

$$E^{2\omega} = (\chi^{(2)} : E^{\omega}E^{\omega}) \tag{14}$$

$$\theta_0^{2\omega} = \frac{1}{\sqrt{2}}\theta_0^{\omega} \tag{15}$$

The reduction in the cone angle arises from squaring of the Gaussian beam profile as a consequence of the quadratic dependence of SHG on the incident intensity. This squaring results in a narrowing of the angular distribution.

$$z_0^{2\omega} = \frac{\lambda_0^{\omega}}{2}\frac{1}{\pi\theta_0^{2\omega}} \tag{16}$$

$$W_0^{2\omega} = \sqrt{\frac{\lambda_0^{\omega}}{2}\frac{z_0^{2\omega}}{\pi}} \tag{17}$$

$$k^{2\omega} = \frac{2\pi n^{2\omega}}{(\lambda_0^{\omega}/2)} \tag{18}$$

The corresponding expressions for $W^{2\omega}(z)$ and $R^{2\omega}(z)$ are exactly analogous to those in eqs 12 and 13, respectively, using the values of $W_0^{2\omega}$ and $z_0^{2\omega}$ from eqs 17 and 16. From these collective equations, the following expression describes the electric field for a propagating doubled frequency in the region adjacent to the focal volume.

$$E_i^{2\omega} = E_0^{2\omega}\frac{W_0^{2\omega}}{W^{2\omega}(z)}\exp\left(\frac{-\rho^2}{W^{2\omega}(z)}\right)\exp\left[-i\left(k_z^{2\omega}z + k_z^{2\omega}\frac{\rho^2}{2R^{2\omega}(z)} - a\tan\left(\frac{z}{z_0}\right)\right)\right] \tag{19}$$

In eq 19, the expression describes the field arising from a pre-existing beam at the doubled frequency with a far-field amplitude of $E_0^{2\omega}$ but with characteristics identical to those expected for SHG within the focal volume.

In practice, the SHG field in a given Δz slice within the focal volume will consist of the coherent addition of the SHG produced in that slice with the pre-existing SHG generated from preceding slices. For coherent addition within a single crystal and under phase-matched conditions, this summation produces a quadratic scaling of the field with propagation along z. Introducing both the quadratic scaling and the tensor describing frequency conversion in the crystal yields the following expression for the incremental addition to the field at each location from SHG.

$$\Delta E_i^{2\omega} = (\chi_{ijk} : \hat{e}_j\hat{e}_k)\frac{W_0^{2\omega}}{W^{2\omega}(z)}\exp\left(\frac{-\rho^2}{W^{2\omega}(z)}\right)\exp\left[-i\left(k_z^{2\omega}z + k_z^{2\omega}\frac{\rho^2}{2R^{2\omega}(z)} - a\tan\left(\frac{z}{z_0}\right)\right)\right] \tag{20}$$

The factor of $(\chi_{ijk} : \hat{e}_j\hat{e}_k)$ is a scalar proportionality constant describing the i-polarized doubled field produced within a crystal when driven by unit j-polarized and k-polarized fundamental fields, with all the spatial and angular information contained in the term to the right of this factor. In general, the net field at each location within the crystal will consist of the coherent sum of the SHG produced previously with that generated by each next slice. For a crystal positioned with the front face in the focal plane at $z = 0$, the net SHG is generated by integration over the intensity and phase of each contribution within the focal volume and the crystal from the front crystal face the interaction length l_{int}.

$$I_{net}^{2\omega} \propto \left|\int_0^{\infty}\int_0^{l_{int}} |E^{2\omega}(z,\rho)|^2 e^{i\delta}\, dz\, d\rho\right|^2 \tag{21}$$

The phase term δ in eq 21 is given by the argument between the squared fundamental beam and the propagating second harmonic beam.

$$\delta(z,\rho) = \arg\left[\frac{(E^{\omega}(z,\rho))^2}{E^{2\omega}(z,\rho)}\right] \tag{22}$$

In the absence of dispersion, only the Guoy phase shift given by the a tan term in eq 19 will influence the relative phase between the fundamental and doubled frequencies (the sign change across the focal volume inverts the phase of the doubled frequency, but the quadratic dependence on the fundamental results in no sign change in the incremental contributions from SHG). However, the Guoy shift varies slowly when using low NA optics and rarely needs to be explicitly considered. In the presence of dispersion, the phase shift in eq 22 typically results in oscillations in the SHG as a function of crystal thickness than vary with a periodicity approximately equal to the forward coherence length.

AUTHOR INFORMATION

Corresponding Author

*E-mail: gsimpson@purdue.edu.

Notes

The authors declare no competing financial interest.

ACKNOWLEDGMENTS

The authors gratefully acknowledge financial support from the National Science Foundation GOALI award entitled "Informing Amorphous Formulations Design through Quantitative Nonlinear Optical Analysis"; Grant No. 1412888-CHE.

REFERENCES

(1) Clevers, S.; Rougeot, C.; Simon, F.; Sanselme, M.; Dupray, V.; Coquerel, G. *J. Mol. Struct.* **2014**, *1078*, 61−67.
(2) Clevers, S.; Simon, F.; Sanselme, M.; Dupray, V.; Coquerel, G. *Cryst. Growth Des.* **2013**, *13*, 3697−3704.
(3) Simon, F.; Clevers, S.; Dupray, V.; Coquerel, G. *Chem. Eng. Technol.* **2015**, *38*, 971−983.
(4) Clevers, S.; Simon, F.; Dupray, V.; Coquerel, G. *J. Therm. Anal. Calorim.* **2013**, *112*, 271−277.
(5) Galland, A.; Dupray, V.; Berton, B.; Morin-Grognet, S.; Sanselme, M.; Atmani, H.; Coquerel, G. *Cryst. Growth Des.* **2009**, *9*, 2713−2718.
(6) Newman, J. A.; Schmitt, P. D.; Toth, S. J.; Deng, F.; Zhang, S.; Simpson, G. J. *Anal. Chem.* **2015**, *87*, 10950−10955.
(7) Lee, C. J.; Strachan, C. J.; Manson, P. J.; Rades, T. *J. Pharm. Pharmacol.* **2007**, *59*, 241−250.
(8) Rawle, C. B.; Lee, C. J.; Strachan, C. J.; Payne, K.; Manson, P. J.; Rades, T. *J. Pharm. Sci.* **2006**, *95*, 761−768.
(9) Strachan, C. J.; Lee, C. J.; Rades, T. *J. Pharm. Sci.* **2004**, *93*, 733−742.

DOI: 10.1021/acs.analchem.5b04942
Anal. Chem. 2016, 88, 3853−3863

(10) Thomas, S. P.; Nagarajan, K.; Row, T. G. *Chem. Commun.* **2012**, *48*, 10559−10561.
(11) Strachan, C. J.; Windbergs, M.; Offerhaus, H. L. *Int. J. Pharm.* **2011**, *417*, 163−172.
(12) Schmitt, P. D.; Trasi, N. S.; Taylor, L. S.; Simpson, G. J. *Mol. Pharmaceutics* **2015**, *12*, 2378−2383.
(13) Wanapun, D.; Kestur, U.; Taylor, L.; Simpson, G. *Anal. Chem.* **2011**, *83*, 4745−4751.
(14) Wanapun, D.; Kestur, U. S.; Kissick, D. J.; Simpson, G. J.; Taylor, L. S. *Anal. Chem.* **2010**, *82*, 5425−5432.
(15) LeCaptain, D. J.; Berglund, K. A. *J. Cryst. Growth* **1999**, *203*, 564−569.
(16) Aramburu, I.; Ortega, J.; Folcia, C.; Etxebarria, J. *Appl. Phys. B: Lasers Opt.* **2014**, *116*, 211−233.
(17) Aramburu, I.; Ortega, J.; Folcia, C.; Etxebarria, J. *Appl. Phys. Lett.* **2014**, *104*, 071107.
(18) Aramburu, I.; Ortega, J.; Folcia, C.; Etxebarria, J.; Illarramendi, M.; Breczewski, T. *J. Appl. Phys.* **2011**, *109*, 113105.
(19) Kurtz, S.; Perry, T. *J. Appl. Phys.* **1968**, *39*, 3798−3813.
(20) Kiguchi, M.; Kato, M.; Okunaka, M.; Taniguchi, Y. *Appl. Phys. Lett.* **1992**, *60*, 1933−1935.
(21) Kiguchi, M.; Kato, M.; Kumegawa, N.; Taniguchi, Y. *J. Appl. Phys.* **1994**, *75*, 4332−4339.
(22) Moutzouris, K.; Papamichael, M.; Betsis, S. C.; Stavrakas, I.; Hloupis, G.; Triantis, D. *Appl. Phys. B: Lasers Opt.* **2014**, *116*, 617−622.
(23) Sani, E.; Dell'Oro, A. *Opt. Mater.* **2014**, *37*, 36−41.
(24) Otanicar, T. P.; Phelan, P. E.; Golden, J. S. *Sol. Energy* **2009**, *83*, 969−977.
(25) Rheims, J.; Wriedt, T. *Meas. Sci. Technol.* **1997**, *8*, 601.
(26) Kedenburg, S.; Vieweg, M.; Gissibl, T.; Giessen, H. *Opt. Mater. Express* **2012**, *2*, 1588−1611.
(27) Sultanova, N.; Kasarova, S.; Nikolov, I. *Acta Phys. Pol., A* **2009**, *116*, 585.
(28) Muir, R. D.; Sullivan, S. Z.; Oglesbee, R. A.; Simpson, G. J. *Rev. Sci. Instrum.* **2014**, *85*, 033703.
(29) Bracewell, R. *The Fourier Transform and Its Application*; McGraw-Hill: New York, 1965; Vol. 5.
(30) Sibarita, J.-B. In *Microscopy Techniques*; Springer: New York, 2005; pp 201−243.
(31) Saleh, B. E.; Teich, M. C.; Saleh, B. E. *Fundamentals of Photonics*; Wiley: New York, 1991; Vol. 22.
(32) Pressley, R. J.; Company, C. R. *CRC Handbook of Lasers: With Selected Data on Optical Technology*; Chemical Rubber Co.: Cleveland, OH, 1971.
(33) Storey, R. A.; Ymen, I. *Solid State Characterization of Pharmaceuticals*; Wiley Online Library: Chichester, U.K., 2011.
(34) Bourhill, G.; Mansour, K.; Perry, K. J.; Khundkar, L.; Sleva, E. T.; Kern, R.; Perry, J. W.; Williams, I. D.; Kurtz, S. K. *Chem. Mater.* **1993**, *5*, 802−808.
(35) Bersohn, R.; Pao, Y. H.; Frisch, H. *J. Chem. Phys.* **1966**, *45*, 3184−3198.
(36) Szostak, M. M.; Piela, K.; Hołderna-Natkaniec, K.; Natkaniec, I.; Bidzińska, E. *Carbohydr. Res.* **2014**, *395*, 29−37.
(37) Kim, E.; Steinbrück, A.; Buscaglia, M. T.; Buscaglia, V.; Pertsch, T.; Grange, R. *ACS Nano* **2013**, *7*, 5343−5349.
(38) Rogov, A.; Mugnier, Y.; Bonacina, L. *J. Opt.* **2015**, *17*, 033001.

DOI: 10.1021/acs.analchem.5b04942
Anal. Chem. 2016, 88, 3853−3863